DYNAMICS OF METABOLISM IN *NEUROSPORA CRASSA*

by

MICHAEL T. JUDGE

(Under the Direction of JONATHAN ARNOLD & ARTHUR S. EDISON)

ABSTRACT

Organisms inhabit different metabolic states depending on their developmental programming, internal resources, regulatory processes, emergent dynamics (e.g. circadian clocks), and in response to changes in their environments. The Quinic Acid (QA) gene cluster, a model for eukaryotic biochemical networks and their regulation, provides the enzymes and regulatory mechanisms for *Neurospora crassa* to shift (e.g. from glucose or starvation) to utilization of QA as a sole carbon source. While much of this process is known, the function of *qa-x* has remained elusive despite the availability of a mutant strain (Δ*qa-x*) for decades. We hypothesized that *qa-x* either assists in QA flux to central carbon metabolism or exerts broader control over QA metabolism. Continuous *in vivo* monitoring of metabolism by NMR (CIVM-NMR), a recent approach we developed, revealed latent metabolic phenotypes in the mutant, including net ethanol flux reversal. We demonstrate that this metabolic shift is triggered by quorum sensing in both the mutant and the wild-type, and that the quorum is lower in the *qa-x* mutant. Homogentisic acid (HGA) accumulation in the mutant indicates a *qa-x* function downstream of the anabolic QA pathway en route to the TCA cycle and accounts for the one known Δ*qa-x* phenotype. Finally, initial data indicate that known *Saccharomyces cerevisiae* quorum sensing signals do not induce the quorum response.

INDEX WORDS: metabolomics, metabolism, quinic acid gene cluster, *qa-x*, CIVM-NMR, quorum sensing, *in vivo*

DYNAMICS OF METABOLISM IN *NEUROSPORA CRASSA*

by

MICHAEL T. JUDGE

BS, APPALACHIAN STATE UNIVERSITY, 2015

A Dissertation Submitted to the Graduate Faculty of The University of Georgia in Partial Fulfillment of the Requirements for the Degree

DOCTOR OF PHILOSOPHY

ATHENS, GEORGIA

2021

DYNAMICS OF METABOLISM IN *NEUROSPORA CRASSA*

by

MICHAEL T. JUDGE

Major Professor:	JONATHON ARNOLD
	ARTHUR S. EDISON
Committee:	Heinz-Bernd Schüttler
	Natarajan Kannan
	Jonathan Eggenschwiler

Electronic Version Approved:

Ron Walcott
Vice Provost for Graduate Education and Dean of the Graduate School
The University of Georgia
December 2021

DEDICATION

This work is dedicated to Mary Case, a true pioneer of *Neurospora* genetics and a great teacher, advisor, and inspiration for generations of scientists.

ACKNOWLEDGEMENTS

I would like to acknowledge first my advisors, who have patiently instructed me over the last six and a half years. I could not have asked for more supportive and stimulating mentors. I would like to thank my two roommates during my time at UGA, Josh Watson and Emily Krach, who have been there for the good and challenging. Will Jordan for being an All-Star. My family, near and far, old, new, and passed. Brandon, Robert and Sydney and Group. James and Michelle Griffith for providing me guidance and a home away from home. Ricardo Borges for introducing me to grad student life and metabolomics in Art's lab. Nick Batora and Tyler Miyawaki for showing me how to grad student and being an all-round great person. Max Colonna, Gonçalo Gouveia, Olatomiwa Bifarin. Tyler and Melissa Morrison, Rex and the Holmbergs, Tim, Big Tim and Kim. Gary Munday for his encouragement and friendship early on. Many, many others who I can't name here. John and Carmen, I'm so proud of both of you. Go do great things.

TABLE OF CONTENTS

Page

CHAPTER 1

INTRODUCTION TO *IN VIVO* METABOLOMICS AND THE *QA* GENE CLUSTER IN *NEUROSPORA CRASSA*

I wrote the following section on *in vivo* metabolomics as part of a published invited review from the Edison Lab on NMR metabolomics in Analytical Chemistry (Reprinted with permission from *Anal. Chem*. 2021, 93, 1, 478–499. Copyright © 2020 American Chemical Society, available at http://pubs.acs.org/articlesonrequest/AOR-YFDTBSVHRQV4ZQJP3SWN). This is primarily relevant for introducing the CIVM paper (Chapter 2) and the CIVM component of the *qa-x* manuscript (Chapter 3). I then review the historical and current knowledge on the *qa* gene cluster in *Neurospora crassa*, as this is relevant to Chapter 3 in which I provide new insights on the function of the elusive *qa-x* gene.

In vivo metabolomics

Organisms inhabit different metabolic states depending on their developmental programming, internal resources, regulatory processes, emergent dynamics (e.g. circadian clocks), and in response to changes in their environments. Single time-point measurements with little or no sample preparation allow for rapid snapshots of metabolism across multiple samples, conditions, or times. Continuous or real-time methods provide repeated measurements on the same sample over timescales with sufficient temporal resolution to observe a given dynamic phenomenon. NMR stands alone in its ability to non-invasively study the inner workings of metabolism within a wide range of living organisms due to its sensitivity, resolution, unbiased and quantitative nature, and ability to non-destructively measure complex samples with minimal modification.

Fingerprinting and the Utility of High-Resolution Magic Angle Spinning (HR-MAS) NMR Techniques

Metabolomics data are often considered the gold standard for phenotypic measurements. Thus the most basic use of *in vivo* metabolomics leverages the strengths of magnetic resonance to provide metabolic profiles (fingerprints) of samples to aid in *de novo* annotation, facilitate sample classification, and lend a scalable functional perspective (Fuhrer et al. 2017; Mülleder et al. 2016) to metabolomics.

Sample preparation for *in vivo* NMR is typically quite simple; some cell suspensions can be measured directly in NMR tubes with only the addition of D_2O and a chemical shift reference (Himmelreich et al. 2003). However, High-Resolution Magic Angle Spinning (HR-MAS), which reduces effects of sample *inhomogeneity* (e.g. broad line shapes) for mixed-phase and solid biological samples, has gained popularity for *ex vivo* and *in vivo* metabolomics since its introduction for observing nonliving semisolids over 30 years ago (Li et al. 2006; Maricq et al. 1979). In modern HR-MAS systems, a sample is simply placed with lock solvent and chemical shift reference in a small zirconia rotor (typically < 80 μL). The rotor is then inserted into a specialized probe which tilts it to the 'magic angle' (54.7° with respect to the applied magnetic field) and spins it pneumatically about its longitudinal axis.

One use of this technology is measuring regulatory and lifestyle changes, such as those which occur in the switch to pathogenicity (Righi et al. 2013). HR-MAS provided the first *in vivo* metabolic profile of *Pseudomonas aeruginosa* to serve as a baseline for detection and identification of infections in clinical samples (Faure et al. 2018). The lack of sample disruption in HR-MAS means clinical samples such as these can subsequently be preserved or used in downstream molecular analyses. This robust technique also provided classification of microalgae *in vivo*

containing residual seawater, thus opening up metabolomics measurements for osmotically fragile marine cells in general (Chauton et al. 2003) (discussed below). Additionally, it can link together pathways important to metabolic disease and aging and allows simultaneous observation of polar small molecules and lipids. Using *in vivo* NMR measurements of lipids and other metabolites in living flies, Righi et al. dissected relationships between injury in aging/immunodeficient flies and suggested that insulin signaling plays a role in both (Righi et al. 2010). The group then found intramyocellular lipid components to be potential biomarkers for insulin resistance in mitochondrial flies, including unidentified peaks (Righi et al. 2014). More recently, an exciting study by Sarou-Kanian et al. demonstrated that HR-MAS could both quantify and localize several metabolites (e.g. to reproductive organs) in living *Drosophila* (Sarou-Kanian et al. 2015).

HR-MAS offers considerable advantages as a flexible *in vivo* metabolomics technique. However, samples can experience high acceleration while spinning (Judge et al. 2019). While microorganisms such as yeast and bacteria tolerate and even grow in comparable hypergravity, these forces have some known effects on physiology (Deguchi et al. 2011). Furthermore, these effects may be complex and difficult to distinguish from ordinary metabolic processes. Fortunately, two avenues of research are addressing this issue. First, new pulse sequences that allow for spinning speeds as low as 100 Hz have been demonstrated for intact *C. elegans* tissue and living freshwater shrimp (Mobarhan et al. 2017), greatly reducing the forces experienced by organisms during measurement. Second, an arrangement called High-Resolution Magic Angle Coil Spinning (HR-MACS) uses a small resonator coil that is made in-house and placed inside the zirconia rotor. By reducing sample radius and spinning speeds, sub-μL yeast cell suspensions are subjected to far less acceleration with preserved data quality and improved mass-sensitivity (Wong

et al. 2014). We refer to a recent review of HR-µMAS approaches (Lucas-Torres et al. 2019), which show promise for further *in vivo* measurements of microorganisms.

Other challenges in HR-MAS based studies include water and macromolecule suppression, spinning sideband attenuation, and reduced flexibility in sample conditions. These, along with spinning speed, have been partially addressed by new 1D and 2D pulse sequences (Mobarhan et al. 2017; Bastawrous et al. 2018), enabling application of HR-MAS to more sensitive specimens and extending the practical length of time-series experiments. Finally, probes with higher radio frequency (RF) power (e.g. Bruker composite multiphase (CMP) probes) have allowed comprehensive multiphase NMR measurements in freshwater shrimp which survive in the rotor for hours (Mobarhan et al. 2016). A hole can also be drilled in the rotor cap to allow for oxygenation with ambient air (Judge et al. 2019; Mobarhan et al. 2016), or treatment with alternative gas mixtures.

Observing Fluxes using Stable Isotope Labeling (SIL) Approaches.

Stable isotope labeling (SIL) has historically allowed flux to be traced through the network of metabolism from a defined start point to multiple endpoints (Eakin et al. 1972) where the label accumulates over time (Ugurbil et al. 1978). Most current SIL studies rely on ^{13}C (Clendinen et al. 2015; Edison et al. 2019), which has a large chemical shift dispersion, ubiquity of incorporation in biomolecules, and relative low natural abundance that allows labels to be selectively observed without much background. A recent application of SIL produced a combined *in vivo* and *ex vivo* annotation of a ^{13}C-enriched water flea metabolome using several multidimensional ^{1}H and ^{13}C NMR experiments. This custom reference metabolome will be used in future studies for mapping results from real-time toxicity detection experiments (Anaraki et al. 2020). The approach represents a promising general strategy of using reference datasets for future SIL studies in this

non-model organism, underscoring the flexibility of *in vivo* NMR metabolomics. SIL approaches using NMR are reviewed in more detail below as well as in other recent reviews (Jang et al. 2018; Kumar et al. 2019). However, the utility of SIL approaches is maximized when combined with real-time *in vivo* measurement (Figure 1.1).

Real-time Metabolism Measurements.

The gold standard for observing metabolism at work is a dynamic, real-time measurement. Because NMR excels at quickly and non-intrusively measuring metabolites in relatively small volumes, flow NMR systems were adapted long ago for monitoring cell cultures and conditioned media (Gonzalez-Mendez et al. 1982). In these systems, a liquid sample (such as culture media or cell suspension) is pumped through the magnet bore into the probe in a closed or open loop, and can be recycled or discarded after measurement. Alternatively, cells held within the probe can be continuously replenished with fresh media. Of particular interest, commercially available benchtop flow NMR systems extend the versatility of NMR for real-time monitoring of liquid reactions (Bradley et al. 2010) while greatly reducing overhead, and will be useful for problems like media optimization and culture control (Friebel et al. 2019). Lastly, flow NMR is not limited to single-celled organisms as multicellular aquatic organisms were recently sustained in-probe with media flow to do real-time metabolic flux monitoring (Anaraki et al. 2019).

For cell suspensions, simpler NMR setups can be used. Koczula et al. (2016) recently used solution ^{1}H NMR to collect time series spectra on agar-embedded chronic lymphoid leukemia (CLL) cells, allowing them to observe real-time metabolome shifts without sedimentation. Select peaks were traced using an in-house tool (Ludwig et al. 2011), and pH was estimated by a known internal standard (Koczula et al. 2016). For more complex samples, such as the multicellular fungus *Neurospora crassa*, HR-MAS can be used for continuous *in vivo* monitoring of metabolism

by NMR (CIVM-NMR). Judge et al. used CIVM-NMR to collect data (Figure 1.2, Panels A-B) with high temporal resolution (up to ~30s) under different oxygenation conditions without needing specialized flow NMR equipment and with minimal sample preparation (Judge et al. 2019). More recently, *C. elegans* metabolism was monitored in real time using a custom NMR tube insert that separated worms from the D_2O lock solvent (Nguyen et al. 2020). The approach used in this study offers the benefits of ease of application and high-quality real-time data without requiring an HR-MAS probe. In both this study and CIVM-NMR, features were extracted for both known and unknown peaks (Figure 1.2, Panels A-B) (Judge et al. 2019; Nguyen et al. 2020).

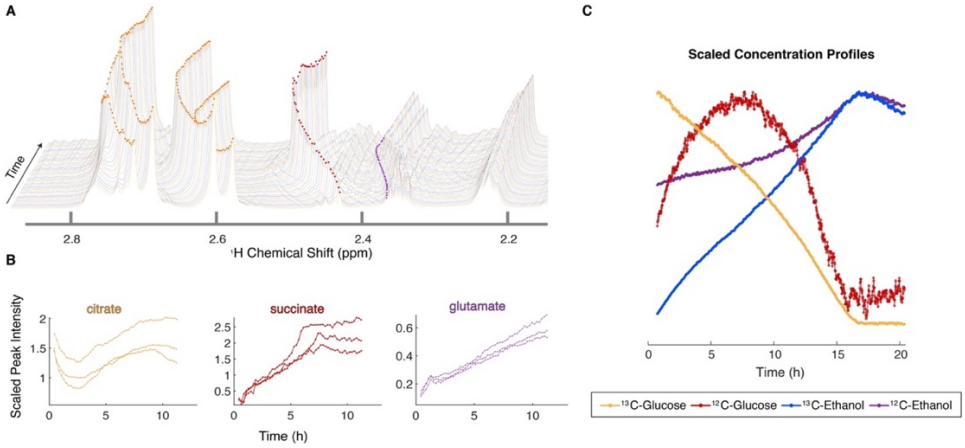

Figure 1.1. Continuous *in vivo* Metabolism by NMR (CIVM-NMR) allows for global monitoring of known and unknown endo- and exo-metabolite pools in living cells or organisms with high temporal resolution. (A) Raw data can be traced using feature (peak/ridge) extraction algorithms, and (B) plots of combined peak intensity profiles for replicate samples show high reproducibility for metabolic trends. (C) Major fluxes can be observed when SIL is used to selectively monitor labeled derivatives, and differential dynamics in distinct pools of the same metabolite can be monitored in the same sample. Reprinted with permission from *Anal. Chem*. 2021, 93, 1, 478–499. Copyright © 2020 American Chemical Society. Available at http://pubs.acs.org/articlesonrequest/AOR-YFDTBSVHRQV4ZQJP3SWN.

One particular strength of NMR is the unique ability to noninvasively conduct selective or parallel measurements of distinct pools of metabolites *in vivo*. Reed et al. recently used ^{13}C-edited NMR to track real-time incorporation of isotopically labeled glucose into multiple myeloma cells as well as define important considerations for SIL experiments (Reed et al. 2019). Likewise, Judge et al. monitored fluxes derived from ^{13}C-labeled glucose in *Neurospora*, and protons on both labeled and unlabeled carbons were measured simultaneously to reveal unique dynamics for different glucose pools in the same organism (Figure 1.2, Panel C). In the same study, specific amino acid fluxes were measured in living cancer cells (see Figure 1.3 below) (Judge et al. 2019).

Finally, while *in vivo* systems such as these are desirable, well-mixed cell cultures can be effectively sampled frequently with small volumes to yield very similar dynamic information. By injecting bacterial, yeast, or mammalian cell cultures into a mass spectrometer after in-line extraction, Link et al. were able to effectively track the response of bacterial cultures from starvation into feeding (Link et al. 2015). This study also highlights the need for modeling, as the high-density dynamic data generated from the technically impressive platform were used to fit kinetic models to interpret amino acid biosynthesis pathway dynamics (Link et al. 2014). Hyperpolarization NMR experiments, while challenging to implement and optimize, also produce data of similar temporal resolution for specific reactions (Kumar et al. 2019; Brindle et al. 2015).

In vivo Data Analysis

New approaches to data analysis are emerging for real-time metabolomics, as the ability to collect large amounts of real-time *in vivo* data currently outpaces our ability to extract and interpret information from it. In particular, advanced feature extraction tools and kinetic models trained on these new data are needed. Commercially available and proprietary software is limited for the analysis of extracted continuous NMR systems. MetaboLab from the Günther group (Koczula et

al. 2016) and in-house scripts from our own group (Judge et al. 2019) have been used for real-time *in vivo* feature tracing (Figure 1.2A) and extraction Figure 1.2B). More recently, a computer vision-based tool called RTExtract has been developed for extracting peak intensities from NMR data with continuous changes in peak location and intensity, including those from CIVM-NMR or flow NMR experiments (Wu et al. 2020). This tool greatly expands the potential of time-series *in vivo* NMR experiments by simplifying and expediting the feature extraction process as well as improving the capability to track overlapping peaks. This is exciting, as continuous spectral measurements on a system as quantitative and stable as NMR offer several advantages in solving deconvolution and alignment problems (Judge et al. 2019; Wu et al. 2020). Ultimately, automated non-parametric feature extraction flexible enough for different measurement intervals and experimental formats is desirable. Improved approaches for spectral deconvolution are also needed, particularly for HR-MAS probes, which inherently have broader linewidths that can mask coupling. Because real-time data are typically 1D, annotation is still a challenge. Faster 2D pulse sequences, which are more amenable to real-time measurements, would aid in annotation and resolution. Likewise, improved *de novo* annotation strategies could be paired with streamlined approaches for mapping peak annotations from extracted data to *in vivo* data to better leverage the benefits of both data types. Finally, integration of real-time data requires detailed kinetic models (Link et al. 2014), which do not make steady-state assumptions and are flexible with experimental format.

The QA Gene Cluster in *Neurospora crassa*

Neurospora crassa has been a key model organism for fundamental biochemistry, genetics and metabolism research for over 75 years (Beadle and Tatum, 1941). It is robust and easy to grow with limited nutritional requirements, greatly simplifying metabolic experiments. It

also grows as a haploid organism, simplifying interpretation of biochemical mutants (Davis and DeSerres, 1970). Beadle and Tatum's approach took advantage of this to demonstrate the genetic underpinnings of metabolism in auxotrophs. Indeed, one of these first auxotrophs was a tryptophan biosynthesis mutant (Beadle and Tatum, 1945).

The biochemistry to accomplish the rest of aromatic amino acid (AAA) biosynthesis was worked out in *Neurospora* by Tatum, Gross, Ehrensvard, and Garnjobst (1954). Gross and Fein (1960) then pointed out that the genes encoding for the biosynthetic steps were strongly linked, indicating a functional biosynthetic gene cluster. Giles, Case, and colleagues (1967) classified and mapped the available aromatic synthesis (*arom*) mutants to these steps, noting that one step could not be accounted for in the isolated mutations (the dehydroquinase, DHQ). Additionally, the cluster appeared to produce a multienzyme complex, distinguishing it from operons and potentially revealing a new type of regulatory unit in eukaryotes (it was later found to be a single, multi-subunit gene) (Gaertner et al. 1977; Lumsden and Coggins 1977). Giles et al. (1967) proposed the idea that the arom cluster allows for sequestration of aromatic flux to AAA biosynthesis upon discovering that *Neurospora* has both an Inducible- and a Constitutive-DHQase (I-DHQase and C-DHQase, respectively), neither of which could be mapped genetically without mutants. The I-DHQase was presumably able to compensate for loss of the C-DHQase, explaining the inability to isolate a mutant for the latter using screens for AAA auxotrophy.

It was known that the existing *arom* mutants all exhibited DHQase activity when fed QA. In looking at pleiotropic arom pathway mutants, Rines happened upon one which had none of the aromatic biosynthesis steps, exhibited severely reduced DHQase activity in the presence of QA, and was unable to utilize QA as its sole carbon source (giving it the name *qa-1*). With the I-DHQase activity reduced in this strain, the troublesome compensation for C-DHQase was

reduced enough to open up the possibility of detecting mutations in the latter by AAA auxotrophy. The *qa-1* mutant thus formed the basis of the filtration enrichment experiments that finally captured a C-DHQase mutant, which mapped to the *arom* locus and was named *arom-9* (Rines, Case and Giles 1969). Aromatic amino acid biosynthesis had therefore been mapped in *Neurospora* from 3-deoxy-d-arabino-heptulosonate 7-phosphate (DAHP; produced from glycolysis and the pentose phosphate pathway) to erythrose 4-phosphate (EPSP) and chorismate (which branches off into the three aromatic amino acids and their derivatives).

Rines then turned back to the QA pathway, recovering an I-DHQase (*qa-2*) mutation in the *arom-9* background by leveraging the lack of a C-DHQase to screen for AAA auxotrophs (Giles et al., 1985). Case isolated two other QA catabolism mutants (*qa-3*, QA/SA dehydrogenase and *qa-4*, DHS dehydratase) by screening against ability to use QA as the sole carbon source (Giles et al., 1985); these were characterized and placed in the pathway by Chaleff (1974). It was later determined through a series of heterokaryon complementation studies that *qa-1* was a *qa* cluster regulator, and in fact consisted of two genes (Huiett et al. 1986), the *qa-1F* (fast-complementing) activator and *qa-1S* (slow-complementing) repressor (reviewed in Giles et al. 1985). Thus the structural genes were accounted for to metabolize QA to protocatechuic acid (PCA), which feeds into the TCA cycle via the β-ketoadipate pathway (Harwood and Parales 1996).

Research on the *qa* cluster research was again accelerated in 1977 when Vapnek et al. at the University of Georgia demonstrated the first cloning and expression of a eukaryotic gene in a prokaryote with the transcription, translation, and subunit assembly of *qa-2* to produce a completely functional DHQase in *E. coli*. Case et al. then reported transformation and genome integration of the same plasmid back into *Neurospora* to complement a *qa-2* mutant (1979),

making molecular genetics possible in most filamentous fungi. The isolation of the entire *qa* cluster as cloned DNA fragments in *E. coli* (Schweizer et al. 1981) enabled precise mapping of

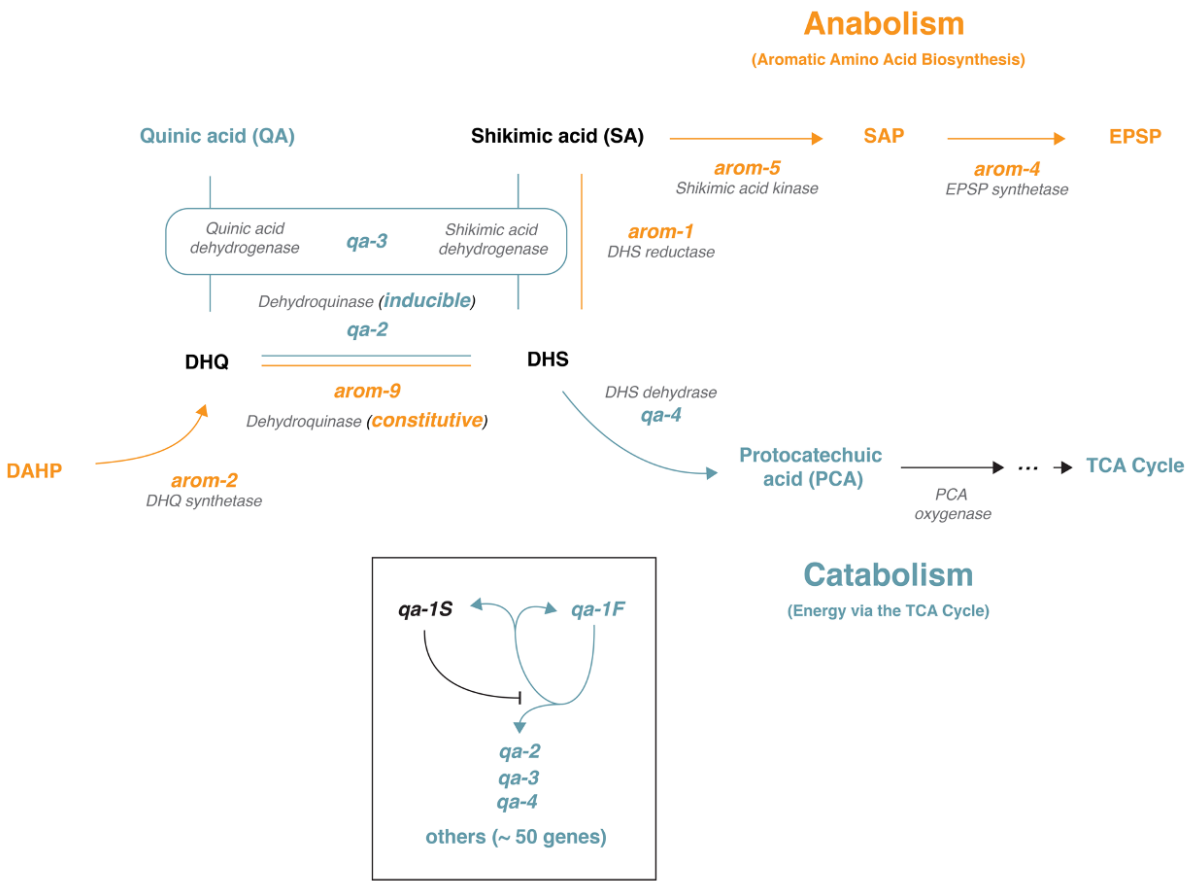

Figure 1.2. The *qa* cluster is divided into two branches. These are referred to as the anabolic (biosynthetic) and catabolic branches, and divert flux to aromatic amino acid biosynthesis. *qa-3* serves as both a QA/SA dehydrogenase. Inset shows the transcriptional regulation scheme for the cluster, where QA (not shown) results in released *qa-1S* repression.

the QA-induced transcripts and sequencing of the genes. This in turn led to the discovery of two previously unknown structural genes, *qa-y* and *qa-x* (Patel et al. 1981). These studies also revealed that the *qa* cluster genes are not transcribed as a polycistronic mRNA, as was previously suggested, but are closely clustered in the genome and share regulatory regions. Case et al. then

used a gene replacement approach to generate *qa-y* and *qa-1S* deletion mutants, and another mutant with disrupted *qa-x.* This study revealed the function of *qa-y* as a QA transporter by its insensitivity to exogenous QA but normal response to internal induction by *arom-9* mutation. The *qa-x* mutant exhibited no obvious auxotrophy, but did accumulate an as-of-yet unidentified brown pigment in liquid media after QA feeding (Giles et al., 1985, Case et al. 1992). Thus *qa-x* remains the only *qa* cluster gene of unknown function to date.

The protein sequence for *qa-x* has been computationally annotated as an inositol monophosphatase or magnesium-binding protein in databases such as Uniprot, while mixed evidence suggests a role in carbon catabolite repression.

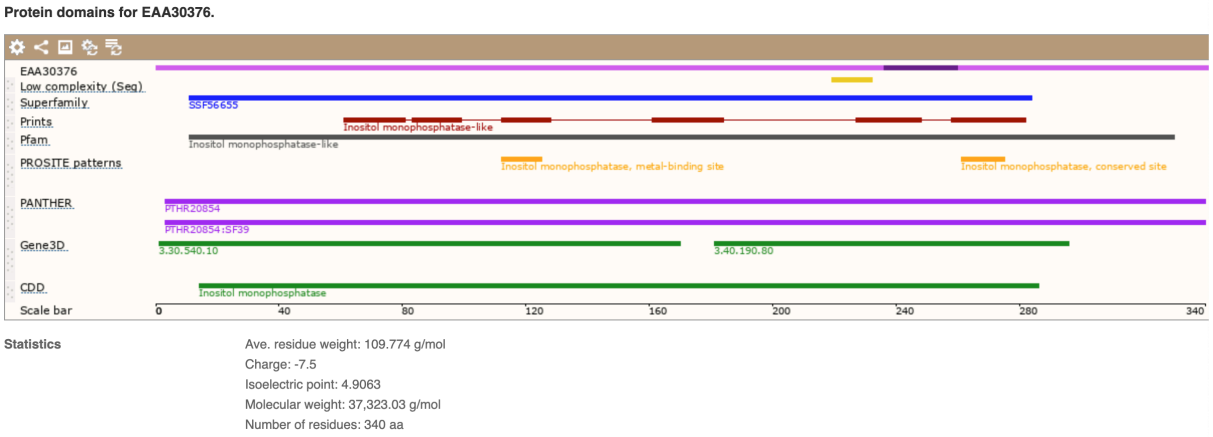

Figure 1.3. The *qa-x* gene is computationally annotated as an inositol monophosphatase. The predicted protein structure contains magnesium binding domains associated with catalytic activity, as well as conserved monophosphatase regions. Screenshot from https://fungi.ensembl.org/.

The default state of the *qa* cluster is for all 7 genes to be strongly repressed by the *qa-1S* transcription factor (Battogtokh et al., 2002, PNAS). QA likely binds *qa-1S* to release the

structural genes released from repression, allowing activation of the *qa* cluster to proceed (Battogtokh et al., 2002). Activation of the *qa* cluster has been shown in heterokaryon complementation studies to be *qa-1F*-dependent, i.e. *qa-1F*- strains are non-inducible. In the absence of functional *qa-1S* repressor activity (*qa-1SC* mutant), the entire *qa* cluster is constitutively expressed, but this is still dependent on the *qa-1F* gene. It is worth noting that, even in *qa-1Sc* strains, *qa-4*, *qa-x*, and *qa-1F* transcripts are induced further by addition of QA (Giles et al. 1985).

Carbon catabolite repression (CCR) plays a significant role in *qa* cluster regulation. The *qa* cluster is known to be repressed in the presence of rich carbon sources (Giles et al. 1985), and Arnett et al. (2009) showed that the presence of dextrose overrides QA induction of *qa-2*, *qa-3*, *qa-4*, *qa-y*, and *qa-1F* transcription. A potential role for *qa-x* in CCR had been previously posited on the basis that *qa-x* is induced weakly by QA compared to the other *qa* cluster genes. Furthermore, unlike the other structural genes, *qa-x* is strongly upregulated upon shifting from glucose to starvation (Giles et al. 1985; Case et al 1992). Arnett et al. therefore gauged the contributions of both *qa-1S* and *qa-x* to CCR of the *qa* cluster genes by measuring mRNA expression in *qa-1S* and *qa-x* mutants (2009). They determined that CCR effect on *qa-2* and *qa-4* transcripts depends strongly on *qa-1S*, although expression of both was reduced somewhat when *qa-1S* was deleted. Thus *qa-2* and *qa-4* do not appear to be regulated by CCR directly. CCR of *qa-3*, *qa-x*, and *qa-1F* depended only partially on *qa-1S*, and loss of *qa-1S* had little to no effect on CCR of *qa-y*, indicating that some mechanism(s) outside of the *qa* cluster are employed for CCR. Furthermore, *qa-x* disruption by gene replacement altered neither the *qa-2* (*qa-1S*-dependent) nor the *qa-y* (*qa-1S*-independent) transcriptional response to CCR in the *qa* cluster. These results are consistent with the knowledge that *qa-1S* deletion results in higher *qa* cluster

transcripts in the presence of glucose (Case et al. 1992), suggesting that *qa-1S* contributes to CCR of some *qa* cluster genes. The *qa-1F* gene does not appear to mediate CCR, but is itself repressed in the presence of glucose in the *qa-1S* deletion strain (Arnett et al. 2009). A role for *qa-y* as a point of control in CCR was then proposed: low expression of *qa-y* could result in exclusion of QA inducer from the cell; this in combination with strong *qa-1S* repression could keep the *qa* cluster inactivated (Arnett et al. 2009). Consistent with this interpretation is the observation that a sucrose to QA shift results in strong upregulation of *qa* cluster structural genes in QA non-utilization mutants such as *qa-4* which presumably accumulate internal inducers (Giles et al. 1985).

The CCR effect on *qa-x* is intriguing. Exogenous induction of *qa-x* is dependent on *qa-1F* and *qa-1S*. However, in strains with endogenous induction by accumulation of DHS or DHQ (like *arom-9*), only a 2-3 fold increase in *qa-x* expression is attributable to *qa-1F* activation, while loss of *qa-1S* results in complete loss of internal induction. Thus, the reported 5-10 fold increase in *qa-x* transcription in response to starvation is not due to release from *qa-1S* repression, nor is it from internal induction (Giles et al. 1985). As such, it seems likely that *qa-x* is activated by an unnamed factor, despite *qa-1S* repression.

The CRE system in *Neurospora*, in which the CreA/CRE-1 transcription factor controls the shift to cellulolytic protein secretions, is a well-known catabolite repression system in filamentous ascomycetes (Sun and Glass 2011). In Aspergillus, the primary CCR transcription factor CreA has far-reaching regulation, and also has roles in amino acid and glycogen metabolism, as well as the ethanol metabolism regulon via adh expression. The *alcR* gene positively regulates the alcohol utilization cluster under ethanol or ethyl methyl ketone induction in Aspergillus much like *qa-1F* activates the *qa* cluster in *Neurospora*. In this system, CreA was

shown to bind the promoters of alcR and a structural ethanol cluster gene to mediate CCR in the presence of glucose (Fillinger et al. 1995). Much like the *qa-1F* gene, *alcR* did not regulate all ethanol cluster genes evenly, and a degree of competition with CreA for influence over the control of these genes seems likely. This may exist in order to integrate positive control over the circuit from availability of inducers such as ethanol, threonine, ethylammonium, and negative regulation from CreA in the presence of glucose (Fillinger et al. 1995). More recently, phosphorylation sites which control the activities of this regulator were shown to cause defects in CCR, including altered glycogen and trehalose metabolism (de Assis et al. 2021). Arnett et al. (2009) reported CRE binding sites in *qa* cluster promoters. One might therefore expect a connection between *qa-x* and ethanol metabolism, as well as glycogen metabolism in *Neurospora* through the hypothesized *qa* cluster CCR regulator. Furthermore, the predicted phosphatase activity of *qa-x* may be relevant to phosphorylation states of this regulator.

Integrated modeling and transcriptomics

As one of the early attempts to model biochemical regulatory networks, *qa* cluster was first modeled using ensemble methods to fit mRNA quantification from Northern blots by Battogtokh et al. (2002). This effort was greatly expanded with the emergence of transcriptomics, wherein Tang et al. (2011) conducted careful model-guided microarray experiments to probe the transcriptional network controlling connections between the QA pathways and the rest of metabolism. Because the overlap between starvation and QA transcriptional responses was expected to be significant, the group used both a shift from glucose to QA and one from glucose to starvation (no carbon). They also intersected the microarray measurements with the subset of *Neurospora*'s 11,000 genes that have QA upstream Response Elements in their promotor regions. Several major findings are discussed below.

First, in addition to *qa-1F*, there is an additional transcription factor (NCU03643, QA-responsive cutinase transcription factor-1β) regulating response to QA. This regulator is highly conserved in filamentous ascomycetes, and controls fatty acid catabolism in *Aspergillus* (Hynes et al. 2006). The transcriptome response to the actions of these two transcription factors in *Neurospora* was specific to a handful of metabolic modules. For instance, positive control of several key flux regulation points in metabolism were indicated in a shift to starvation, including gla-1, PEP carboxykinase (*acu-6*), an aldehyde dehydrogenase (NCU03415), and a putative succinyl-CoA:3-ketoacid-coenzyme A transferase subunit (NCU06881). Upregulation of *gla-1* suggests glycogenolysis. The PEP carboxykinase suggests flux from oxaloacetate to PEP under starvation, i.e. net flux out of the TCA cycle, perhaps for gluconeogenesis. The putative aldehyde dehydrogenase may indicate an upregulation of a range of activities, including tryptophan degradation (indole acetaldehyde), gluconeogenesis (G-3-P and 3-P-G), alanine and 3-aminopropanal, and acetaldehyde conversion to acetate (a potential chokepoint reaction for ethanol degradation). Additionally, the authors point out that this enzyme and NCU06881 converge in acetoacetate flux into/out of butanoate metabolism. Lastly, sugar and amino acid transporters, including *hgt-1*, a high-affinity glucose transporter, were upregulated in response to starvation. The authors found good agreement with starvation response genes and another transcriptomics study assessing glucose transport (Xie et al. 2004). Interestingly, *qa-x* does not satisfy the requirements in their analysis of being QA-regulated, as it is also induced strongly by starvation, and its function remains a mystery.

Description of Study

In Chapter 1 of the following work I lay out our recently published method for Continuous *In Vivo* monitoring/measurement of Metabolism by NMR (CIVM-NMR), which

yields untargeted, dynamic profiles of the major metabolite pools in *Neurospora crassa* under aerobic and anaerobic glucose feeding. We validate this method by it's the consistency of its results with known biochemistry, and hypothesize extensions thereof (Judge et al. 2019). The second chapter applies this method to the classic *qa* cluster to reveal the dynamic metabolic activities associated with starvation, QA feeding, and carbon catabolite repression. We provide exciting new insights into the function of the elusive Δ*qa-x* mutant, as it exhibits latent metabolic phenotypes involving differential metabolite accumulation and metabolite pool dynamics under various conditions as compared to the wild-type. Additionally, our data reveal a distinct shift in metabolic dynamics dependent on cell density in *Neurospora*. We show that this shift occurs at a lower density in the Δ*qa-x* mutant, and provide evidence that it likely involves an as-of-yet unidentified/novel fungal quorum sensing signal.

References

Anaraki, M. T., Lane, D., Bastawrous, M., Jenne, A. & Simpson, A. J. in *NMR-Based Metabolomics: Methods and Protocols* (eds G. A. Nagana Gowda & Daniel Raftery) 395-409 (Springer New York, 2019).

Anaraki, M. T. *et al.* NMR assignment of the in vivo daphnia magna metabolome. *Analyst*, doi:10.1039/D0AN01280G (2020).

Arnett, D. R., Lorimer, H. E. & Asch, D. K. Catabolite repression directly affects transcription of the *qa-y* gene of Neurospora crassa. *Fungal genetics and biology : FG & B* **46**, 377-380, doi:10.1016/j.fgb.2009.02.003 (2009).

Bastawrous, M., Jenne, A., Tabatabaei Anaraki, M. & Simpson, A. J. In-Vivo NMR Spectroscopy: A Powerful and Complimentary Tool for Understanding Environmental Toxicity. *Metabolites* **8**, doi:10.3390/metabo8020035 (2018).

Battogtokh, D., Asch, D. K., Case, M. E., Arnold, J. & Schüttler, H.-B. An ensemble method for identifying regulatory circuits with special reference to the qa gene cluster of Neurospora crassa. *Proceedings of the National Academy of Sciences* **99**, 16904-16909 (2002).

Beadle, G. & Tatum, E. Neurospora. II. Methods of producing and detecting mutations concerned with nutritional requirements. *American Journal of Botany* **32**, 678-686 (1945).

Beadle, G. W. & Tatum, E. L. Genetic Control of Biochemical Reactions in Neurospora. *Proceedings of the National Academy of Sciences* **27**, 499, doi:10.1073/pnas.27.11.499 (1941).

Bradley, S. A. *et al.* Fermentanomics: monitoring mammalian cell cultures with NMR spectroscopy. *Journal of the American Chemical Society* **132**, 9531-9533 (2010).

Brindle, K. M. Imaging Metabolism with Hyperpolarized ^{13}C-Labeled Cell Substrates. *Journal of the American Chemical Society* **137**, 6418-6427, doi:10.1021/jacs.5b03300 (2015).

Case, M. E., Geever, R. F. & Asch, D. K. Use of gene replacement transformation to elucidate gene function in the qa gene cluster of Neurospora crassa. *Genetics* **130**, 729-736 (1992).

Case, M. E., Geever, R. F. & Asch, D. K. Use of gene replacement transformation to elucidate gene function in the qa gene cluster of Neurospora crassa. *Genetics* **130**, 729-736 (1992).

Case, M. E., Schweizer, M., Kushner, S. R. & Giles, N. H. Efficient transformation of Neurospora crassa by utilizing hybrid plasmid DNA. *Proc Natl Acad Sci U S A* **76**, 5259-5263, doi:10.1073/pnas.76.10.5259 (1979).

Chaleff, R. S. The Inducible Quinate-Shikimate Catabolic Pathway in Neurospora crassa: Genetic Organization. *Microbiology* **81**, 337-355, doi:https://doi.org/10.1099/00221287-81-2-337 (1974).

Chauton, M. S. *et al.* HR MAS 1H NMR spectroscopy analysis of marine microalgal whole cells. *Marine Ecology Progress Series* **256**, 57-62 (2003).

Clendinen, C. S. *et al.* An overview of methods using ^{13}C for improved compound identification in metabolomics and natural products. *Frontiers in Plant Science* **6**, doi:10.3389/fpls.2015.00611 (2015).

Davis, R. H. & de Serres, F. J. in *Methods in Enzymology* Vol. 17 79-143 (Academic Press, 1970).

de Assis Leandro, J. *et al.* Carbon Catabolite Repression in Filamentous Fungi Is Regulated by Phosphorylation of the Transcription Factor CreA. *mBio* **12**, e03146-03120, doi:10.1128/mBio.03146-20.

Deguchi, S. *et al.* Microbial growth at hyperaccelerations up to 403,627 × <em>g</em&gt. *Proceedings of the National Academy of Sciences* **108**, 7997, doi:10.1073/pnas.1018027108 (2011).

Eakin, R., Morgan, L., Gregg, C. & Matwiyoff, N. Carbon-13 nuclear magnetic resonance spectroscopy of living cells and their metabolism of a specifically labeled ^{13}C substrate. *FEBS letters* **28**, 259-264 (1972).

Edison, A. S., Le Guennec, A., Delaglio, F. & Kupče, Ē. in *NMR-Based Metabolomics* 69-95 (Springer, 2019).

Faure, E., Kwong, K. & Nguyen, D. Pseudomonas aeruginosa in Chronic Lung Infections: How to Adapt Within the Host? *Front Immunol* **9**, 2416-2416, doi:10.3389/fimmu.2018.02416 (2018).

Fillinger, S., Panozzo, C., Mathieu, M. & Felenbok, B. The basal level of transcription of the alc genes in the ethanol regulon in Aspergillus nidulans is controlled both by the specific

transactivator AlcR and the general carbon catabolite repressor CreA. *FEBS letters* **368**, 547-550 (1995).

Friebel, A., von Harbou, E., Münnemann, K. & Hasse, H. Reaction monitoring by benchtop NMR spectroscopy using a novel stationary flow reactor setup. *Industrial & Engineering Chemistry Research* **58**, 18125-18133 (2019).

Fuhrer, T., Zampieri, M., Sévin, D. C., Sauer, U. & Zamboni, N. Genomewide landscape of gene–metabolome associations in Escherichia coli. *Molecular systems biology* **13**, 907 (2017).

Gaertner, F. H. & Cole, K. W. A cluster-gene: Evidence for one gene, one polypeptide, five enzymes. *Biochemical and Biophysical Research Communications* **75**, 259-264, doi:https://doi.org/10.1016/0006-291X(77)91037-3 (1977).

Giles, N. *et al.* Gene organization and regulation in the qa (quinic acid) gene cluster of Neurospora crassa. *Microbiological reviews* **49**, 338-358 (1985).

Giles, N. H., Case, M. E., Partridge, C. W. & Ahmed, S. I. A gene cluster in Nuerospora crassa coding for an aggregate of five aromatic synthetic enzymes. *Proceedings of the National Academy of Sciences* **58**, 1453, doi:10.1073/pnas.58.4.1453 (1967).

Gonzalez-Mendez, R., Wemmer, D., Hahn, G., Wade-Jardetzky, N. & Jardetzky, O. Continuous-flow NMR culture system for mammalian cells. *Biochimica et Biophysica Acta (BBA)-Molecular Cell Research* **720**, 274-280 (1982).

Gross, S. R. & Fein, A. LINKAGE AND FUNCTION IN NEUROSPORA. *Genetics* **45**, 885 (1960).

Harwood, C. S. & Parales, R. E. The beta-ketoadipate pathway and the biology of self-identity. *Annual review of microbiology* **50**, 553-590, doi:10.1146/annurev.micro.50.1.553 (1996).

Himmelreich, U. *et al.* Rapid identification of Candida species by using nuclear magnetic resonance spectroscopy and a statistical classification strategy. *Applied and environmental microbiology* **69**, 4566-4574 (2003).

Huiet, L. & Giles, N. H. The qa repressor gene of Neurospora crassa: wild-type and mutant nucleotide sequences. *Proceedings of the National Academy of Sciences* **83**, 3381, doi:10.1073/pnas.83.10.3381 (1986).

Hynes, M. J., Murray, S. L., Duncan, A., Khew, G. S. & Davis, M. A. Regulatory genes controlling fatty acid catabolism and peroxisomal functions in the filamentous fungus Aspergillus nidulans. *Eukaryotic cell* **5**, 794-805 (2006).

Jang, C., Chen, L. & Rabinowitz, J. D. Metabolomics and isotope tracing. *Cell* **173**, 822-837 (2018).

Judge, M. T. *et al.* Continuous in vivo Metabolism by NMR. *Frontiers in Molecular Biosciences* **6**, doi:10.3389/fmolb.2019.00026 (2019).

Kochut, K. *et al.* IntelliGEN: A distributed workflow system for discovering protein-protein interactions. *Distributed and Parallel Databases* **13**, 43-72 (2003).

Koczula, K. M. *et al.* Metabolic plasticity in CLL: adaptation to the hypoxic niche. *Leukemia* **30**, 65-73, doi:10.1038/leu.2015.187 (2016).

Kumar, A., Kuhn, L. T. & Balbach, J. In-Cell NMR: Analysis of Protein–Small Molecule Interactions, Metabolic Processes, and Protein Phosphorylation. *International Journal of Molecular Sciences* **20**, 378 (2019).

Li, W. Multidimensional HRMAS NMR: a platform for in vivo studies using intact bacterial cells. *Analyst* **131**, 777-781, doi:10.1039/B605110C (2006).

Link, H., Christodoulou, D. & Sauer, U. Advancing metabolic models with kinetic information. *Current opinion in biotechnology* **29**, 8-14 (2014).

Link, H., Fuhrer, T., Gerosa, L., Zamboni, N. & Sauer, U. Real-time metabolome profiling of the metabolic switch between starvation and growth. *Nat Methods* **12**, 1091-1097, doi:10.1038/Nmeth.3584 (2015).

Logan, D. A. *et al.* Genome-wide expression analysis of genetic networks in Neurospora crassa. *Bioinformation* **1**, 390 (2007).

Lucas-Torres, C. & Wong, A. Current Developments in μMAS NMR Analysis for Metabolomics. *Metabolites* **9**, 29, doi:10.3390/metabo9020029 (2019).

Ludwig, C. & Günther, U. L. MetaboLab-advanced NMR data processing and analysis for metabolomics. *BMC bioinformatics* **12**, 1-6 (2011).

Lumsden, J. & Coggins, J. R. The subunit structure of the arom multienzyme complex of Neurospora crassa. A possible pentafunctional polypeptide chain. *The Biochemical journal* **161**, 599-607, doi:10.1042/bj1610599 (1977).

Maricq, M. M. & Waugh, J. NMR in rotating solids. *The Journal of Chemical Physics* **70**, 3300-3316 (1979).

Mobarhan, Y. L. *et al.* Comprehensive multiphase NMR applied to a living organism. *Chem Sci* **7**, 4856-4866, doi:10.1039/c6sc00329j (2016).

Mobarhan, Y. L., Struppe, J., Fortier-McGill, B. & Simpson, A. J. Effective combined water and sideband suppression for low-speed tissue and in vivo MAS NMR. *Anal Bioanal Chem* **409**, 5043-5055, doi:10.1007/s00216-017-0450-3 (2017).

Mülleder, M. *et al.* Functional Metabolomics Describes the Yeast Biosynthetic Regulome. *Cell* **167**, 553-565.e512, doi:https://doi.org/10.1016/j.cell.2016.09.007 (2016).

Nickerson, K. W., Atkin, A. L. & Hornby, J. M. Quorum sensing in dimorphic fungi: farnesol and beyond. *Applied and environmental microbiology* **72**, 3805-3813 (2006).

Nguyen, T. T. M. *et al.* Real-Time In-Organism NMR Metabolomics Reveals Different Roles of AMP-Activated Protein Kinase Catalytic Subunits. *Analytical Chemistry* **92**, 7382-7387, doi:10.1021/acs.analchem.9b05670 (2020).

Patel, V. B., Schweizer, M., Dykstra, C. C., Kushner, S. R. & Giles, N. H. Genetic organization and transcriptional regulation in the qa gene cluster of Neurospora crassa. *Proceedings of the National Academy of Sciences* **78**, 5783-5787 (1981).

Reed, M. A. C., Roberts, J., Gierth, P., Kupče, Ē. & Günther, U. L. Quantitative Isotopomer Rates in Real-Time Metabolism of Cells Determined by NMR Methods. *Chembiochem : a European journal of chemical biology* **20**, 2207-2211, doi:10.1002/cbic.201900084 (2019).

Righi, V. *et al.* In vivo high-resolution magic angle spinning magnetic resonance spectroscopy of Drosophila melanogaster at 14.1 T shows trauma in aging and in innate immune-deficiency is linked to reduced insulin signaling. *Int J Mol Med* **26**, 175-184, doi:10.3892/ijmm_00000450 (2010).

Righi, V. *et al.* In vivo high-resolution magic angle spinning proton NMR spectroscopy of Drosophila melanogaster flies as a model system to investigate mitochondrial dysfunction in Drosophila GST2 mutants. *Int J Mol Med* **34**, 327-333, doi:10.3892/ijmm.2014.1757 (2014).

Righi, V., Constantinou, C., Kesarwani, M., Rahme, L. G. & Tzika, A. A. Live-cell high resolution magic angle spinning magnetic resonance spectroscopy for in vivo analysis of

Pseudomonas aeruginosa metabolomics. *Biomed Rep* **1**, 707-712, doi:10.3892/br.2013.148 (2013).

Rines, H. W., Case, M. E. & Giles, N. H. Mutants in the arom gene cluster of Neurospora crassa specific for biosynthetic dehydroquinase. *Genetics* **61**, 789-800, doi:10.1093/genetics/61.4.789 (1969).

Sarou-Kanian, V. *et al.* Metabolite localization in living drosophila using High Resolution Magic Angle Spinning NMR. *Sci Rep* **5**, 9872, doi:10.1038/srep09872 (2015).

Schweizer, M., Case, M. E., Dykstra, C. C., Giles, N. H. & Kushner, S. R. Identification and characterization of recombinant plasmids carrying the complete qa gene cluster from Neurospora crassa including the qa-1+ regulatory gene. *Proceedings of the National Academy of Sciences* **78**, 5086-5090 (1981).

Sun, J. & Glass, N. L. Identification of the CRE-1 cellulolytic regulon in Neurospora crassa. *PloS one* **6**, e25654, doi:10.1371/journal.pone.0025654 (2011).

Tang, X. *et al.* Systems Biology of the qa Gene Cluster in Neurospora crassa. *PloS one* **6**, e20671, doi:10.1371/journal.pone.0020671 (2011).

Tatum, E. L., Gross, S. R., Ehrensvärd, G. & Garnjobst, L. SYNTHESIS OF AROMATIC COMPOUNDS BY NEUROSPORA. *Proceedings of the National Academy of Sciences* **40**, 271, doi:10.1073/pnas.40.5.271 (1954).

Ugurbil, K., Brown, T., Den Hollander, J., Glynn, P. & Shulman, R. High-resolution 13C nuclear magnetic resonance studies of glucose metabolism in Escherichia coli. *Proceedings of the National Academy of Sciences* **75**, 3742-3746 (1978).

Vapnek, D., Hautala, J. A., Jacobson, J. W., Giles, N. H. & Kushner, S. R. Expression in Escherichia coli K-12 of the structural gene for catabolic dehydroquinase of Neurospora crassa. *Proceedings of the National Academy of Sciences* **74**, 3508-3512 (1977).

Wong, A., Boutin, C. & Aguiar, P. M. (1)H high resolution magic-angle coil spinning (HR-MACS) μNMR metabolic profiling of whole Saccharomyces cerevisiae cells: a demonstrative study. *Front Chem* **2**, 38-38, doi:10.3389/fchem.2014.00038 (2014).

Wu, Y., Judge, M. T., Arnold, J., Bhandarkar, S. M. & Edison, A. S. RTExtract: Time-series NMR spectra quantification based on 3D surface ridge tracking. *Bioinformatics*, doi:10.1093/bioinformatics/btaa631 (2020).

Xie, X. *et al.* Transcriptional response to glucose starvation and functional analysis of a glucose transporter of Neurospora crassa. *Fungal genetics and biology* **41**, 1104-1119 (2004)

CHAPTER 2

CONTINUOUS *IN VIVO* METABOLISM BY NMR [1]

[1] Judge, M. T., Wu, Y., Tayyari, F., Hattori, A., Glushka, J., Ito, T., Arnold, J., and Edison, A.S. Continuous *in vivo* Metabolism by NMR. *Frontiers in Molecular Biosciences* **6**, (2019). Reprinted here with permission from the publisher.

Abstract

Dense time-series metabolomics data are essential for unraveling the underlying dynamic properties of metabolism. Here we extend high-resolution-magic angle spinning (HR-MAS) to enable continuous in vivo monitoring of metabolism by NMR (CIVM-NMR) and provide analysis tools for these data. First, we reproduced a result in human chronic lymphoid leukemia cells by using isotope-edited CIVM-NMR to rapidly and unambiguously demonstrate unidirectional flux in branched-chain amino acid metabolism. We then collected untargeted CIVM-NMR datasets for *Neurospora crassa*, a classic multicellular model organism, and uncovered dynamics between central carbon metabolism, amino acid metabolism, energy storage molecules, and lipid and cell wall precursors. Virtually no sample preparation was required to yield a dynamic metabolic fingerprint over hours to days at ~4-min temporal resolution with little noise. CIVM-NMR is simple and readily adapted to different types of cells and microorganisms, offering an experimental complement to kinetic models of metabolism for diverse biological systems.

Introduction

Metabolic time-series data are invaluable for the development and validation of high-quality models that accurately describe the dynamics of metabolism (Montana, Berk et al. 2011, Link, Christodoulou et al. 2014, Sefer, Kleyman et al. 2016). Information about the metabolic state of an organism typically requires extensive time, resources, and sample material. As such, researchers must choose between variables such as the number of replicates, the number of time points, and the time resolution for time-series. Furthermore, traditional metabolomics experimental designs face the challenges of extraction biases (Sitnikov, Monnin et al. 2016) and the confounding of biological and analytical variance (Anaraki, Simpson et al. 2018). While

many studies employ sample preparation and extraction approaches effectively, direct or *in vivo* measurements are fundamentally simpler to obtain and interpret. Likewise, while carefully designed (Rhoades, Sengupta et al. 2017) and executed studies with large sample sizes undeniably yield powerful insights into the dynamics of biological systems (Sengupta, Krishnaiah et al. 2016, Krishnaiah, Wu et al. 2017, Cannon, Zucker et al. 2018), continuous and repeated measurements on the same living sample are invaluable for monitoring and confirming these dynamics.

Small molecules and their fluxes have been measured *in vivo* using NMR (Bastawrous, Jenne et al. 2018), and methods have recently been developed that begin to address the need for a continuous time dimension in metabolomics data. For example, long-standing flow NMR techniques allow monitoring of secretion and uptake of extracellular metabolites for organisms grown in liquid culture (Bastawrous, Jenne et al. 2018). Link et al. recently achieved high temporal resolution on many metabolites by developing an automated real-time metabolomics platform that samples liquid cultures of single cells and directly injects them onto a time-of-flight mass spectrometer every 15-30s (Link, Fuhrer et al. 2015). The group have more recently probed the interactions between biomass synthesis and cell division in *E. coli* using this method (Sekar, Rusconi et al. 2018). Koczula et al. conducted *in vivo* measurements changes in media composition with 4-8 min resolution for chronic lymphoid leukemia. Sedimentation and line broadening are major factors that limit standard NMR measurements of complex samples like cells. Koczula et al. were able to mitigate sedimentation by immobilizing the single cells in agarose (Koczula, Ludwig et al. 2016).

Alternatively, HR-MAS enables high-resolution NMR measurements on mixed-phase samples such as tissues (Beckonert, Coen et al. 2010), or more recently, living organisms (Righi,

Apidianakis et al. 2014, Sarou-Kanian, Joudiou et al. 2015, Augustijn, Roy et al. 2016, Mobarhan, Fortier-McGill et al. 2016, Bastawrous, Jenne et al. 2018) with minimal line broadening. In this study, we extended HR-MAS to real-time continuous *in vivo* measurements of metabolism in cells. Using isotope editing, CIVM-NMR was able to reproduce and more directly observe a surprising branched-chain amino acid (BCAA) flux result reported last year in human myeloid leukemia cells (Hattori, Tsunoda et al. 2017). We found that CIVM-NMR was not only easier but faster and more conclusive than traditional approaches for flux measurements in human cell cultures. We then applied CIVM-NMR to the multicellular filamentous fungus, *N. crassa*, in both aerobic and anaerobic environments. We observed highly reproducible dynamics in central carbon and amino acid metabolism with ~4 min resolution over 11 hours. The continuous nature of these measurements facilitated metabolite annotation, and semi-automated peak tracing provided relative quantification of known and unknown compounds. We developed several new MATLAB functions and workflows, freely available through GitHub, for the analysis and visualization of these novel data. As CIVM-NMR can be applied widely to cells, tissues, and small multicellular organisms, it enables new opportunities in fields such as developmental and chronobiology for monitoring high-resolution metabolic time-series data. Importantly, it will enable more robust and experimentally-based kinetic metabolic models for diverse biological systems.

Materials and Methods

Human Leukemia Cell Culture and Preparation for HR-MAS NMR

The human BC-CML cell line K562 was obtained from ATCC, and cell line authentication testing was performed by ATCC-standardized STR analysis to verify their identity. After cell counting and washing with PBS, K562 cells were resuspended and labeled in

a custom-made Iscove's modified Dulbecco's Medium (IMDM) without BCAAs supplemented with 10% dialyzed FBS, 100 IU/ml penicillin, 100 µg/ml streptomycin and the following amino and keto acids. For ^{13}C-KIV (keto-isovalerate) tracer experiment, isoleucine, leucine and valine were supplemented at 170 µM. For ^{13}C-valine tracer experiment, isoleucine, leucine and KIV were added at 170 µM. Cell suspension (54 µl) was loaded in a clean 4 mm diameter zirconia HR-MAS rotor (Bruker BioSpin), and then either [(U)-^{13}C]-ketoisovalerate or [(U)-^{13}C]-valine solution in D_2O was added to a final concentration of 170 µM. Rotor was closed with a Kel-F rotor cap (Bruker BioSpin).

Preparation of Growth Media and Slants for *N. crassa*

Ingredients for Vogel's Media (3 % Glucose) (Glucose, 0.334 M; Biotin, 0.614 µM; Arginine, 1.95 mM; Na_3 Citrate, 9.74 mM; KH_2PO_4, 36.7 mM; NH_4NO_3, 25.0 mM; $MgSO_4$, 0.811 mM; $CaCl_2$, 0.680 mM; $ZnSO_4$, 34.8 µM; Fe $(NH_4)_2$ $(SO_4)_2$, 5.10 µM; $CuSO_4$, 2.00 µM; $MnSO_4$, 0.592 µM; H_3BO_3, 1.62 µM; Na_2MoO_4, 0.413 µM) were dissolved in ddH_2O in a large glass bottle, filter-sterilized (0.22µm Steritop Threaded Bottle Top Filter, 500mL, Millipore EMD), stirred using a magnetic stir bar, then aliquoted into clean, sterile 500-mL bottles. Ingredients for Vogel's Media with Agar (same as above, with the addition of 1.5 % agar, w/v, and using 1.5 % Glucose, w/v) were combined in a beaker. Agar was dissolved by heating in a microwave oven. The dissolved mixture was aliquoted to 15-mL or 5-mL glass test tubes, stoppered with cotton, and sterilized by autoclaving.

Vogel's Media for NMR and Wash Solution

2X Vogel's Media (minus glucose), DSS solution, and D_2O were combined to make a concentrate, which was split into two aliquots. To prepare Vogel's Media for NMR (1.5 % Glucose), filter-sterilized D-glucose solution (0.5mg/µL) was added to the smaller aliquot to a

final composition of Glucose, 0.167 M; DSS, 1mM; Biotin, 0.614 µM; L-arginine, 1.95 mM; Na_3 Citrate, 9.74 mM; KH_2PO_4, 36.7 mM; NH_4NO_3, 25.0 mM; $MgSO_4$, 0.811 mM; $CaCl_2$, 0.680 mM; $ZnSO_4$, 34.8 µM; Fe $(NH_4)_2$ $(SO_4)_2$, 5.10 µM; $CuSO_4$, 2.00 µM; $MnSO_4$, 0.592 µM; H_3BO_3, 1.62 µM; Na_2MoO_4, 0.413 µM in 95 ddH_2O/5 D_2O (v/v). Wash Solution was prepared by adding ddH2O in place of D-glucose solution to the larger aliquot.

Preparation and Storage of *N. crassa* Conidial Suspension

A frozen bd1858 (A) stock obtained by the Fungal Genetics Stock Center (McCluskey, Wiest et al. 2010) was used to inoculate two Growth Slants (Vogel's Media Agar, 1.6% Glucose w/v, 3 mL in 15 mL glass test tubes stoppered with sterile cotton plugs). These were incubated for 2 days at 30°C, then placed under a benchtop lamp at 25 °C for 2 days to induce maturation of conidia. Conidia were collected from both tubes sequentially by suspension in 12 mL Vogel's Media (no glucose) and filtration through sterile cotton. Concentration of the resulting conidial suspension was found to be 6.47 x 10E7 cells/mL using a Nexus Cellometer Auto 2000 (Nexelcom Bioscience; Lawrence, MA, USA). The conidial suspension was kept at 4 °C over the course of the experiments (4 weeks).

Growth of *N. crassa* Mycelia

Vogel's Media (50 mL, 3 % Glucose w/v) in a 250-mL Erlenmeyer flask, covered in aluminum foil was inoculated under aseptic conditions with Conidial Suspension to a total concentration of 2.7 x 10E4 cells/mL, (21 µL Conidial Suspension). Liquid cultures were grown with orbital shaking (~237 rpm) at room temperature (~25 °C) under constant cool white light (7 µmol L-1 s-1 m-2) for 32h. At that point mycelia consistently formed a single, cohesive mass. The entire culture was transferred to a 50 mL Conical Tube (Sarstedt; Newton, NC, USA) for transport to the NMR facility (15-30min).

Preparation of *N. crassa* Mycelia

Under aseptic conditions, a section of mycelium from the edge of the main mycelial mat was cut off using a sterile tube cap and trimmed to fit the volume of approximately 126 µL using a pre-marked microcentrifuge tube. Mycelia were handled from this point using clean, sterile tweezers (cleaned with 70 % EtOH on a lint-free single-ply lab tissue (kimwipe) and dried in an aseptic environment). The section of mycelium was then patted dry on autoclaved filter paper (Whatman Filter Paper #3; GE Healthcare, USA) atop a layer of folded kimwipes, and was washed by placing in a sterile microcentrifuge tube containing 1 mL Wash Solution and vortexing briefly (~10 s) until the mycelium had fully absorbed the media. Washing was repeated with fresh Wash Solution for a total of 4 washes. The mycelium was reduced to ~63 µL (0.9 x volume of rotor + plug), measured in a second microcentrifuge tube pre-marked to that volume. The mycelium was pat-dried in a sandwich of sterile filter paper folded into kimwipes, pressing firmly three times (until no liquid spots were visible on the filter paper). The dried mycelium was then weighed in a separate microcentrifuge tube. The dry mycelium was 9.04-10.13 mg in our experiments (μ = 9.62 mg; SD = 0.32 mg). We observed a reduction in mass of ~30 % as conidia, loose filaments, and other debris are removed along with waste products and glucose during wash steps. In our hands, the prep process took between 4 and 13 min., during which time the organism was immersed in a low-glucose environment.

Loading *N. crassa* Mycelia into the Rotor

The dried, weighed mycelium was then placed in a microcentrifuge tube containing fresh Vogel's Media for NMR (500 µL, 1.5 % Glucose), and vortexed briefly until the mycelium had fully absorbed the media. The mycelium was then transferred to a third, pre-marked microcentrifuge tube (63 µL). By adding/removing media, the volume was adjusted to the 63 µL

volume mark. Sterile tweezers were used to transfer the mycelium to a clean 4 mm diameter zirconia rotor (Bruker BioSpin) cleaned by rinsing with bleach solution, tap water, 70 % ethanol, tap water, and ddH2O x 4). The mycelium was pushed to the bottom, taking caution not to lose liquid. The remaining liquid in the tube was added to the rotor and one tweezer prong was used to position the mycelium to remove larger air bubbles, although small bubbles occurred with no issues in the NMR. A Teflon sealing plug (Bruker BioSpin) was then inserted to ~2 mm below the edge of the rotor. For the aerobic condition, a Kel-F rotor cap (Bruker BioSpin) modified with a 0.016-inch diameter hole drilled using a lathe was lined on the inside with three layers of Rayon breathable microplate sealing tape (QuickSeal Breathable Film, Thomas Scientific, USA) to prevent spore escape. The cap was fully inserted to push the sealing plug into its final position. The cap was then removed, and the insides of the cap and plug were inspected to ensure that no liquid was lost and that an airspace existed between the plug and the sample. The rotor was then re-capped, the bottom edge marked with a permanent marker, and dropped into the bore of the magnet (cap facing up). In our hands, this process typically takes 15-30 min. For the anaerobic condition, media was added to fill all airspaces and an unmodified cap was used to prevent gas exchange. For the ^{13}C labeling experiment in partially anaerobic conditions, an airspace was left and fresh Vogel's Media for NMR was prepared with 3% (w/v) ^{13}C-labeled Glucose (99% labeled; Cambridge Isotope Laboratories; Tewksbury, MA, USA) was used in place of 1.5% (w/v) glucose.

NMR Parameters

For human ML cell experiments, a hsqcetgpsisp.2 gradient Heteronuclear Single Quantum Coherence Spectroscopy (HSQC) experiment run as a 1D experiment was used with the following parameters: Data Points: 7272. Dummy Scans: 4 at the beginning of the run.

Number of Scans: 128 /timepoint. O1 offset: 4.699 ppm. O2 offset: 30.000 ppm. Acquisition Time 0.3999600 s. Delay: 1.5 s. fid Resolution: 2.500250 Hz. Receiver Gain: auto (101). Temperature: 298 K = 25 °C. Spinning Speed: 3100 Hz. A standard noesypr1d protocol (Bruker) was used for N. crassa non-labeled real-time metabolomics measurements. The following parameters applied to all samples and timepoints: Data Points: 42856. Dummy Scans: 8 at the beginning of the run. Number of Scans: 64 /timepoint. Spectral Width 11904.762 Hz. Acquisition Time 1.7999520 s. Delay: 1.5 s. fid Resolution 0.555570 Hz. Receiver Gain: auto (101). Temperature: 298 K = 25 °C (calibrated using a deuterated methanol standard (Van Geet 1970)). The following parameters were optimized for each sample: O1 offset for water suppression: 2817.24 - 2818.24 Hz. PWL9 water suppression power: 43.87 - 44.42 dB (μ = 44.23 dB, SD = 0.19 dB). P1 pulse width: 12.49 - 13.30 μs (μ = 12.78 μs, SD = 0.29 μs). Spinning Speed: 6000 Hz. Notably, this variation in pulse width between samples manifested as a difference in temporal resolution (i.e. longer pulse widths resulted in time points slightly farther apart). The effect was measurable (on the order of minutes) over hundreds of measurements. The average experiment took 4.23min +/- 0.004min (SD). For measurement of ^{13}C in the labeled glucose experiment, a modified hmqc Heteronuclear Multiple-Quantum Correlation (HMQC) experiment with additional phase cycling was used. The following parameters were used: Data Points: 3636. Dummy Scans: 8 at the beginning of the run. Number of Scans: 64 /timepoint. O1 offset: 2826.24 Hz. O2 offset: 12070.62 Hz. Acquisition Time 0.2545200 s. Delay: 1.5 s. fid Resolution 3.928964 Hz. Receiver Gain: auto (101). Temperature: 298 K = 25 °C. Spinning speed: 6000 Hz. All Bruker parameter files are available with the raw data at http://www.metabolomicsworkbench.org/.

Automated Data Acquisition and Post-experiment Sample Preparation

For human ML cells, spectra were collected sequentially using the multizg command in TopSpin (v4.0.1; Bruker). For N. crassa samples, the noesypr1d experiment, optimized for the sample, was imported into IconNMR in TopSpin (v4.0.1; Bruker). The solvent was set to "D2O_H2O+salt". The "iterate" command was used to queue 1024 identical, sequential noesypr1d experiments (each taking ~4.6 min) on a Bruker NEO equipped with a 4-mm CMP probe. Dummy scans were only implemented for the first experiment. Experiments generally ended after ~12 h, though some were allowed to continue as long as 37 h. By spinning N. crassa at 6 KHz, spinning sidebands (Maricq and Waugh 1979) were eliminated in the spectral region of 0-10 ppm. At the end of each run, the mycelia were transferred from the rotor to a sterile microcentrifuge tube with clean, sterile tweezers. All liquid from the rotor was also transferred to the tube. This was either extracted and assessed for growth immediately, or was allowed to sit on the bench for one day.

Survival Assessment

Sterile tweezers were used to tear a piece of mycelium from the rotor contents; this was used to inoculate a growth slant. All growth slants were assessed for 24 h or longer post-inoculation for growth. Photographs were taken using a 16MP digital camera on an LG G5 cell phone in Manual Mode.

Extraction

The remaining rotor contents were transferred with a pipette to a microcentrifuge tube containing a mixture of zirconia beads (1 mm, 167 µL or ~375 mg; 0.7 mm, 334 µL or ~1314 mg; 500 µL total) on dry ice. The old tube was rinsed by briefly vortexing with 800 µL MeOH (80 % in ddH2O), which was added to the beads. This mixture was either processed immediately

or frozen on dry ice for up to 3 days. Contents were twice homogenized on dry ice for 180 s @1800 rpm using a MP FastPrep 96 (MP Biomedical; USA) adapted for microcentrifuge tubes, adding dry ice each time. The homogenate was centrifuged at 14k rpm at 4 °C for 5 min (18220 x g; Centrifuge 5417C; Eppendorf, USA). The supernatant was transferred to a separate microcentrifuge tube and kept on dry ice while the pellets were back-extracted with 500 µL MeOH (80 %), homogenized once for 180 s @1800 rpm, and centrifuged an additional 5 min. Supernatants from both extractions were combined, then dried to completion in a CentriVap Concentrator/CentriVap Cold Trap -105 °C system (Labconco, Kanasas City, MO, USA) for 4-6 h. Pellets for two samples were combined during resuspension in D_2O (DSS, 1/9 mM) for each condition. Two replicates from each condition were pooled and pipetted into 1.5 mm NMR tubes (Norell; Morganton, NC, USA).

Annotation

For each pooled sample representing the anaerobic and the aerobic conditions, noesypr1d, ^{13}C-HSQC, Total Correlation Spectroscopy (TOCSY), and ^{13}C-HSQC-TOCSY spectra were collected on a 600 MHz Bruker magnet equipped with a 5mm cryoprobe and an Avance III HD console at the University of Georgia NMR Facility. 2D data were processed in nmrPipe (System Version 9.4 Rev 2017.340.17.07 64-bit) and submitted to COLMARm (Bingol, Li et al. 2016) for putative compound identification. After manual inspection, metabolites were assigned a confidence level ranging from 1 to 5, with 5 being the highest. The scale is defined (Walejko, Chelliah et al. 2018) as follows: (1) putatively characterized compound classes or annotated compounds, (2) matched to literature and/or 1D reference data such as HMDB (Wishart, Tzur et al. 2007) and BMRB (Ulrich, Akutsu et al. 2008) (3) matched to HSQC, (4) matched to HSQC and validated by HSQC–TOCSY (COLMARm (Bingol, Li et al. 2016)), and

(5) validated by spiking the authentic compound into sample. Identifications from extracted 1d spectra were manually mapped to real-time in vivo noesypr1d data. An additional score was assigned to each mapped compound: 0 (unannotated), 1 (annotated only), 2 (qualitatively assessed), or 3 (relatively quantifiable) in the real-time data. This score depended on number of observed peaks, baseline, peak overlap, and sensitivity. Both metabolite confidence levels are reported in Table S1. All raw and processed data files are available at http://www.metabolomicsworkbench.org/ and matching can be run on COLMARm (Bingol, Li et al. 2016) directly.

Batch Processing in nmrPipe for *in vivo* NMR Data

Parameters were optimized based on agreement between spectra from several time points for a given sample. A custom bash script ran nmrPipe (Delaglio, Grzesiek et al. 1995) using the optimized parameters on all spectra for a given sample. This script included all necessary nmrPipe commands for file conversions and NMR data processing. In brief, the following were implemented: line broadening, Fast Fourier Transform, 0- and 1st-order phasing, end removal, and baseline correction using automatic polynomial fitting. All raw data, parameter files and code are available at http://www.metabolomicsworkbench.org/.

Additional Processing in MATLAB for *in vivo* NMR Data

For each sample, custom scripts were written in MATLAB R2017b (The MathWorks, Inc., Natick, Massachusetts, USA), to load the processed spectra, ppm vectors, and measurement start times from .ft and .acqus files. Spectra were then referenced to DSS semi-automatically, stored as a matrix, and saved as a MATLAB workspace in .mat format. Using custom MATLAB scripts, .mat files from individual experiments were combined into a "sampleData" structure. Metadata (e.g. condition, pulse width, time shift between inoculation and start time) were added

to each sample by manual entry or by automated retrieval from the Bruker acqus files for each sample. Spectral ends outside of [-0.5,10] ppm were removed. The spectral region containing the water signal [4.7,5] ppm was replaced by zeros. Measurements for time points >11 h were removed in all experiments for consistency. Each spectrum was normalized to its DSS peak intensity as a formal step to allow for relative quantification. Finally, every three spectra were summed starting from the first timepoint for improved signal-to-noise. The resulting structure was saved as a .mat file (~2 Gb). All data and scripts are available at http://www.metabolomicsworkbench.org/ and at https://github.com/artedison/Edison_Lab_Shared_Metabolomics_UGA.

Relative Quantification of NMR Resonances

A combination of a Gaussian smoothing filter with user-defined sigma in the ppm and time dimensions and peak picking script was used to identify peak maxima for a given region of ~0.5-1 ppm in a given sample, allowing some noise to be picked. Agglomerative clustering based on single linkage of Euclidean distances was then used to cluster the picked points in the chemical shift (ppm), time, and intensity space. Weights for each dimension in the clustering, as well as the number of clusters, were manually optimized for each region and sample. Clusters were quality-controlled by interactive visual inspection. If multiple ridge points existed for the same time, the one with highest intensity was retained. Peak positions at temporal gaps were estimated using linear interpolation between the two closest existing ridge points. Ridges on the smoothed data were mapped to the unsmoothed data for each time point by choosing the maximum within a small window around the peak position obtained from the smoothed data. A window size of 10 indices (~2.9 x 10-3 ppm) worked for all but a few ridges, whose optimal mapping windows ranged between 6 and 60 indices (between 1.7 x 10-3 and 1.7 x 10-2 ppm).

All ridges were visually inspected for good tracing, well-defined peaks, and minimal overlap by plotting on real spectra. To combine the trend information from multiple ridges annotated to the same compound, intensities of constituent ridges were scaled such that the ridge means across the time points shared by the highest number of ridges were equal. Lastly, the mean across scaled ridges at each time point was taken, yielding a single composite trajectory for each compound.

Titration of a Citrate Standard for Estimation of in-vivo pH Changes

A 10 mM solution of citric acid (A104-500; Fisher Scientific, USA) containing 1mM DSS reference standard was prepared, and 600 µL were added to a 5 mm NMR tube (Norell; Morganton, NC, USA). The pH of the solution was adjusted in-tube in ~0.25 pH increments by addition of 0.5-2 µL volumes of dilutions of concentrated NaOH and HCl and four rounds of inversion and vortex mixing. For each pH point, exact pH was measured in-tube using a calibrated accumet AB150 pH meter (Fisher Scientific, USA), then a 1D noesypr1d spectrum was collected (DS = 2; NS = 16) on a 600 MHz Bruker magnet equipped with a 5mm cryoprobe and an Avance III HD console at the University of Georgia NMR Facility. Data were phased and referenced to DSS in TopSpin (v3.5pl7; Bruker). Custom Matlab scripts were used to obtain the most upfield citrate peak position for each pH. A 3rd-order polynomial was fit to the positions ($R2 > 0.99$) and used with the ridge belonging to the same peak to estimate the pH of each culture at each timepoint.

Results

Isotopic CIVM-NMR measurements confirm unidirectional KIV-to-valine flux in ML cells

Branched-chain amino transferase-1 (BCAT1) is a reversible enzyme, but in most cells the reaction degrades BCAAs and makes branched-chain keto acid (BCKA)s. However, we recently demonstrated that BCKA transamination by the BCAT1 enzyme builds up the BCAA pool in

myeloid leukemia (ML) cells, essentially running in the reverse direction(Hattori, Tsunoda et al. 2017). When α-keto-isovalerate (KIV; one of the substrates of BCAT1) was ^{13}C-labeled, valine (the expected product of BCAT1) containing ^{13}C accumulated. Labeled KIV was not observed when ^{13}C-labeled valine was supplied, indicating a non-canonical, unidirectional flux from KIV to valine (Hattori, Tsunoda et al. 2017). In that study, metabolic fingerprints were acquired via a traditional, labor- and material-intensive sampling scheme involving months of sample preparation and several dozen samples. One reason for the large number of samples in this or similar studies is the biological and technical variation due to sample preparation steps; these factors make it more challenging to compare time-series data without large numbers of replicates. We sought to replicate the result of the original Hattori et al. study using real-time *in vivo* metabolomics.

First, we cultured myeloid leukemia cells as previously described (Hattori, Tsunoda et al. 2017), then pelleted and resuspended them in IMDM media without KIV or valine. Working quickly, we loaded the cells into an HR-MAS rotor and added either ^{13}C-labeled KIV or valine to make a total volume of ~60 μL, capped the sample, and inserted the rotor into the magnet. We recorded 1D HSQC spectra every 4.2 minutes while spinning at 3500 Hz at the magic angle (54.7°) (Beckonert, Coen et al. 2010). A hole in the rotor cap allowed for gas exchange (Mobarhan, Fortier-McGill et al. 2016).

Figure 2.1. Targeted isotopic CIVM-NMR measurement of metabolic flux in human myeloid leukemia cells. (A) ^{13}C-labeled keto-isovalerate (KIV) was converted to valine. **(B)** ^{13}C-labeled valine was not converted to KIV, confirming unidirectional flux in ML cells.

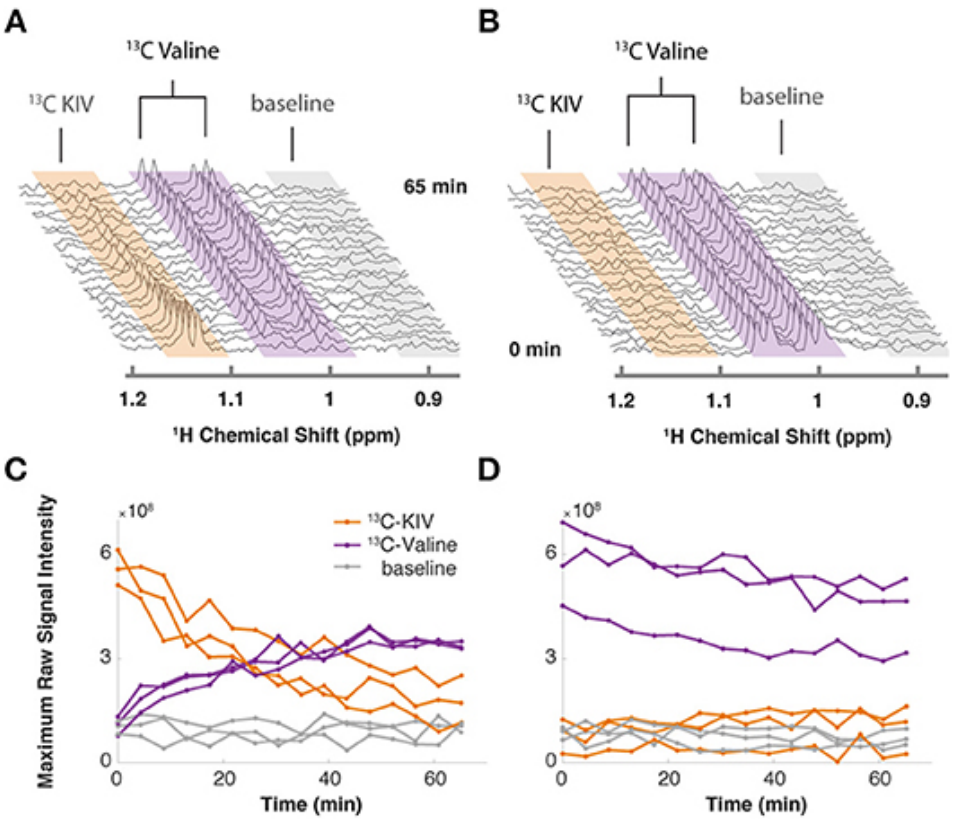

By monitoring the intensity of the methyl peaks of both KIV and valine, we observed that ^{13}C-labeled KIV decreased in intensity and fell close to the limit of detection within about 60 min (Figure 2.1A). The ^{13}C-labeled valine peak grew with an inversely proportional trajectory, providing real-time, *in vivo* evidence of KIV-to-valine conversion. As the reaction rate depended on the concentration of the cells in the rotor, cell density was adjusted to accommodate measurement of the rapid reaction and provide greater detail about reaction kinetics. As reported previously, labeled KIV was not observed when ^{13}C-labeled valine was supplied (Figure 2.1B). Thus, the original results from Hattori et al. that took months of sample prep and data collection were reproduced with real-time resolution in one afternoon. We did not need to adapt the culture media (Link, Fuhrer et al. 2015) or embed the cells (Koczula, Ludwig et al. 2016) to get these

results. Additionally, the combined rate of uptake and conversion of valine could be measured with precision, where measurements at only a few time points were taken previously.

Untargeted CIVM-NMR measurements of *N. crassa* growth

Given the utility of CIVM-NMR for the targeted monitoring of known reactions in mammalian cells, we applied it to the continuous measurement of the metabolic dynamics of the filamentous fungus *N. crassa* over 11 h in both aerobic and anaerobic environments. *N. crassa* is an obligate aerobe but will live under low oxygen conditions (Slayman 1965, Slayman and Slayman 1968, Slayman, Long et al. 1973). We grew *N. crassa* tissue in a nutrient-rich liquid medium (Figure 2.2A). After 30 h, a piece of tissue with a volume of ~50 µL was taken from the main mycelial mass, rinsed, and put into a 4-mm HR-MAS rotor with fresh media. The rotor was sealed with a cap with a hole filtered with rayon culture tape punches ("aerobic") (Mobarhan, Fortier-McGill et al. 2016) or no hole ("anaerobic"), placed in the HR-MAS probe, and spun at 6000 Hz at the magic angle for the duration of each experiment (Figure 2.2B). Each individual scan of a standard 1dnoesypr experiment took ~3.97 s. Scans were recorded and summed continuously, and free induction decays (fids) were written to a file once every 64 scans, establishing our shortest temporal resolution at 4.23 min (Figure 2.2C). After data acquisition, properly phased and Fourier-transformed frequency-domain data were added together to increase the signal-to-noise ratio (S/N) at the expense of temporal resolution (Figure 2.2D). The organism was assessed for survival after each experiment (ranging between 11 h to 4 days). In every case (n = 9), mycelia did not sediment, were intact, and grew significant hyphae within hours of being placed on standard nutrient agar (Supplementary Figure 1). Thus, *N. crassa* survived the CIVM-NMR experiments and could be used in downstream experiments or processing steps (Figure 2.2E). Custom shell scripts allowed for batch processing of NMR data (Figure 2.2D) using

NMRPipe (Delaglio, Grzesiek et al. 1995). Normalizing to the stable 1 mM DSS reference resonance (0.0 ppm) allowed for relative comparison of peak intensities across time points and samples. To improve S/N, sequential spectra were time-averaged, resulting in 12.7-min temporal resolution for all downstream analyses (Figure 2.2D).

To assist with annotation and compound identification, the organism and media were removed at the end of each run, bead-homogenized, and extracted in MeOH (80%) (Figure 2.2E). Combined supernatants for representative samples were analyzed using ^{13}C-HSQC, HSQC-TOCSY, and noesypr1d NMR experiments, and the data were matched to an NMR metabolomics database using COLMARm (Bingol, Li et al. 2016). Resulting putative identifications were manually assigned confidence scores as described previously (Walejko, Chelliah et al. 2018). We mapped 34 metabolites with high confidence scores onto the real-time *in vivo* spectra of *N. crassa* (representative annotations, Figure 2.2F), including multiple amino acids and metabolites involved in the TCA cycle, glycolysis, and fermentation (Figure 2.3A-C; Supplementary Table 1). Several metabolites overlapped with those found in a previous NMR study in *N. crassa* (Kim, Kaiser et al. 2011*)*. We created MATLAB functions for visualization of time series data for samples individually (Figure 2.2C-D) or as interactive mirror images (Figure 2.3). We found that the latter approach facilitated comparison between samples, revealing several differences in metabolism between the aerobic and anaerobic conditions (Figure 2.3) that were reproduced in replicate samples (Supplementary Figure 2).

Figure 2.2. Sample preparation and analysis for CIVM-NMR experiments. (A) Samples were first grown to a suitable volume or density in standard media and **(B)** transferred to the HR-MAS rotor (*N. crassa* is shown). Gas composition (e.g. air availability) was altered using a

filtered hole or no hole in the cap, and the rotor was spun at the magic angle. NMR data were collected continuously every 4 minutes over the course of hours, then **(C)** processed and normalized to the DSS reference peak (0 ppm) to yield full-resolution data. **(D)** Every three spectra were time-averaged (summed) for improved S/N, and peak intensities were traced across time using ridge tracing to yield relative quantification of metabolites. **(E)** Following HR-MAS, the rotor contents were homogenized, methanol-extracted, and used for 2D NMR analysis for peak annotation by database matching. **(F)** For annotated metabolites with >1 peak (e.g. citrate), the quantified and annotated trajectories (ridges) for each peak were scaled and combined into a single representative trajectory. Trajectories for each annotated compound in 3 aerobic experiments are plotted to compare time series between biological replicates.

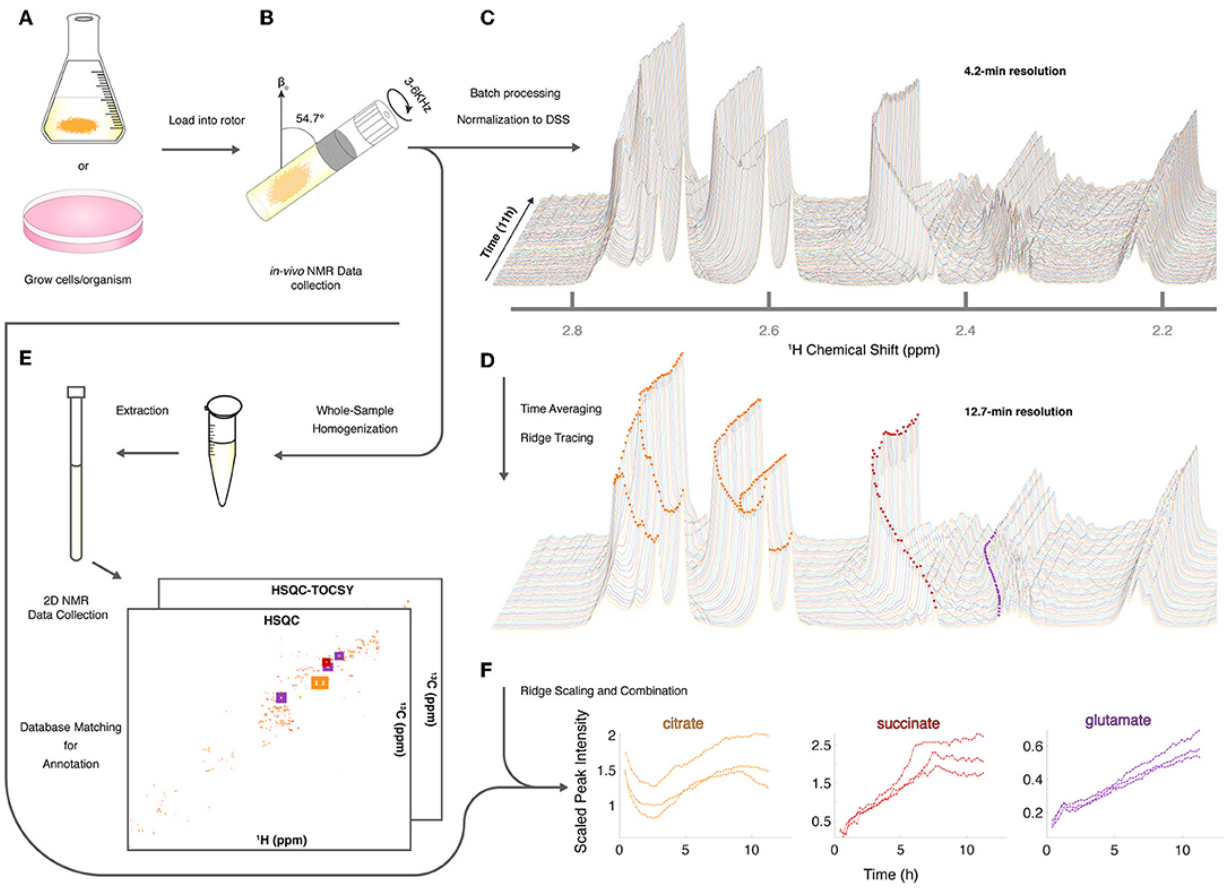

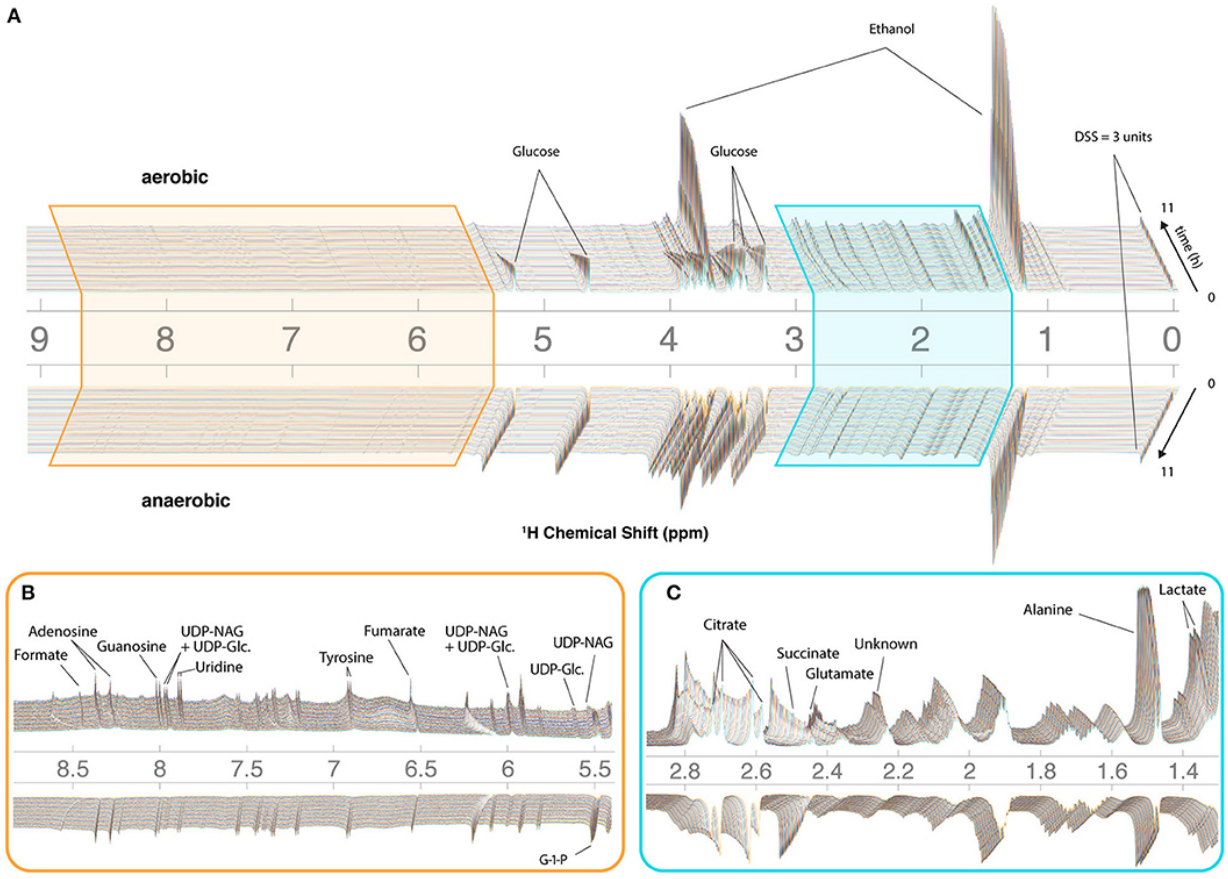

Figure 2.3. CIVM-NMR measurements of *N. crassa* metabolism under aerobic and anaerobic conditions. ^{1}H NMR data for one aerobic replicate (top) and one anaerobic replicate (bottom) plotted interactively as a 'mirror plot' for direct comparison between conditions by peak height and position at a given time. To improve the S/N, data were analyzed at 12.7 min resolution. Annotations are shown for select peaks of interest for **(A)** the entire spectrum, and expansions of **(B)** the aromatic region and **(C)** the aliphatic region. Several peaks change position and intensity over the course of the experiments. Abbreviations: UDP-NAG, UDP-N-Acetyl Glucosamine; UDP-Glc., UDP-Glucose; G-1-P, Glucose-1-Phosphate.

Relative quantification of metabolites by ridge tracing

The 34 compounds that were mapped to *in-vivo* data were assigned a second confidence score for quantifiability. For 21 highly scoring metabolites (Supplementary Table 1), we obtained relative quantification (Supplementary Figure 3) by tracing peaks across time with a ridge-tracing algorithm (Figures 2.2D, 4A). With our current algorithm that is limited to peaks with low overlap, we traced over 170 peaks across all of our spectra, including ~150 that are currently un-annotated. We combined the information from ridges of sufficient quality when assigned to the same compound (Figure 2.4B), leveraging the information about compound concentration from multiple measurements. Replicates of dense, continuously repeated

Figure 2.4. Ridge tracing produces concentration dynamics of metabolites. (A) Multiple traced ridges for a single aerobic replicate. Peak maxima at each time point were located using a peak-picking algorithm that includes an adjustable Gaussian filter. Maxima were connected to form ridges along the time dimension using a single linkage hierarchical agglomerative clustering based on Euclidean distances between the points in chemical shift, time, and intensity space. Metabolites typically have several characteristic NMR peaks, e.g. the 4 orange ridges in citrate **(A)**. A simple time-wise average represented by the black line in **(B)** only gives the average intensity over time but loses valuable information on actual dynamic trends. To more accurately extract trends for a particular metabolite, we first integrate each peak in that metabolite over time to obtain its mean value. Then, each peak trajectory is scaled by ratio of the highest mean to its own mean, yielding the 4 orange lines in **(C)**. The mean of these trajectories is shown in black in **(C)** and represents the relative concentration over time for that metabolite in that replicate. The 3 aerobic (red) and 3 anaerobic (blue) replicates for citrate are shown in (**D)**.

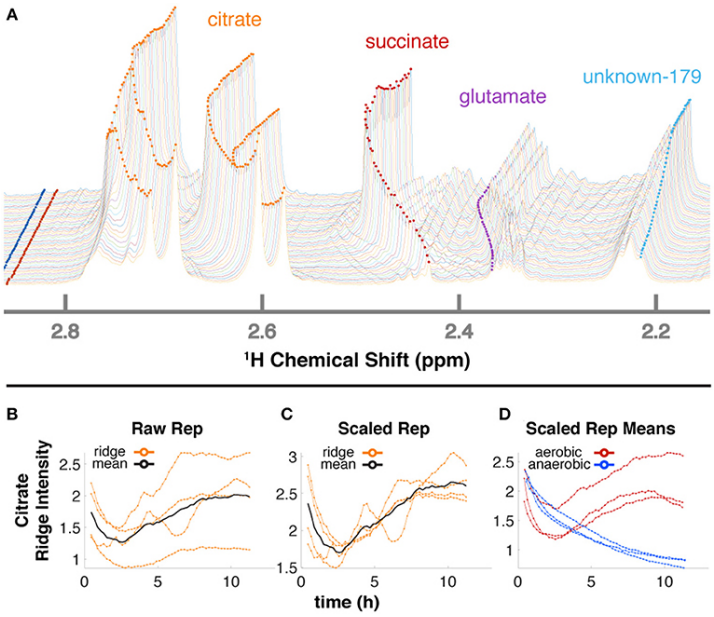

measurements on the same sample offer benefits (Sefer, Kleyman et al. 2016) that would be eliminated by taking time-wise averages or standard errors. We are developing more comprehensive and robust statistical treatments of these unique data within a modeling framework to address this need.

Glucose-dependent changes in pH

NMR chemical shifts are sensitive to pH and metal ion content (Tredwell, Bundy et al. 2016, Ye, De Iorio et al. 2018), typically requiring peak alignment algorithms that are prone to creating artifacts. The positions of peaks clearly changed across time in our data (Figures 2.3B-C, 4A), particularly in the aerobic samples. Because these changes were monitored continuously, peak identity across time was unambiguous, eliminating the need for alignment and facilitating annotation and quantification even as changes in peak position affected overlap with other peaks. Changes in peak position for organic acids in our samples were compared with reported titration curves (Koczula, Ludwig et al. 2016, Tredwell, Bundy et al. 2016, Ye, De Iorio et al. 2018), in-house titrations for citrate (Supplementary Figure 4), and Bruker AssureNMR software (Bruker Biospin, USA; Supplementary Table 2) to estimate pH of the sample at each timepoint. Our data

indicate that the pH of the aerobic cultures began at 6.2-6.4, then dropped to 5.2-5.4 coincidentally with glucose consumption. Furthermore, this acidification reversed after glucose depletion at 6-7h, and pH increased to 5.5-5.7 by the end of our experiments. In the anaerobic samples, the pH decreased from 6.2-6.3 to 5.7-5.9. Although we did not perform high-resolution titrations for glutamate, succinate, and fumarate, their reported shifts were consistent with the trends for citrate (Supplementary Table 2). Maintenance of characteristic differences in pH is well-accepted between organelles, the cytoplasm, and the extracellular milieu (Magnuson and Lasure 2004, Casey, Grinstein et al. 2010, Bencina 2013). Filamentous fungi including N. crassa (Vrabl, Fuchs et al. 2012) secrete large amounts of organic acids such as citrate, fumarate, and succinate, to acidify their extracellular environment (Magnuson and Lasure 2004, Kubicek, Punt et al. 2010, Dorsam, Fesseler et al. 2017), and the two latter acids are taken up by carbon-limited N. crassa, with maximal uptake occurring around pH 5.5.

Activation of central carbon metabolism in aerobic conditions

Under aerobic conditions, glucose and trehalose were consumed within the first 6h while ethanol and lactate were produced. Glucose fell below our limit of detection by ~6h, after which it was depleted as the concentrations of ethanol and lactate plateaued (Figures 2.3A-B, 5). The inverse trends between sugars and fermentation products indicate that most carbon was shunted to fermentation. In fact, we observed that most ^{13}C in labeled glucose was channeled to ethanol and succinate (Supplementary Figure 5), consistent with known N. crassa biochemistry (Colvin, Sauer et al. 1973, Greenfield, McKenzie et al. 1988). Low levels of trehalose, another energy metabolite in the aerobic samples are consistent with vegetative growth, while increasing levels in the anaerobic samples may reflect a developmental shift to production of conidia in response to stress (Hill and Sussman 1964).

Four TCA cycle metabolites were detected in our experiments (Figures 2.3B-C). Fumarate and succinate increased in the aerobic condition, and both accumulated slightly faster around 6h following glucose depletion and remained abundant (Figure 2.5). This dynamic could be a result of glyoxylate cycle (Voet and Voet 2011) or mixed acid fermentation (Dreyfuss, Zucker et al. 2013) activation, and would not be observable without a continuous, densely sampled time series. Standard replicate averaging with extracted samples at different times would average out much of this detail. Next, one of the clearest signs of low oxygen levels in the anaerobic sample was the slight reduction in succinate compared to the drastic reduction in fumarate. Succinate levels in the aerobic condition are comparable to those in the anaerobic condition, while fumarate accumulates much more in the aerobic condition (Figure 2.5). This is explained by the fact that conversion from succinate to fumarate depends on oxygen reduction in the electron transport chain (Dreyfuss, Zucker et al. 2013, Kanehisa, Sato et al. 2016). Finally, citrate was abundant in the aerobic condition and followed a complex trend, while malate was observed in endpoint extracts (Supplementary Figure 6A). Taken together,

Figure 2.5. Integration of central metabolic pathways. Arrows correspond to one or more reactions, and nodes correspond to metabolites (Dreyfuss, Zucker et al. 2013, Kanehisa, Sato et al. 2016). Nodes are filled for observed metabolites. Plots show the means of scaled peak/ridge intensities for a given compound in a given replicate over traceable times, where red and blue trajectories represent aerobic and anaerobic conditions, respectively. Arrows indicate typical reaction directions. The glyoxylate cycle is shown as a shunt through glyoxylate embedded in the TCA cycle.

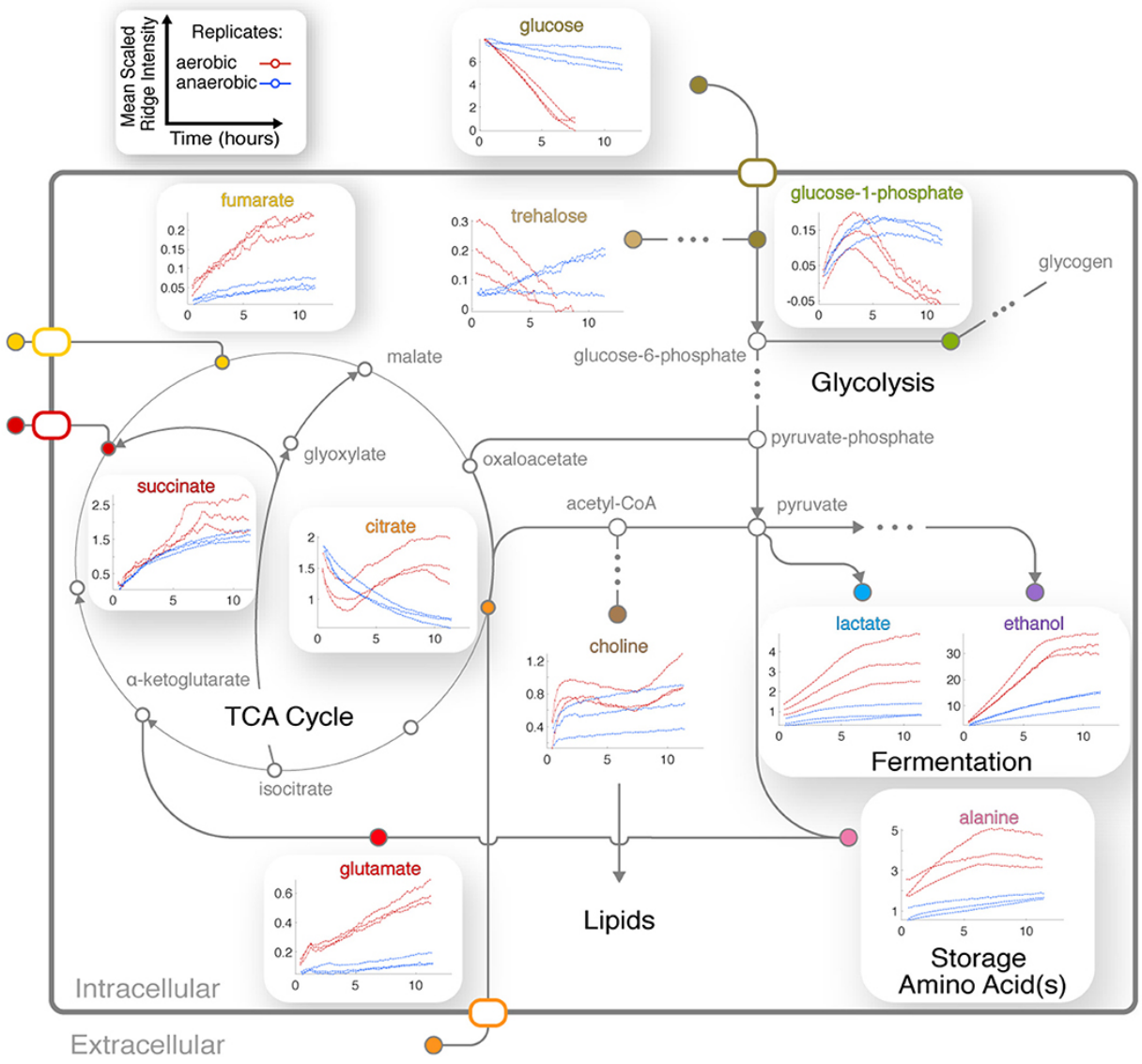

these trajectories constitute strong evidence for active glycolysis and fermentation in the presence of glucose and oxygen, while alternative pathways such as the glyoxylate cycle were active after glucose depletion. Similar trends with lower rates were observed in the anaerobic samples, except for differences in citrate and glucose-1-phosphate (G-1-P) (Figure 2.5).

Interplay between amino acid, central carbon, and nitrogen metabolism

The dynamics of glutamate were different between the two conditions (Figure 2.5). Glutamate accumulates while synthesis of glutamine is repressed in N. crassa in nitrogen-sufficient conditions (Kanamori, Legerton et al. 1982). We could not annotate glutamine with confidence because of overlap (Supplementary Table 1B). However, resonances consistent with glutamine increased after ~3h (Supplementary Figure 6B), indicating potential nitrogen insufficiency in the aerobic culture. Arginine levels correspond to those of glutamate in the aerobic condition (Supplementary Figure 3). Glutamate is produced from arginine degradation (Voet and Voet 2011); for instance, arginine has been reported as an abundant amino acid in extracted samples of actively growing N. crassa cultures (Kanamori, Legerton et al. 1982, Kim, Kaiser et al. 2011) and is thought to be catabolized to glutamate during conidiation (Kim, Kaiser et al. 2011).

Trends for alanine (Figure 2.5) and an unknown in the aliphatic region (Figure 2.4A) were very similar to that of ethanol and lactate (Figure 2.5), indicating that their metabolic fluxes are closely dependent on intermediates or energy produced by glycolysis and fermentation. This hypothesis is supported by the fact that alanine is synthesized from glutamate and pyruvate by alanine transaminase (Kanamori, Legerton et al. 1982, Radford 2004). Glutamate levels increased and were unaffected by glucose, but alanine first accumulated and then decreased upon glucose depletion (Figure 2.5). We conclude that alanine synthesis was limited by a lack of pyruvate caused by glucose depletion. Glutamate levels are maintained during starvation (Voet and Voet 2011), and Kanamori et al. (1982) suggested that alanine serves as a storage for pyruvate and nitrogen via glutamate in favorable conditions (Kanamori, Legerton et al. 1982). Therefore, the observed decrease in alanine suggests that it was utilized for pyruvate and

glutamate when glucose concentrations were low in the aerobic condition (Figure 2.5). Our CIVM-NMR data therefore supports glutamate as a hub between central carbon and amino acid pathways and confirms the maintenance of glutamate stores even under starvation.

Complex trends reveal dynamics between energy storage and cell wall synthesis pathways

CIVM-NMR data revealed significant changes that preceded glucose depletion at ~6 h for compounds such as citrate, choline, adenosine, and valine, which all had similar trends in the aerobic condition (Figure 2.5). Citrate decreased at the start of all experiments. Under aerobic conditions it began to accumulate again around 2.5 h and surpassed initial levels, while in anaerobic conditions it decreased at an exponential rate to a very low amount (Figure 2.5). In the anaerobic samples, citrate was utilized while succinate accumulated to levels similar to those in the aerobic samples. However, fumarate levels remained low. Lack of oxygen could explain low rates of conversion from succinate to fumarate, while glyoxylate cycle activity can occur in anaerobic conditions (Wayne and Lin 1982, Rude, Toffaletti et al. 2002) and yields succinate and malate without fumarate.

N. crassa does not survive on citrate as a sole carbon source (Wolfinbarger and Kay 1973), and to our knowledge extracellular citrate utilization has not been reported for *N. crassa*. However, citrate levels were observed well below the initial amount present in the media alone (9.74 mM) in both conditions, strongly indicating that external citrate was consumed in both experiments. Isotopic labeling experiments will more directly test this hypothesis.

Pyruvate and acetyl-CoA both serve as crossroads between major energy metabolites and lipids. Although we did not observe pyruvate and acetyl-CoA directly, most accumulating metabolites in pathways emanating from pyruvate exhibited strikingly similar trends (Figure 2.5), suggesting flux through pyruvate. Curiously, citrate and choline did not follow this pattern,

indicating activity from pathways that consume and replenish their pools. However, the rates of change of these metabolites were clearly opposed in both aerobic and anaerobic samples. This opposition suggests that flux from acetyl-CoA was being channeled differentially between citrate and choline synthesis and demonstrates a major carbon and energy exchange between central metabolism and lipid precursors (Markham, Robson et al. 1993).

The accumulation of citrate and choline after glucose depletion in the aerobic samples was puzzling. Prior work has indicated that under low oxygen or glucose depletion *N. crassa* cells become vacuolated (Slayman, Moussatos et al. 1994, Slayman and Potapova 2006). The synthesis of membranes for the vacuoles and their membranes under anaerobic conditions would explain the rise in choline. A concordant decrease in G-1-P at ~3h may indicate a shift of carbon flux to glycolysis from glycogen, caused by sensing of extracellular glucose levels (Wang, Li et al. 2017) or limitations of glycogen capacity. Glucose conversion to G-6-P (Glucose 6-phosphate) is the first step of glycolysis (Voet and Voet 2011), which was clearly active in the first stages of our aerobic condition (Figure 2.5). High levels of G-6-P drives its conversion by phosphoglucomutase to G-1-P (Voet and Voet 2011), which is converted by UDP-glucose pyrophosphorylase and UTP hydrolysis to the direct glycogen precursor UDP-glucose (Voet and Voet 2011). The latter is the rate-limiting step in glycogen synthesis, which is an endergonic process. If G-6-P levels were high and flux were shunted to glycogen, high levels of G-1-P would be expected. In fact, G-1-P levels increased in the aerobic samples until around 3 h then decreased, while UDP-Glucose was also observed. Therefore, we conclude that glycogen synthesis occurred in the first half of the aerobic experiments, but slowed or reversed after 3 h. This conclusion is further supported by the fact that glycogen synthesis occurs during high rates of growth in *N. crassa*, and wanes during slow growth (Brody and Tatum 1967, de Paula,

Azzariti de Pinho et al. 2002, Virgilio, Cupertino et al. 2017). On the other hand, high levels of G-1-P are unlikely to be produced by the relatively low levels of glycolysis observed in the anaerobic samples and can indicate glycogen degradation. G-1-P accumulated to comparable levels in both conditions, but it remained in the anaerobic samples. Glycogen degradation is exergonic and releases G-1-P and glucose directly in an approximate 9:1 ratio (Voet and Voet 2011). Furthermore, UDP-Glucose was not observed in the anaerobic samples. Thus, high levels of G-1-P in the anaerobic conditions may indicate glycogen degradation.

The primary chitin cell wall building block UDP-N-acetylglucosamine (UDP-GlcNAc) (Milewski, Gabriel et al. 2006) increased in only the aerobic cultures (Figure 2.3, Supplementary Figure 2.6C), although overlap and low intensity prevented quantification. UDP-GlcNAc is synthesized via the unidirectional Leloir pathway (Milewski, Gabriel et al. 2006), and the only known uses for UDP-GlcNAc in *N. crassa* are chitin/cell wall biosynthesis and UDP-GalNAc production (Edson and Brody 1976, Milewski, Gabriel et al. 2006). Filamentous fungi such as *N. crassa* produce chitinases (Patil, Ghormade et al. 2000) and could utilize these for autolysis under stress conditions. However, if an increase in UDP-GlcNAc indicated cell wall degradation (i.e. due to stress or autolysis), those resonances would be expected to increase in the anaerobic condition; however, they were barely detected (Figure 2.3, Supplementary Figure 6C). Curiously, a recent study suggested that *N. crassa* utilizes alternative chitin catabolism pathways that would not result in increased GlcNAc-derived UDP-GlcNAc (Gaderer, Seidl-Seiboth et al. 2017). Considering the above dynamics, we conclude that resources were allocated between energy storage and cell wall synthesis pathways in glucose-rich conditions.

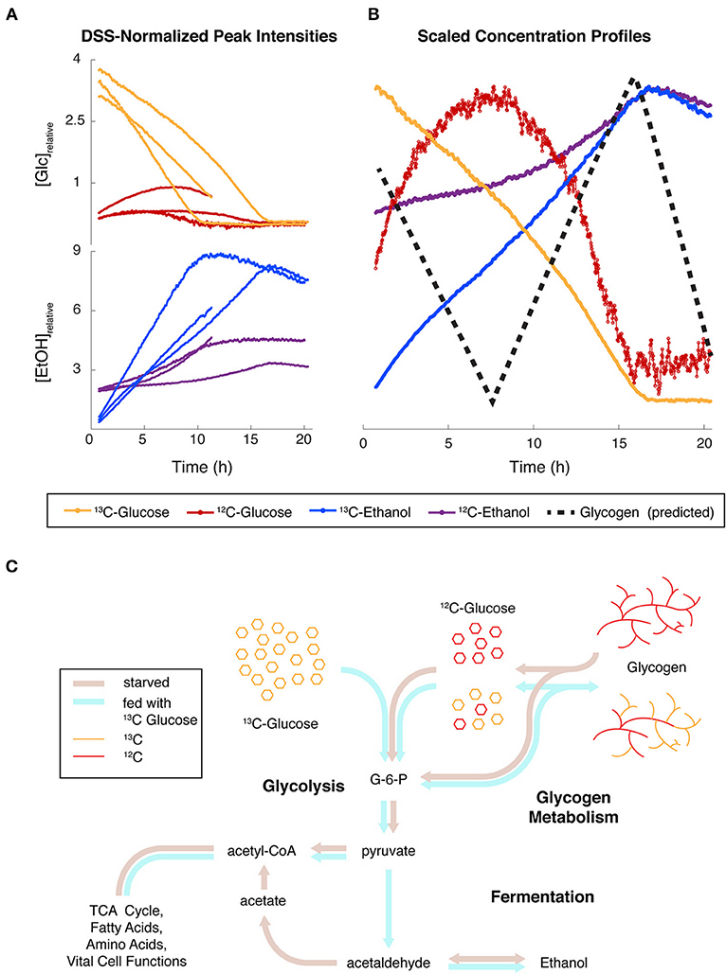

Figure 2.6. Simultaneous monitoring of carbon isotopes reveals convergence of major glucose fluxes from different origins. (A) Relative concentrations for Glucose (Glc) and Ethanol (EtOH) containing ^{12}C and ^{13}C in N. crassa cultures fed with ^{13}C-labeled glucose (t = 0 h) after 2 h of starvation. Protons covalently attached to ^{12}C and ^{13}C were differentiated in noesypr1d experiments by ^{13}C-induced splitting. Three independent replicates are shown. One replicate was only recorded for 11 h. (B) Relative concentrations scaled by the maximum of each trajectory of one replicate highlight the relationships between trends. A hypothesized glycogen trajectory is plotted as a black dotted line. (C) Hypothesized fluxes through glycolysis, glycogen metabolism, and fermentation under starved (brown arrows) and fed (blue arrows) conditions.

Discussion

We have demonstrated the use of CIVM-NMR to monitor metabolic dynamics in cells and whole microorganisms. An uninterrupted, high-resolution time series of NMR data allows observation of rapid but reproducible metabolic events. In contrast, using traditional studies of different replicates for each time point, the biological and technical variation often obscure details of dynamics. The lack of extraction removes a major source of technical variation found in typical MS and NMR metabolomics workflows and can facilitate inter-study comparisons. NMR has relatively low sensitivity, but it is a quantitative and reproducible technique, and conventional NMR cryoprobes allow routine proton detection of compounds at concentrations as low as about 5 μM ^{1}H. HR-MAS probes are generally less sensitive. However, the temporal dimension of CIVM-NMR data allows for more confident assignment of peaks with surprisingly low signal-to-noise ratios. By taking advantage of this unique property of CIVM-NMR data, we detected peaks as low as ~24-62 μM ^{1}H (Supplementary Figure 7). The sensitivity of CIVM-NMR is therefore particularly well-suited for observation of the major sources, sinks, and bottlenecks of metabolism in an organism or cells (e.g. for metabolic engineering). For instance, absolute quantification of 103 metabolites in *E. coli* by LC-MS/MS revealed intracellular concentrations ranging from 0.13 μM to 96 mM. Of these, 61 were found in concentrations of 100 μM or higher (Bennett, Kimball et al. 2009), placing them well within the detection limits of CIVM-NMR.

Only 20-70 μL of sample is needed with no sample preparation to yield an entire time series for various metabolites, and the sample can be used in downstream *in vivo* or chemical analyses following NMR data collection. These factors make CIVM-NMR ideal for scarce samples that would not otherwise be possible to study by time-series metabolomics (Sefer,

Kleyman et al. 2016). With an internal rotor radius of 1.4 mm spinning at 6000 Hz, our samples experienced up to 200,000 x g of acceleration. As sedimentation was not observed, it is possible that a low relative density of *N. crassa* mycelia compared to the media may have resulted in a lower effective radius of rotation. While some samples, including the leukemia cells in Figure 2.1, are less stable at high spinning rates, microorganisms such as *E. coli* and *S. cerevisiae* can grow under different amounts of hypergravity, even with cellular and organellar sedimentation (Deguchi, Shimoshige et al. 2011). Furthermore, methods have been developed to obtain HR-MAS data with slow spinning (Mobarhan, Struppe et al. 2017), which could allow monitoring in ~1500 x g or less. The lack of perfusion and a limited sample volume are both factors that need to be considered with regard to nutrient depletion and waste accumulation. Lastly, identification of spectral features and deconvolution of overlap are still challenging in any NMR or LC-MS metabolomics study. However, temporal continuity clearly provides information (e.g. as seen in Figure 2.3 and Supplementary Figure 7) that will be helpful in addressing these problems.

Full utilization of the time series data from CIVM-NMR will require a modeling-based method, and our data underscore the need for accurate and experimentally-based kinetic models of metabolism. With the potential for <4-minute resolution by using fewer scans before saving fids at the cost of signal-to-noise ratio, CIVM-NMR provides a unique opportunity for probing flux changes as well as allosteric regulation (Link, Kochanowski et al. 2013) with kinetic models (Link, Christodoulou et al. 2014, Link, Fuhrer et al. 2015) for abundant metabolites. Each replicate can be seen as a single, complete model with different initial conditions, which is significantly better than a time series of averages. Previous real-time methods (Link, Fuhrer et al. 2015, Koczula, Ludwig et al. 2016) have equal or greater temporal resolution at the expense of disadvantages such as being destructive (Link, Christodoulou et al. 2014), limitation to cell

suspensions (Link, Christodoulou et al. 2014, Koczula, Ludwig et al. 2016), primarily measuring the media(Koczula, Ludwig et al. 2016, Sengupta, Krishnaiah et al. 2016), or having combined biological and technical variance. CIVM-NMR minimizes noise by eliminating sampling and extraction variance. Batch effects for each replicate are eliminated since all experimental and NMR parameters are consistent across timepoints. Analytical drift is eliminated because the detector never contacts the samples, and the sample is not perturbed by measurement. These factors in turn facilitate optimization of modeling parameters (Ghasemi, Lindsey et al. 2011).

CIVM-NMR can also allow continuous monitoring of the metabolic state before, during, and after a range of environmental and genetic perturbations. For instance, we observed a shift from a glucose-rich environment to starvation at ~6h. Sequential utilization of alternative carbon sources such as quinic acid (Tang, Dong et al. 2011) is a natural extension of this work. In studies involving targeted pathways in mammalian cells, CIVM-NMR can facilitate the testing of mutants, gene knockdowns, or small molecule substrates, inhibitors, or activators. We are exploring the use of alternative gas mixtures for spinning the rotor, allowing adjustment of O_2:CO_2:N_2 ratios during experiments. This presents another environmental shift and facilitates monitoring of cells (e.g. mammalian) which require controlled gas compositions. Real-time temperature control could also be used to probe temperature shifts or assess the effects of a temperature-sensitive mutation on the metabolism of an organism. Perturbations such as these will be critical to exploring and refining dynamics in kinetic models with an empirical basis.

References

Augustijn, D., Roy, U., van Schadewijk, R., de Groot, H. J. & Alia, A. Metabolic Profiling of Intact Arabidopsis thaliana Leaves during Circadian Cycle Using 1H High Resolution

Magic Angle Spinning NMR. *PLoS One* **11**, e0163258, doi:10.1371/journal.pone.0163258 (2016).

Bastawrous, M., Jenne, A., Tabatabaei Anaraki, M. & Simpson, A. J. In-Vivo NMR Spectroscopy: A Powerful and Complimentary Tool for Understanding Environmental Toxicity. *Metabolites* **8**, doi:10.3390/metabo8020035 (2018).

Beckonert, O. *et al.* High-resolution magic-angle-spinning NMR spectroscopy for metabolic profiling of intact tissues. *Nat Protoc* **5**, 1019-1032, doi:10.1038/nprot.2010.45 (2010).

Bencina, M. Illumination of the spatial order of intracellular pH by genetically encoded pH-sensitive sensors. *Sensors (Basel)* **13**, 16736-16758, doi:10.3390/s131216736 (2013).

Bennett, B. D. *et al.* Absolute metabolite concentrations and implied enzyme active site occupancy in Escherichia coli. *Nature chemical biology* **5**, 593 (2009).

Bingol, K., Li, D. W., Zhang, B. & Bruschweiler, R. Comprehensive Metabolite Identification Strategy Using Multiple Two-Dimensional NMR Spectra of a Complex Mixture Implemented in the COLMARm Web Server. *Anal Chem* **88**, 12411-12418, doi:10.1021/acs.analchem.6b03724 (2016).

Brody, S. & Tatum, E. L. Phosphoglucomutase mutants and morphological changes in neurospora crassa. *Proc Natl Acad Sci U S A* **58**, 923-930 (1967).

Cannon, W. *et al.* Prediction of Metabolite Concentrations, Rate Constants and Post-Translational Regulation Using Maximum Entropy-Based Simulations with Application to Central Metabolism of Neurospora crassa. *Processes* **6**, 63 (2018).

Casey, J. R., Grinstein, S. & Orlowski, J. Sensors and regulators of intracellular pH. *Nat Rev Mol Cell Bio* **11**, 50-61, doi:10.1038/nrm2820 (2010).

Colvin, H. J., Sauer, B. L. & Munkres, K. D. Glucose utilization and ethanolic fermentation by wild type and extrachromosomal mutants of Neurospora crassa. *J Bacteriol* **116**, 1322-1328 (1973).

de Paula, R., Azzariti de Pinho, C., Terenzi, H. F. & Bertolini, M. C. Molecular and biochemical characterization of the Neurospora crassa glycogen synthase encoded by the gsn cDNA. *Mol Genet Genomics* **267**, 241-253, doi:10.1007/s00438-002-0659-4 (2002).

Deguchi, S. *et al.* Microbial growth at hyperaccelerations up to 403,627× g. *Proceedings of the National Academy of Sciences* **108**, 7997-8002 (2011).

Delaglio, F. *et al.* NMRPipe: A multidimensional spectral processing system based on UNIX pipes. *J Biomol Nmr* **6**, 277-293, doi:10.1007/bf00197809 (1995).

Dorsam, S. *et al.* Sustainable carbon sources for microbial organic acid production with filamentous fungi. *Biotechnol Biofuels* **10**, 242, doi:10.1186/s13068-017-0930-x (2017).

Dreyfuss, J. M. *et al.* Reconstruction and Validation of a Genome-Scale Metabolic Model for the Filamentous Fungus Neurospora crassa Using FARM. *Plos Comput Biol* **9**, doi:ARTN e1003126

10.1371/journal.pcbi.1003126 (2013).

Edson, C. M. & Brody, S. Biochemical and genetic studies on galactosamine metabolism in Neurospora crassa. *J Bacteriol* **126**, 799-805 (1976).

Gaderer, R., Seidl-Seiboth, V., de Vries, R. P., Seiboth, B. & Kappel, L. N-acetylglucosamine, the building block of chitin, inhibits growth of Neurospora crassa. *Fungal Genet Biol* **107**, 1-11, doi:10.1016/j.fgb.2017.07.005 (2017).

Ghasemi, O. *et al.* Bayesian parameter estimation for nonlinear modelling of biological pathways. *BMC Syst Biol* **5 Suppl 3**, S9, doi:10.1186/1752-0509-5-S3-S9 (2011).

Greenfield, N. J., McKenzie, M. A., Adebodun, F., Jordan, F. & Lenard, J. Metabolism of D-glucose in a wall-less mutant of Neurospora crassa examined by ^{13}C and 31P nuclear magnetic resonances: effects of insulin. *Biochemistry* **27**, 8526-8533 (1988).

Hattori, A. *et al.* Cancer progression by reprogrammed BCAA metabolism in myeloid leukaemia. *Nature* **545**, 500-504, doi:10.1038/nature22314 (2017).

Hill, E. P. & Sussman, A. S. Development of Trehalase and Invertase Activity in Neurospora. *J Bacteriol* **88**, 1556-1566 (1964).

Kanamori, K., Legerton, T. L., Weiss, R. L. & Roberts, J. D. Effect of the nitrogen source on glutamine and alanine biosynthesis in Neurospora crassa. An in vivo 15N nuclear magnetic resonance study. *J Biol Chem* **257**, 14168-14172 (1982).

Kanehisa, M., Sato, Y., Kawashima, M., Furumichi, M. & Tanabe, M. KEGG as a reference resource for gene and protein annotation. *Nucleic Acids Res* **44**, D457-D462, doi:10.1093/nar/gkv1070 (2016).

Kim, J. D., Kaiser, K., Larive, C. K. & Borkovich, K. A. Use of 1H nuclear magnetic resonance to measure intracellular metabolite levels during growth and asexual sporulation in Neurospora crassa. *Eukaryot Cell* **10**, 820-831, doi:10.1128/EC.00231-10 (2011).

Koczula, K. M. *et al.* Metabolic plasticity in CLL: adaptation to the hypoxic niche. *Leukemia* **30**, 65-73, doi:10.1038/leu.2015.187 (2016).

Krishnaiah, S. Y. *et al.* Clock Regulation of Metabolites Reveals Coupling between Transcription and Metabolism. *Cell Metabolism* **25**, 961-974.e964, doi:https://doi.org/10.1016/j.cmet.2017.03.019 (2017).

Kubicek, C. P., Punt, P. & Visser, J. Production of Organic Acids by Filamentous Fungi. *Mycota* **10**, 215-234, doi:Book_Doi 10.1007/978-3-642-11458-8 (2010).

Link, H., Christodoulou, D. & Sauer, U. Advancing metabolic models with kinetic information. *Curr Opin Biotechnol* **29**, 8-14, doi:10.1016/j.copbio.2014.01.015 (2014).

Link, H., Fuhrer, T., Gerosa, L., Zamboni, N. & Sauer, U. Real-time metabolome profiling of the metabolic switch between starvation and growth. *Nat Methods* **12**, 1091-1097, doi:10.1038/Nmeth.3584 (2015).

Link, H., Kochanowski, K. & Sauer, U. Systematic identification of allosteric protein-metabolite interactions that control enzyme activity in vivo. *Nat Biotechnol* **31**, 357-+, doi:10.1038/nbt.2489 (2013).

Magnuson, J. K. & Lasure, L. L. in *Advances in Fungal Biotechnology for Industry, Agriculture, and Medicine* (eds Jan S. Tkacz & Lene Lange) 307-340 (Springer US, 2004).

Maricq, M. M. & Waugh, J. NMR in rotating solids. *The Journal of Chemical Physics* **70**, 3300-3316 (1979).

Markham, P., Robson, G. D., Bainbridge, B. W. & Trinci, A. P. Choline: its role in the growth of filamentous fungi and the regulation of mycelial morphology. *FEMS Microbiol Rev* **10**, 287-300 (1993).

McCluskey, K., Wiest, A. & Plamann, M. The Fungal Genetics Stock Center: a repository for 50 years of fungal genetics research. *Journal of biosciences* **35**, 119-126 (2010).

Milewski, S., Gabriel, I. & Olchowy, J. Enzymes of UDP-GlcNAc biosynthesis in yeast. *Yeast* **23**, 1-14, doi:10.1002/yea.1337 (2006).

Mobarhan, Y. L. *et al.* Comprehensive multiphase NMR applied to a living organism. *Chem Sci* **7**, 4856-4866, doi:10.1039/c6sc00329j (2016).

Mobarhan, Y. L., Struppe, J., Fortier-McGill, B. & Simpson, A. J. Effective combined water and sideband suppression for low-speed tissue and in vivo MAS NMR. *Anal Bioanal Chem* **409**, 5043-5055, doi:10.1007/s00216-017-0450-3 (2017).

Montana, G., Berk, M. & Ebbels, T. in *Software Tools and Algorithms for Biological Systems* (eds Hamid R. Arabnia & Quoc-Nam Tran) 307-315 (Springer New York, 2011).

Patil, R. S., Ghormade, V. V. & Deshpande, M. V. Chitinolytic enzymes: an exploration. *Enzyme Microb Technol* **26**, 473-483 (2000).

Radford, A. Metabolic highways of Neurospora crassa revisited. *Adv Genet* **52**, 165-207, doi:10.1016/S0065-2660(04)52005-9 (2004).

Rhoades, S. D., Sengupta, A. & Weljie, A. M. Time is ripe: maturation of metabolomics in chronobiology. *Current Opinion in Biotechnology* **43**, 70-76, doi:https://doi.org/10.1016/j.copbio.2016.09.007 (2017).

Righi, V. *et al.* In vivo high-resolution magic angle spinning proton NMR spectroscopy of Drosophila melanogaster flies as a model system to investigate mitochondrial dysfunction in Drosophila GST2 mutants. *Int J Mol Med* **34**, 327-333, doi:10.3892/ijmm.2014.1757 (2014).

Rude, T. H., Toffaletti, D. L., Cox, G. M. & Perfect, J. R. Relationship of the Glyoxylate Pathway to the Pathogenesis of Cryptococcus neoformans. *Infection and Immunity* **70**, 5684 (2002).

Sarou-Kanian, V. *et al.* Metabolite localization in living drosophila using High Resolution Magic Angle Spinning NMR. *Sci Rep* **5**, 9872, doi:10.1038/srep09872 (2015).

Sefer, E., Kleyman, M. & Bar-Joseph, Z. Tradeoffs between Dense and Replicate Sampling Strategies for High-Throughput Time Series Experiments. *Cell Syst* **3**, 35-42, doi:10.1016/j.cels.2016.06.007 (2016).

Sekar, K. *et al.* Synthesis and degradation of FtsZ quantitatively predict the first cell division in starved bacteria. *Molecular Systems Biology* **14**, e8623, doi:10.15252/msb.20188623 (2018).

Sengupta, A. *et al.* Deciphering the Duality of Clock and Growth Metabolism in a Cell Autonomous System Using NMR Profiling of the Secretome. *Metabolites* **6**, 23 (2016).

Sitnikov, D. G., Monnin, C. S. & Vuckovic, D. Systematic Assessment of Seven Solvent and Solid-Phase Extraction Methods for Metabolomics Analysis of Human Plasma by LC-MS. *Scientific Reports* **6**, 38885, doi:10.1038/srep38885 https://www.nature.com/articles/srep38885#supplementary-information (2016).

Slayman, C., Long, W. & Lu, C.-H. The relationship between ATP and an electrogenic pump in the plasma membrane ofNeurospora crassa. *The Journal of membrane biology* **14**, 305-338 (1973).

Slayman, C. & Potapova, T. Origin and significance of vacuolar proliferation during nutrient restriction. *Neurospora 2006 Poster Abstracts* (2006).

Slayman, C. L. Electrical properties of Neurospora crassa. Respiration and the intracellular potential. *J Gen Physiol* **49**, 93-116 (1965).

Slayman, C. L., Moussatos, V. V. & Webb, W. W. Endosomal accumulation of pH indicator dyes delivered as acetoxymethyl esters. *Journal of Experimental Biology* **196**, 419-438 (1994).

Slayman, C. L. & Slayman, C. W. Net uptake of potassium in Neurospora. Exchange for sodium and hydrogen ions. *J Gen Physiol* **52**, 424-443 (1968).

Tang, X. *et al.* Systems biology of the qa gene cluster in Neurospora crassa. *PLoS One* **6**, e20671, doi:10.1371/journal.pone.0020671 (2011).

Tredwell, G. D., Bundy, J. G., De Iorio, M. & Ebbels, T. M. Modelling the acid/base 1H NMR chemical shift limits of metabolites in human urine. *Metabolomics* **12**, 152, doi:10.1007/s11306-016-1101-y (2016).

Ulrich, E. L. *et al.* BioMagResBank. *Nucleic Acids Res* **36**, D402-D408, doi:10.1093/nar/gkm957 (2008).

Van Geet, A. L. Calibration of methanol nuclear magnetic resonance thermometer at low temperature. *Anal Chem* **42**, 679-680 (1970).

Virgilio, S., Cupertino, F. B., Ambrosio, D. L. & Bertolini, M. C. Regulation of the reserve carbohydrate metabolism by alkaline pH and calcium in Neurospora crassa reveals a possible cross-regulation of both signaling pathways. *Bmc Genomics* **18**, doi:ARTN 457 10.1186/s12864-017-3832-1 (2017).

Voet, D. & Voet, J. G. *Biochemistry*. (Hoboken, NJ : John Wiley & Sons, ©2011. 4th edition., 2011).

Vrabl, P., Fuchs, V., Pichler, B., Schinagl, C. W. & Burgstaller, W. Organic Acid Excretion in Penicillium ochrochloron Increases with Ambient pH. *Front Microbiol* **3**, 121, doi:10.3389/fmicb.2012.00121 (2012).

Walejko, J. M., Chelliah, A., Keller-Wood, M., Gregg, A. & Edison, A. S. Global Metabolomics of the Placenta Reveals Distinct Metabolic Profiles between Maternal and Fetal Placental Tissues Following Delivery in Non-Labored Women. *Metabolites* **8**, 10 (2018).

Wang, B. *et al.* Identification and characterization of the glucose dual-affinity transport system in Neurospora crassa: pleiotropic roles in nutrient transport, signaling, and carbon catabolite repression. *Biotechnol Biofuels* **10**, doi:ARTN 17 10.1186/s13068-017-0705-4 (2017).

Wayne, L. G. & Lin, K. Y. Glyoxylate metabolism and adaptation of Mycobacterium tuberculosis to survival under anaerobic conditions. *Infection and Immunity* **37**, 1042 (1982).

Wishart, D. S. *et al.* HMDB: the human metabolome database. *Nucleic Acids Res* **35**, D521-D526 (2007).

Wolfinbarger, L. & Kay, W. W. Transport of C4-dicarboxylic acids in Neurospora crassa. *Biochimica et Biophysica Acta (BBA) - Biomembranes* **307**, 243-257, doi:https://doi.org/10.1016/0005-2736(73)90041-2 (1973).

Ye, L., De Iorio, M. & Ebbels, T. M. D. Bayesian estimation of the number of protonation sites for urinary metabolites from NMR spectroscopic data. *Metabolomics* **14**, 56, doi:10.1007/s11306-018-1351-y (2018).

CHAPTER 3

UNCOVERING LATENT METABOLIC PHENOTYPES IN A CLASSIC *NEUROSPORA* MUTANT USING DYNAMIC METABOLOMICS MEASUREMENTS [1]

[1] Judge, M. T. *et al.* To be submitted to *Nature Communications*.

Abstract

The Quinic Acid (QA) gene cluster provides the enzymes and regulatory mechanisms for *Neurospora crassa* to utilize QA as a sole carbon source. The pathway has been model for eukaryotic biochemical networks and their regulation since its key steps were worked out by Case, Giles, and colleagues. The function of *qa-x*, however, has remained elusive despite the availability of a mutant strain (Δ*qa-x*) for decades. We hypothesized that *qa-x* either assists in QA flux to central carbon metabolism or exerts broader control over QA metabolism. Continuous *in vivo* monitoring of metabolism by NMR (CIVM-NMR) revealed latent metabolic phenotypes in the mutant, including net ethanol flux reversal. We demonstrate that this metabolic shift is triggered by quorum sensing in both the mutant and the wild-type, and that the density threshold for quorum is lower in the mutant. Homogentisic acid accumulation in the mutant indicates a *qa-x* function downstream of the anabolic QA pathway en route to the TCA cycle and accounts for the one known Δ*qa-x* phenotype. Finally, initial data indicate that known *Saccharomyces* quorum sensing signals do not induce the quorum response.

Introduction

Neurospora crassa has been a key model organism for fundamental biochemistry, genetics and metabolism research for over 75 years (Beadle and Tatum, 1941). It is robust and easy to grow with limited nutritional requirements, which greatly simplifies metabolic experiments. It also grows as a haploid organism, simplifying interpretation of biochemical mutants (Davis and de Serres, 1970). Beadle and Tatum's approach took advantage of these properties to demonstrate the genetic underpinnings of metabolism in auxotrophic *Neurospora* mutants. Indeed, one of these first auxotrophs was a tryptophan biosynthesis mutant (Beadle and Tatum, 1945). The working out of other aromatic biosynthesis steps in *Neurospora* led to

discovery of the *arom* gene cluster with the exception of one dehydroquinase (DHQ) which curiously lacked a mutant (Tatum, Gross, Ehrensvard, and Garnjobst, 1954; Gross and Fein, 1960; Giles et al., 1967, Gaertner et al. 1977; Lumsden and Coggins 1977).

The discovery that *Neurospora* has both an inducible and a constitutive DHQase (I-DHQase and C-DHQase, respectively) led to the proposal that the *arom* cluster sequesters aromatic flux for aromatic amino acid (AAA) biosynthesis, and explained the frustrated isolation of mutants for both in screens for AAA auxotrophs (Giles et al. 1967). In a stroke of luck, a mutant recovered (*qa-1*) in which I-DHQase remained repressed, thus allowing capture of a C-DHQase mutant (*arom-9*) which mapped to the *arom* locus (Rines, Case and Giles 1969). This mutant allowed recovery of an I-DHQase (*qa-2*) mutation (Giles et al., 1985). Case isolated two other classes of QA catabolism mutants (*qa-3* and *qa-4*) which were characterized as QA/SA dehydrogenase and DHS dehydratase, respectively (Chaleff 1974; Giles et al., 1985). A series of heterokaryon complementation studies, reviewed in Giles et al. (1985) and sequencing (Huiett et al. 1986), showed *qa-1* was actually two genes: the *qa-1F* (fast-complementing) activator for the cluster, and the *qa-1S* (slow-complementing) repressor. The default (uninduced) state of the *qa* cluster is strong repression by *qa-1S*. QA inducer likely binds *qa-1S* directly (Arnett 2009), leading to release of the cluster from repression and *qa-1F*-dependent activation, which also extends to ~ 50 other qa-responsive genes (Tang et al. 2011).

The cloning of the *qa* cluster into plasmids in *E. coli* (Schweizer et al. 1981) enabled precise mapping of the QA-induced transcripts, which led to the unexpected discovery of two more structural genes in the cluster, *qa-y* and *qa-x* (Patel et al. 1981). *qa-y* and *qa-1S* deletion mutants, and another mutant with disrupted *qa-x* (Δ*qa-x*) were obtained through a gene replacement approach (Case et al. 1992). The gene *qa-y* was deduced to be as selective QA

importer; however, Δ*qa-x* exhibited no obvious phenotype aside from the accumulation of a brown substance in liquid media after QA feeding (Case et al. 1992). *qa-x* remains the only *qa* cluster gene of unknown function to date.

The protein sequence for *qa-x* has been computationally annotated as an inositol monophosphatase or magnesium-binding protein (FungiEnsemble.org). Mixed evidence suggests potential *qa-x* roles in carbon catabolite repression (CCR), which exerts strong influence over *qa* cluster expression (Giles et al. 1985; Arnett et al. 2009). On the one hand, *qa-x* induction by QA is relatively weak, but it is strongly expressed under starvation unlike the other structural genes (Giles et al. 1985; Case et al 1992). On the other, CCR of *qa-y* occurs independently of *qa-1S* and *qa-x*, and *qa-y* may mediate CCR by exclusion of QA inducer from the cell (Arnett et al. 2009). While exogenous induction of *qa-x* is dependent on *qa-1F* and *qa-1S*, *qa-1S* repression does not prevent *qa-x* upregulation during starvation, nor is the increase explained by internal induction (Giles et al. 1985). As such, it seems likely that *qa-x* is activated by another regulator, despite *qa-1S* repression. In fact, the bulk of *qa-x* expression was earlier than that of the rest of the *qa* cluster in a shift from starvation to QA (Battogtokh et al. 2002).

Connections with the CRE system (Sun and Glass 2011) have been proposed (Arnett et al. 2009). In Aspergillus, CreA affects regulation of amino acid, glycogen, and ethanol metabolism. CreA and alcR regulate the ethanol utilization gene cluster in an antagonistic relationship (Fillinger et al. 1995; de Assis et al. 2021). Model-guided (Battogtokh et al. 2002, Kochut et al. 2003, Logan et al. 2007) microarray experiments have separated the transcriptional networks controlling starvation and true QA response, and an additional QA response transcription factor connected to fatty acid catabolism was identified (Hynes et al. 2006; Tang et al. 2011). Positive control of several key flux regulation points in metabolism were indicated,

including connections to TCA cycle, ethanol metabolism, glycogenolysis/gluconeogenesis, and amino acid metabolism (Tang et al. 2011). One might therefore expect to find differences in the above metabolic modules in a *qa-x* mutant.

Here, we test this hypothesis and employ a recently developed approach to the questions of CCR and *qa-x* function. Direct, untargeted measurement of metabolite pools by Continuous *in vivo* monitoring of metabolism by NMR (CIVM-NMR) has allowed resolution of dynamic metabolic phenotypes in *Neurospora* (Judge et al., 2019). In probing the mutant for latent metabolic phenotypes, we uncovered a quorum-sensing mechanism that implicates *qa-x* in diversion of flux to aromatic amino acid biosynthesis in the *qa* gene cluster.

Results

Δ*qa-x* phenotype is QA-dependent and suggests oxidation of an extracellular metabolite

We first sought to optimize accumulation of pigment in liquid media, the only known phenotype of Δ*qa-x* (Case et al. 1992; Arnett et al. 2009). A pink-brown color accumulated in the mutant in Vogels arom-complete (supplemented with aromatic amino acids) media using quinic acid (QA) as the carbon source. Cultures grew normally and, after roughly 1 week, color began to appear in Δ*qa-x*-conditioned media. This color deepened greatly over the course of three weeks (Fig. 3.1A), and was retained in the media after filtering out cells. No color was observed in OR74A wild-type (WT) cultures, or in glucose- or sucrose-fed cultures. (Fig. 3.1B).

As such, we concluded that at least one compound in the media (either secreted or modified) must differ between the mutant and the WT. We reasoned that increased QA would drive higher accumulation of this compound, and found that, given pH was controlled, this was correct (Fig. 3.1C). The weeks-long timescale of color evolution from pink to brown color also

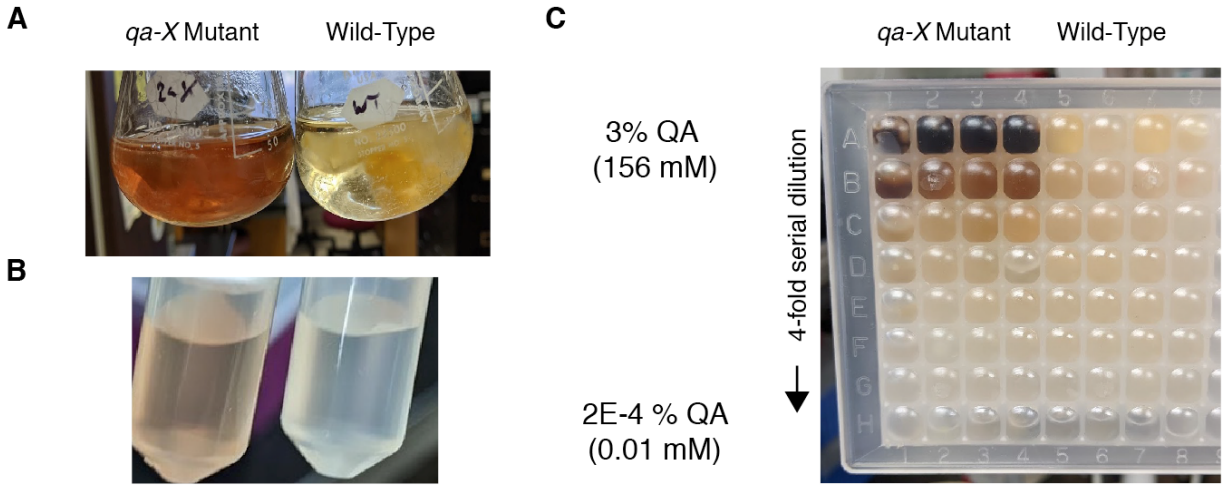

Figure 3.1. Δ*qa-x* (left) imparts a red-brown color to liquid cultures when grown on quinic acid. This color deepens over the course of 1-3 weeks in standing cultures. The wild-type (right) maintains a golden-clear color throughout. Cultures pictured after 2.5 weeks on the bench. B. Color remains after *Neurospora* cells are removed by filtration. C. Increasing QA carbon source concentration up to 3% in liquid cultures results in deeper color, although low pH of ~2.75 prohibits growth if not adjusted. Four 1 mL replicates of four-fold dilutions of 3% QA Vogels (pH adjusted with concentrated NaOH from 2.75 to 4.5) were grown aerobically at 30C in an incubator for 1 week, then allowed to sit on the bench for 6 weeks.

suggested that oxidation products were being formed from an initial compound accumulation. In line with this hypothesis, when bleaching younger cultures which lacked visible color, we noticed an immediate transformation from clear to pink-brown. Combined, these data suggest the accumulating compound is related to QA metabolism. We then turned to Continuous *in vivo* Metabolism-NMR (CIVM-NMR) (Judge et al. 2019) to test for potential differences in metabolite pool dynamics.

Δ*qa-x* and WT metabolite pools differ under starvation.

One of the hallmarks of the *qa-x* gene is its strong upregulation upon shifting from glucose to starvation (Giles et al. 1985; Case et al 1992). To probe differences in starved metabolism in a mutant lacking that activity, we instituted a 1 h period in minimal media (Figure 3.3, yellow spectra) before spiking of the QA carbon source for a WT and a *qa-x* mutant culture. During this period, the WT accumulated ethanol (Figure 3.3A). This was expected, as we have noted a symmetric 24h accumulation and reduction of the ethanol pool in long starvation runs in other strains, and ethanol accumulation under starvation. Alanine also was accumulated in both strains, but did so more rapidly in the wild type (Figure 3.3A). Free amino acids accumulated slightly which is also typical for CIVM-NMR runs, as did choline and a neighboring singlet at 3.2 ppm (Figure 3.3A,B). Succinate accumulated quickly in the wild type, but did not appear in the mutant (Figure 3.3C). This indicates an anaplerotic state of the TCA cycle in the mutant during starvation, but cataplerotic in the WT. Inversely, glucose-1-phosphate (G-1-P) and potential sugar pools rose rapidly during starvation in the mutant, but were maintained at low levels in the WT (Figure 3.3D). This is consistent with liberation of glucose and G-1-P from glycogen and rapid utilization in ethanolic fermentation in the WT, e.g. as an inhibitor to other organisms (Xie et al. 2004). An inability for the mutant to utilize this flux effectively could lead to G-1-P accumulation, and a lack of succinate accumulation. Broadly, these trends in central metabolites also indicated that metabolism was not equalized during metabolism, perhaps because of different regulation of flux utilization from glycogenolysis.

Δ*qa-x* and WT ethanol pools differ under QA feeding.

The cultures were then spiked to 3% QA with concentrated addition solution, which resulted in significant and immediate changes. In contrast to glucose feeding in our previous

study (Judge et al. 2019), the WT culture consumed ethanol and choline along with QA (Figure 3.3B). This is consistent with the knowledge that ethanol can be utilized as a carbon source by *Neurospora*, and may reflect a change in NAD:NADH balance (Xie et al. 2004). QA was readily consumed by the WT, but decreased to a lesser extent in *qa-x*. This may suggest a bottleneck in QA metabolism (regulatory, stoichiometric, or enzymatic deficiency) in the mutant. Pools of G-1-P and the putative sugar at 5.39 ppm depleted rapidly in both strains upon feeding (Figure 3.3D). A set of aromatic peaks accumulated 6.7 ppm was present in Δ*qa-x* culture, but not in the WT (Figure 3.3D). If more central carbon flux were coming from these sources, perhaps QA utilization would be lower.

With the exception of G-1-P and succinate fluxes, trends in most metabolites in the mutant appeared to be consistent with the previous starvation period in the culture. This is perhaps expected; *qa-x* is unique in the *qa* cluster in that it is upregulated under starvation, and is likely implicated in both QA and starvation responses. Remarkably, Δ*qa-x* exhibited ethanol and choline production despite slower QA consumption, indicating a major metabolic differences in the mutant in response to QA (Figure 3.3A, B). Succinate accumulated rapidly in the mutant upon feeding, but more in the WT, and fell just as rapidly as it accumulated in both strains (Figure 3.3C).

In Tang et al. the transcriptional response to QA induction from sucrose is detailed. Several points of consistency with the present dataset can be made with caution (although the modules reported in the paper are specific to QA induction, our data are a shift from starvation). The additional transcription factor (NCU03643; QA-responsive cutinase transcription factor-1β; CTF1β) regulating response to QA is highly conserved in filamentous ascomycetes, and is required for fatty acid catabolism in *Aspergillus* (Hynes et al. 2006). If the QA response

mediated by this TF were modified in the mutant, we may expect to see a change in the amount of fatty acid metabolism. Indeed, we observed choline accumulation (Figure 3.3B) in the mutant, which continued to accumulate from the starvation period through QA feeding in Δ*qa-x*. Second,

Figure 3.3. Net ethanol flux is reversed in dense *qa-x* mutant cultures. (A) Ethanol was present in the media (blue spectrum; from biotin solution) and remained upon spiking quinic acid (red) to 3% (pH-adjusted) in the media blank. Under 1h starvation (yellow spectra), ethanol accumulated further in both cultures. Alanine levels increased more in the wild type during the starvation. Upon quinic acid spiking to the organism (purple spectra), alanine and free amino acid residues rose quickly in the wild type and the mutant, but more in the WT. Ethanol was consumed by the WT, but produced for the first half of the mutant culture. **(B)** Choline (3.18 ppm) accumulated strongly in the mutant, and less so in the Wild-type (WT) during starvation (yellow). Upon QA feeding, choline increased in the mutant, but decreased in WT. A singlet at 3.2 ppm (possibly a choline derivative) increased in WT, but remained constant in the mutant. **(C)** Succinate (leftmost peak starting at ~2.5 ppm) accumulated strongly in the WT, but not the mutant, during starvation (yellow). Upon QA feeding, succinate accumulated then decreased for both strains. Much higher levels were produced in the WT. A pH-sensitive triplet starting at 2.3 ppm and a broad peak at 2.4 ppm both increased throughout the WT run, but were not detected in the mutant. **(D)** G-1-P (5.48 ppm) and a putative maltose or ribose peak at 5.39 ppm accumulated in the mutant during 1h starvation (yellow spectra), and were depleted after feeding. These compounds did not accumulate strongly in the WT. Additionally, aromatic peaks at 6.7 ppm accumulated strongly with QA feeding in the mutant, but not in the WT. Tyrosine accumulated more in the WT.

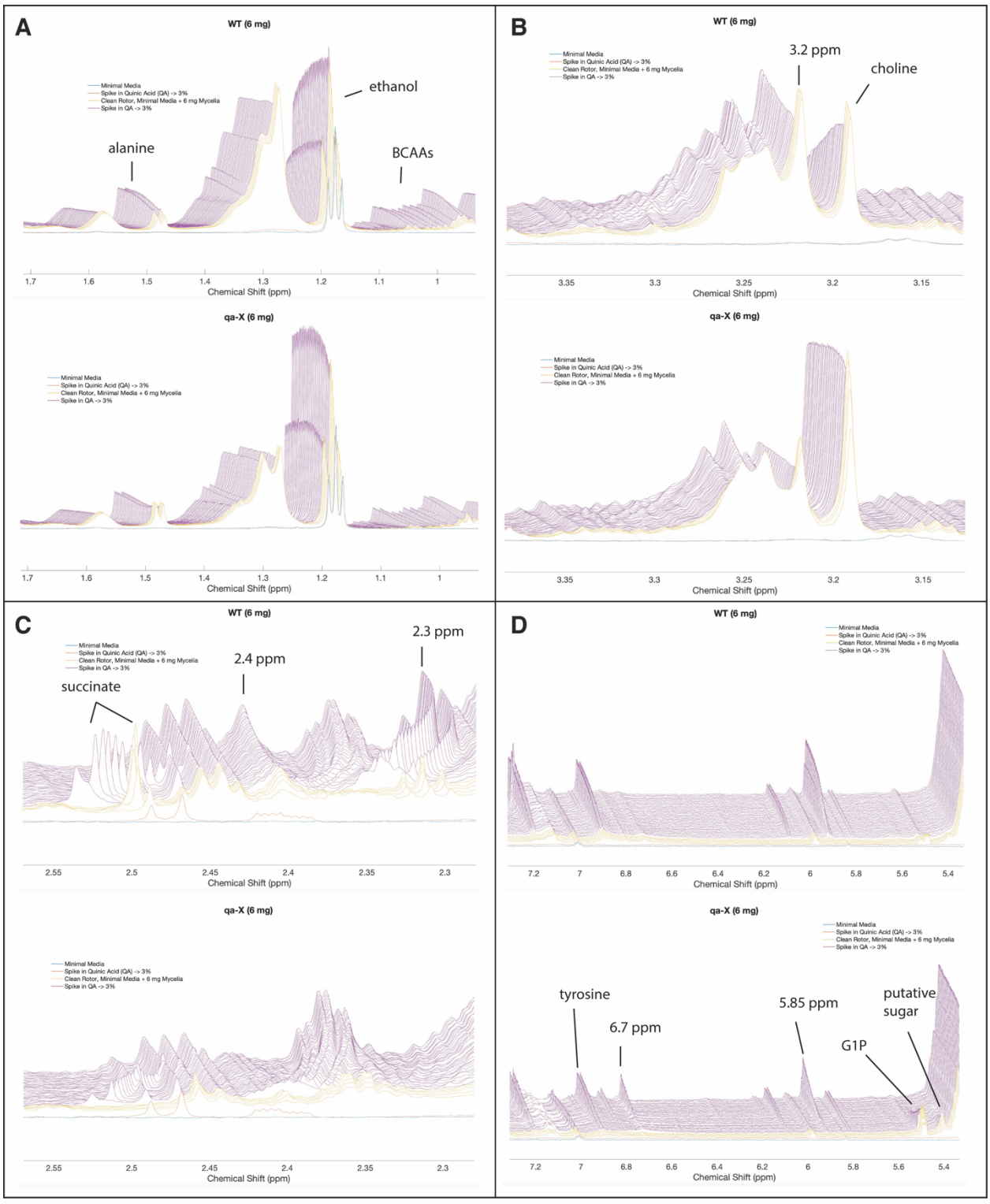
A
WT (6 mg)
Minimal Media
Spike in Quinic Acid (QA) -> 3%
Clean Rotor, Minimal Media + 6 mg Mycelia
Spike in QA -> 3%
alanine
ethanol
BCAAs
1.7
1.6
1.5
1.4
1.3
1.2
1.1
1
Chemical Shift (ppm)
qa-X (6 mg)
Minimal Media
Spike in Quinic Acid (QA) -> 3%
Clean Rotor, Minimal Media + 6 mg Mycelia
Spike in QA -> 3%
1.7
1.6
1.5
1.4
1.3
1.2
1.1
1
Chemical Shift (ppm)
B
WT (6 mg)
Minimal Media
Spike in Quinic Acid (QA) -> 3%
Clean Rotor, Minimal Media + 6 mg Mycelia
Spike in QA -> 3%
3.2 ppm
choline
3.35
3.3
3.25
3.2
3.15
Chemical Shift (ppm)
qa-X (6 mg)
Minimal Media
Spike in Quinic Acid (QA) -> 3%
Clean Rotor, Minimal Media + 6 mg Mycelia
Spike in QA -> 3%
3.35
3.3
3.25
3.2
3.15
Chemical Shift (ppm)
C
WT (6 mg)
Minimal Media
Spike in Quinic Acid (QA) -> 3%
Clean Rotor, Minimal Media + 6 mg Mycelia
Spike in QA -> 3%
succinate
2.4 ppm
2.3 ppm
2.55
2.5
2.45
2.4
2.35
2.3
Chemical Shift (ppm)
qa-X (6 mg)
Minimal Media
Spike in Quinic Acid (QA) -> 3%
Clean Rotor, Minimal Media + 6 mg Mycelia
Spike in QA -> 3%
2.55
2.5
2.45
2.4
2.35
2.3
Chemical Shift (ppm)
D
WT (6 mg)
Minimal Media
Spike in Quinic Acid (QA) -> 3%
Clean Rotor, Minimal Media + 6 mg Mycelia
Spike in QA -> 3%
7.2
7
6.8
6.6
6.4
6.2
6
5.8
5.6
5.4
Chemical Shift (ppm)
qa-X (6 mg)
Minimal Media
Spike in Quinic Acid (QA) -> 3%
Clean Rotor, Minimal Media + 6 mg Mycelia
Spike in QA -> 3%
tyrosine
6.7 ppm
5.85 ppm
G1P
putative
sugar
7.2
7
6.8
6.6
6.4
6.2
6
5.8
5.6
5.4
Chemical Shift (ppm)

upregulation of *gla-1* suggests glycogenolysis or gluconeogenesis, which we see evidence for in both strains. This was a much stronger trend in the mutant, as the strong accumulation of G-1-P in starvation is depleted after the switch to QA. Third, phospho-enol-pyruvate (PEP) carboxykinase was also highly expressed in the Tang et al. study, suggesting flux from oxaloacetate to PEP under starvation, i.e. net flux out of the TCA cycle, which ultimately ends up going to gluconeogenesis, pyruvate and ethanol (accumulates in the mutant), or aromatic biosynthesis via DAHP (aromatic peaks, including tyrosine and phenylalanine increase in both strains) (cycl.pnnl.gov). The putative aldehyde dehydrogenase may indicate an upregulation of a range of activities, including tryptophan degradation (indole acetaldehyde), gluconeogenesis (G3P and 3PG), and acetaldehyde conversion to acetate (Tang, et al. 2011). The involvement of this regulator in the latter reaction is particularly interesting, as it is a potential chokepoint reaction for ethanol degradation. As we see ethanol accumulation, this step appears to be downregulated in Δ*qa-x*.

Media replacement after CIVM demonstrates *Neurospora* survival and allows for annotation of intracellular and extracellular metabolites.

As a functional metabolic test of whether or not *Neurospora* is significantly altered over the course of a 12-h CIVM-NMR experiment, we removed the mycelia from the rotor after the WT QA feeding experiment, then subjected it to the same sample preparation process used for fresh mycelia and re-ran those mycelia with fresh media in another 12-h CIVM-NMR experiment. Any extracellular enzymes, metabolites, or breakdown products from autolysis should have been removed, or significantly reduced. The CIVM data clearly revealed that metabolic activity observed before (Figure 3.4; pink spectra) media replacement was repeated faithfully (green spectra), with only a slight reduction in rates and stable biomass peak

intensities; these are easily attributed because of the addition of the organism to blank media in the earlier starvation run (media, blue spectrum; media plus 6 mg WT mycelia, black spectra; Figure 3.4). Some reduction in rates and organism peaks is to be expected, as mycelia are inevitably lost during sample prep. Even pH shifts observed in titratable groups moving across the spectrum were reproduced.

This experiment also revealed a powerful property of media replacement steps: one set of peaks exhibited a sharp drop in intensity across the media replacement step (Figure 3.4; pink to green), while others retained their intensity (sans slight reduction). The former likely belong to extracellular metabolites, while the latter were typically attributed to biomass and must be secure within the cells. Additionally, as the dilution factor (and the corresponding drop in peak intensity) is easily derived for any carefully controlled partial media replacement (e.g. spiking step), it should be possible to gain information about the location of intracellular and extracellular pools of even the same metabolite in a CIVM run within a degree of statistical certainty. Work is ongoing to systematically categorize our metabolites in this way.

Figure 3.4. CIVM Experiments are exceptionally repeatable with the same mycelia and allow the separation of intracellular and extracellular metabolites. Note the addition of the large quinic acid peaks on either side of the red spectrum in comparison to the blue minimal media spectrum. These quinic acid peaks are absent in the starvation (black spectra), but are added during the spiking step (pink). Repeated metabolism with the same mycelium after washing and a second QA spike (green). Spectra are from the same WT sample discussed above.

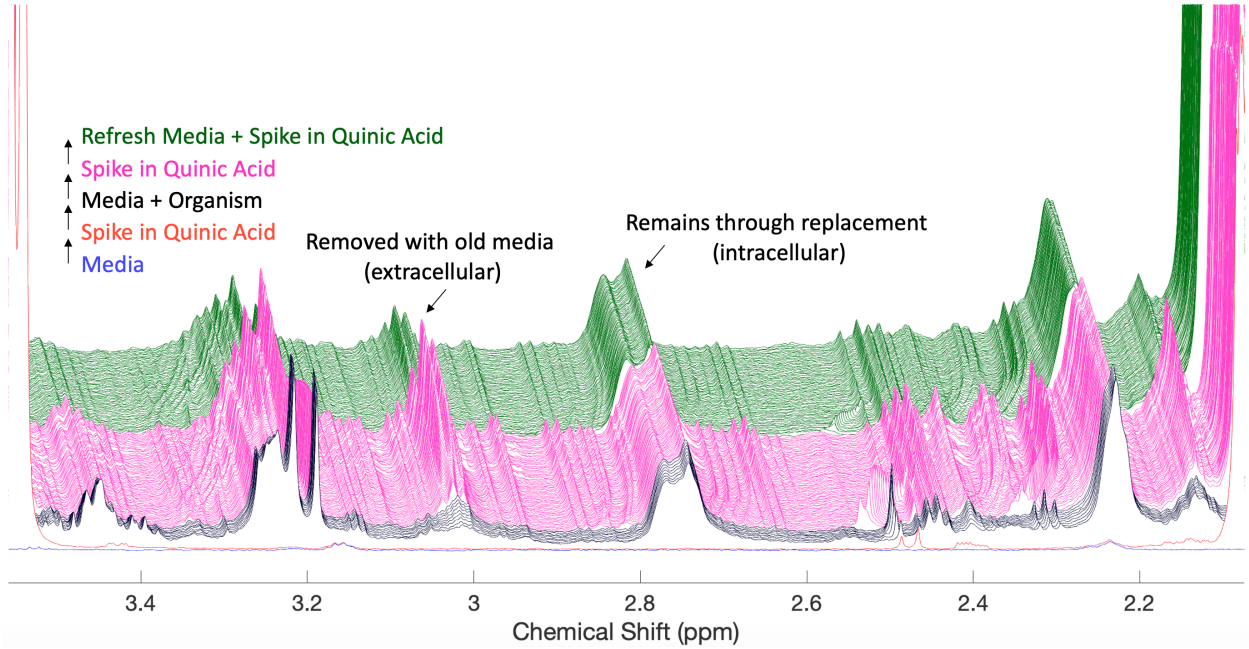

Δ*qa-x* and WT differ across a glucose-QA-starve shift

Given the consistency of our observations with previous transcriptional network models, and previous data which proposed roles for *qa-x* in CCR, we collected the first direct observations of the metabolic shift from CCR to QA feeding *in vivo*. To do so, we sought to recreate at the beginning of a CIVM run the same metabolic state existing in the end of the linear glucose consumption phase of a shaking flask culture, but with QA added. The starvation period was reduced as much as possible (1.5 h to 30 min, including cumulative starvation time from sample rinse, weigh, and organism + media measurement). We reduced the amount of QA to 0.3%, and enough glucose was added to the spiking solution to ensure a few hours of consumption. The idea here was to give time for the transcriptional network to settle into a state of glucose consumption. Mycelia were limited to 1 mg, which is around the same density we achieved routinely in mature shaking flask cultures. As a result, we observed for each strain a glucose-to-quinic shift and a fed QA-to-starvation shift within continuous 30-h run.

Glucose metabolism proceeded immediately and continued for the first 5-7h upon addition as described previously (Judge et al. 2019) for the WT and Δ*qa-x*, indicating successful CCR (Figure 3.5). As glucose was consumed, ethanol and succinate pools increased to significant amounts. In the WT, choline was also consumed rapidly, while in the mutant, the choline pool decreased at a much slower rate until a marked switch to rapid consumption coincident with glucose depletion. Thus it appears that glucose catabolism, and likely CCR, inhibited choline catabolism or increased choline production in the mutant. This would be consistent with altered CTF1β activity, were that or a similar factor to mediate CCR of the *qa* cluster (Tang et al. 2011).

An unexpected finding was that QA appeared to increase by ~5% during WT glucose consumption (Figure 3.5, top), suggesting flux from glycolysis and pentose phosphate pathway (PPP) activity overflowing into DAHP driven by mass action. DAHP is constitutively converted by DHQ synthase (*arom-2*) to DHQ, which can be converted to QA by QA-induced QA dehydrogenase (*qa-3*). This hypothesis will be tested in future work by adding ^{13}C glucose with QA present, resulting in production of ^{13}C QA. On the other hand, in the *qa-x* culture, ~5-10% of the QA appeared to be utilized during glucose consumption (Figure 3.5, bottom). As the *qa* cluster should be suppressed by the presence of rich carbon sources such as glucose, this may indicate that CCR is leaky in Δ*qa-x*. *qa* cluster transcripts could be measured under combined glucose/QA feeding to confirm or refute this.

Glucose depletion resulted in rapid, widespread changes in metabolism (Figure 3.5). This reflects a similar transition to the sucrose to QA shift observed in Tang et al. (2011). In both cultures succinate mirrored its rapid 2h production with 2h of consumption. In the mutant, consumption of ethanol and QA began at this point as well, and continued to increase for 5-7h, in

line with known *qa* cluster induction timescales (Giles et al. 1985; Battogtokh et al. 2002). The rate of QA consumption initially slowed following glucose depletion, while choline consumption sped up, suggesting several potential hypotheses. First, glucose consumption is needed to fuel some part of QA metabolism in the mutant, and succinate does not appear to suffice for that purpose. Alternatively, the QA consumption pathway(s) may be flooded with flux from succinate, ethanol, and choline while these metabolites are present, as the rate of QA consumption steadily increased following coincident depletion of succinate and choline. Succinate depletion was followed by a short-lived increase in the rate of QA consumption in the WT, which suggests the fluxes are linked.

Other metabolites began to accumulate at this point as well, including aromatic peaks (likely aromatic amino acids). Both cultures proceeded relatively linearly across all metabolites during QA/EtOH consumption, until QA depletion when the rate of EtOH consumption increased sharply. In both strains, EtOH and QA consumption appear to be linked tightly, suggesting common metabolic pathways, cofactors, or regulation. Kinetic modeling as in (Pfister et al. 2019), extended to CIVM in Wu et al. 2021 (in review), will be useful in gaining confidence in these links, whether they are flux- or regulation-related. However, the most striking result from these experiments was that Δ*qa-x*, which had previously been characterized by ethanol production during QA feeding, consumed ethanol like the WT upon glucose depletion, constituting a reversion of the ethanol flux phenotype in the mutant.

Δ*qa-x* mutant metabolism reveals a quorum sensing behavior in *Neurospora*

The first set of CIVM conditions (6 mg/rotor cell density, 1.5 h starvation, 3% QA, absence of glucose) were repeated for Δ*qa-x*, and production of ethanol with QA feeding was

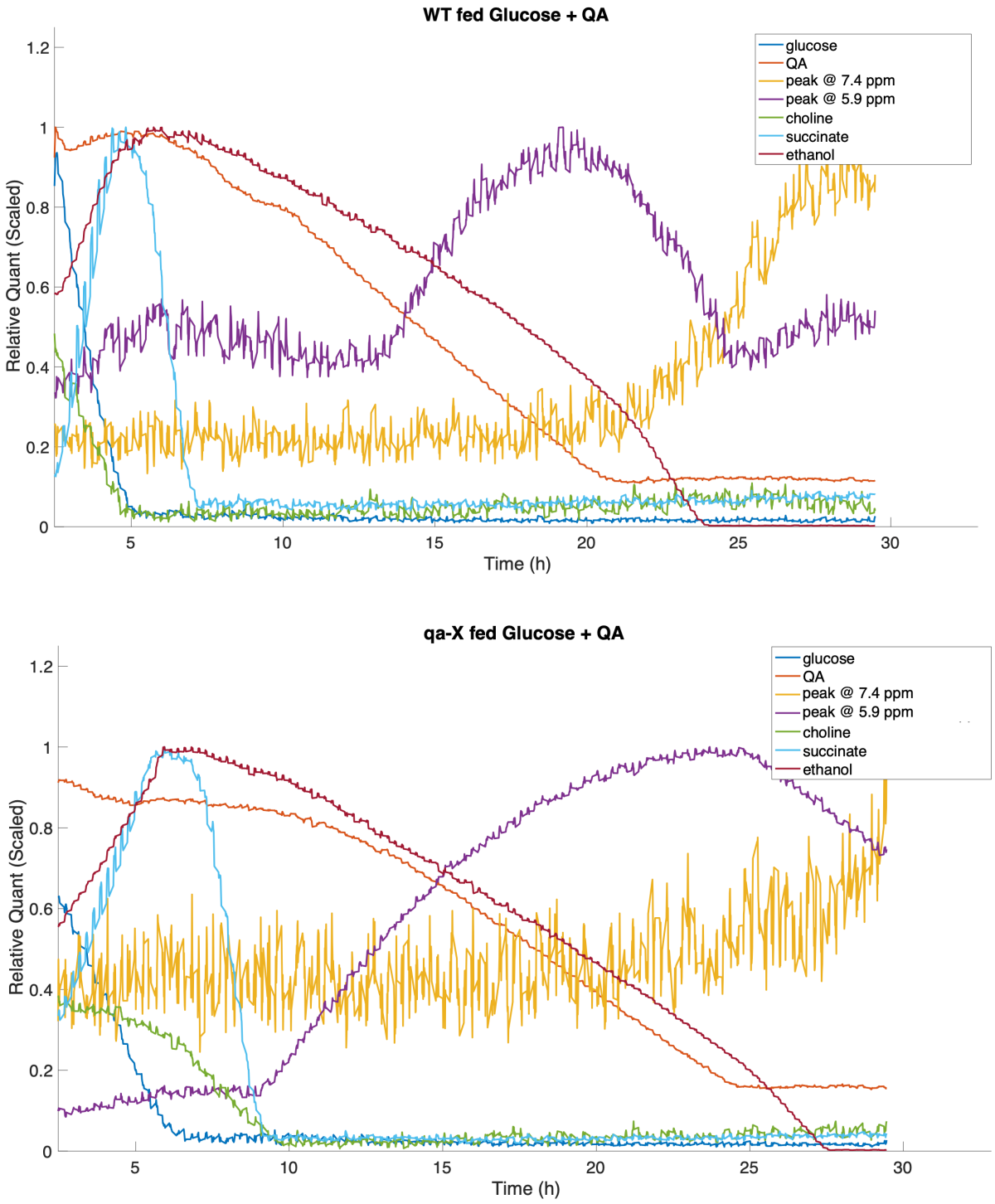

Figure 3.5. Ethanol production was not observed in low-density, glucose + QA media in the mutant. Differences were observed in metabolite dynamics between the WT (top) and Δ*qa-x* (bottom).

confirmed as this was the culture exhibiting the unusual increase in ethanol. We then began altering the culture conditions systematically to determine whether glucose feeding, higher cell density, longer starvation, or higher QA concentration resulted in this reversal of net ethanol flux in Δ*qa-x*. Next, 1 mg of mycelia with no glucose resulted in ethanol consumption, excluding glucose feeding as the causal factor. Next, 6.3 mg mycelia was spiked with 0.3% QA and no starvation, resulting in ethanol production, indicating that starvation was not sufficient to induce WT consumption of ethanol in the mutant. Finally, mycelia were reduced to 1 mg and fed 0.3% QA with no starvation and no glucose, resulting in WT-like ethanol consumption. Further Δ*qa-x* CIVM experiments were run under these same conditions, but varying from 0.55 mg/rotor – 6.3 mg/rotor to produce a metabolomic readout across a cell density gradient. From these data (Fig. 3.6), a clear density-dependent gradient in most metabolite profiles was observed with expected kinetics (accumulation/depletion rates and maximum accumulation levels had strong positive correlations with mycelial density). However, a sharp shift occurs in the ethanol trajectories. Above 1.5 mg/rotor, peak ethanol accumulation and QA consumption occur in a density-dependent manner (less density, less and slower ethanol accumulation). However, below 1.1-1.5 mg/rotor, ethanol was consumed with QA.

Δ*qa-x* lowers the threshold for the density-dependent shift

Above 1.71 mg/rotor (Figure 3.6 and 3.7), as *qa-x* densities decrease, QA is consumed more slowly. At a point between 1.06 and 1.71 mg/rotor, however, the rate of QA consumption undergoes a jump discontinuity resulting in the fastest consumption of QA, faster than even the highest density cultures. From that point, lower density is once again correlated with slower metabolism (note that 0.55 mg is still a low-density profile, but is slow enough to overlap with high-density cultures. Thus, we conclude that there is a sharp and discontinuous metabolic

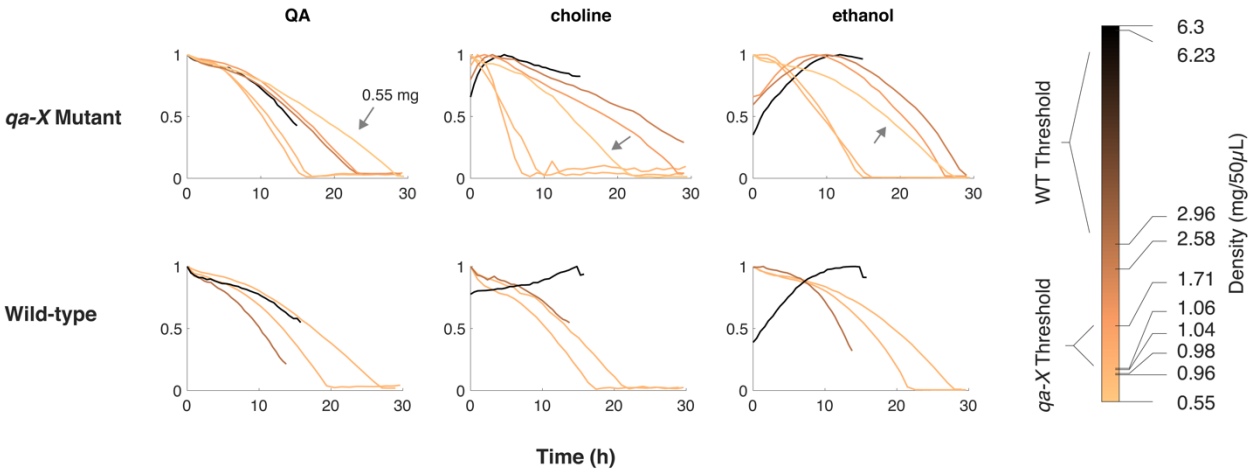

Figure 3.6. Scaled Δ*qa-x* mutant metabolite profiles reveal a cell density threshold which triggers a large scale shift in metabolism. Note that the rate of QA consumption in both strains above the density threshold increases with density (darker lines steeper). However, there is a sudden shift to even faster rates with lower density (lighter lines steepest). The exception is the 0.55 mg Δ*qa-x* culture (gray arrow), which is easily confused for a high-density phenotype, in fact reflects a much slower low-density phenotype. WT metabolite profiles reveal a density threshold much higher than the one observed in Δ*qa-x*. Optimal QA and ethanol consumption occur in the ~1 mg *qa-x* cultures, but occur at ~2.96 mg in the WT. Note that this culture falls into the low-density phenotype. The optimal density is therefore the highest allowed below the density threshold.

switch between high and low mycelial density cultures under QA feeding. This boundary in the mutant appears to lie between 1.06 and 1.7 mg/rotor, and is in the range of the densities achieved in shaking flask cultures, suggesting a common mechanism for cell density regulation in *Neurospora*. A similar gradient of CIVM-NMR runs was also produced for the WT (Figure 3.8). Remarkably, this transition occurs at a much higher density in the WT (> 3 mg/rotor), implicating *qa-x* in production, detection, or metabolic response to this mechanism.

HGA accumulates in the Δ*qa-x* strain

Density-matched comparisons of the WT and the Δ*qa-x* cultures revealed major differences in one of the sets of aromatic peaks (6.7 and 6.8 ppm) noted earlier which strongly distinguished Δ*qa-x* from the WT at all densities; Fig. 3.9). The aromatic metabolite accumulated in all Δ*qa-x* cultures, but did not appear in the WT. We annotated this metabolite as homogentisic acid (homogentisate, HGA), which lies directly downstream of the tyrosine degradation pathway (cyc.pnnl.gov). Tyrosine accumulated twice as much in the WT as in Δ*qa-x* (Fig. 3.7-9). HGA is also known to darken with oxidation or addition of alkali, and accumulations in alkaptonuria patients (lacking HGA oxidase) form a pigmented polymer that underlies the classic ochronotic markers of the genetic disease, darkened urine and spots on the skin. Ironically, Beadle in his Nobel Lecture (1958) explains that this phenomenon was a major influence for his famous experiments with Tatum in *Neurospora* which led to the study of the *qa* cluster. Accumulation of HGA explains the only phenotype observed for Δ*qa-x* preceding this study – a pink/brownish discoloration of liquid QA media after left standing (Case et al. 1992, Arnett et al. 2009), as well as the rapid color change upon addition of bleach solution. HGA offers an alternative route for QA flux into the TCA cycle post-respiration through fumarate and acetoacetate (cyc.pnnl.gov). Thus, both forks of QA metabolism are capable of feeding the TCA cycle, but the canonical catabolic pathway through PCA and B-ketoadipate enters at succinate and therefore requires active respiration to be utilized (Figure 3.10).

Notably, HGA accumulation did not appear to correlate with mycelial density; it simply mirrored QA consumption and decreased upon QA depletion, suggesting that QA flux drives accumulation of HGA in the mutant as we predicted earlier. One implication of this finding in combination with our QA-dependence data is that QA appears to simply be converted

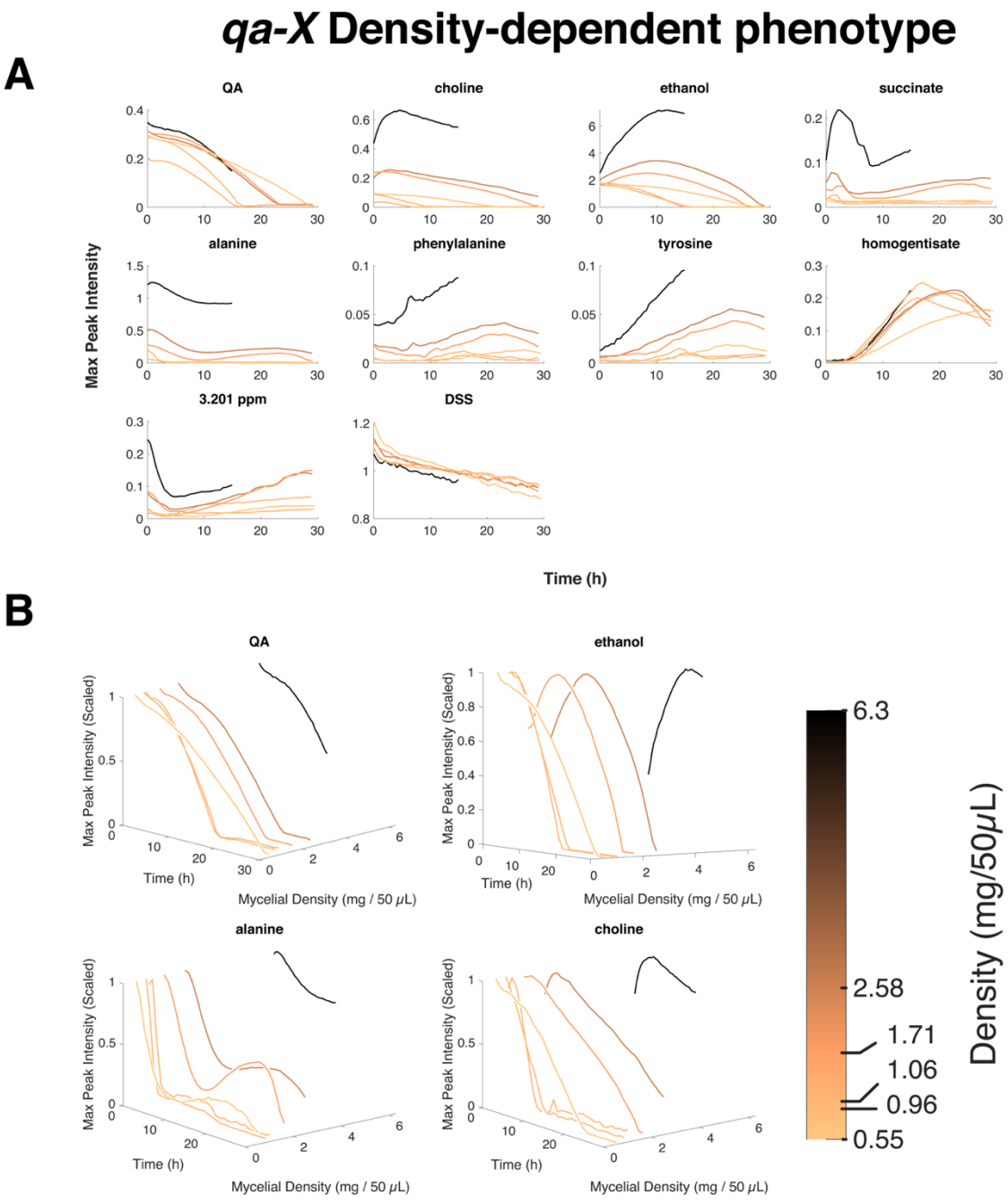

Figure 3.7. Unscaled Δ*qa-x* mutant metabolite profiles show the density-dependent accumulation of important metabolites. Scaled 3D metabolite profiles better illustrate the optimal density for metabolism, which is between 1 and 1.7 mg/50 µL.

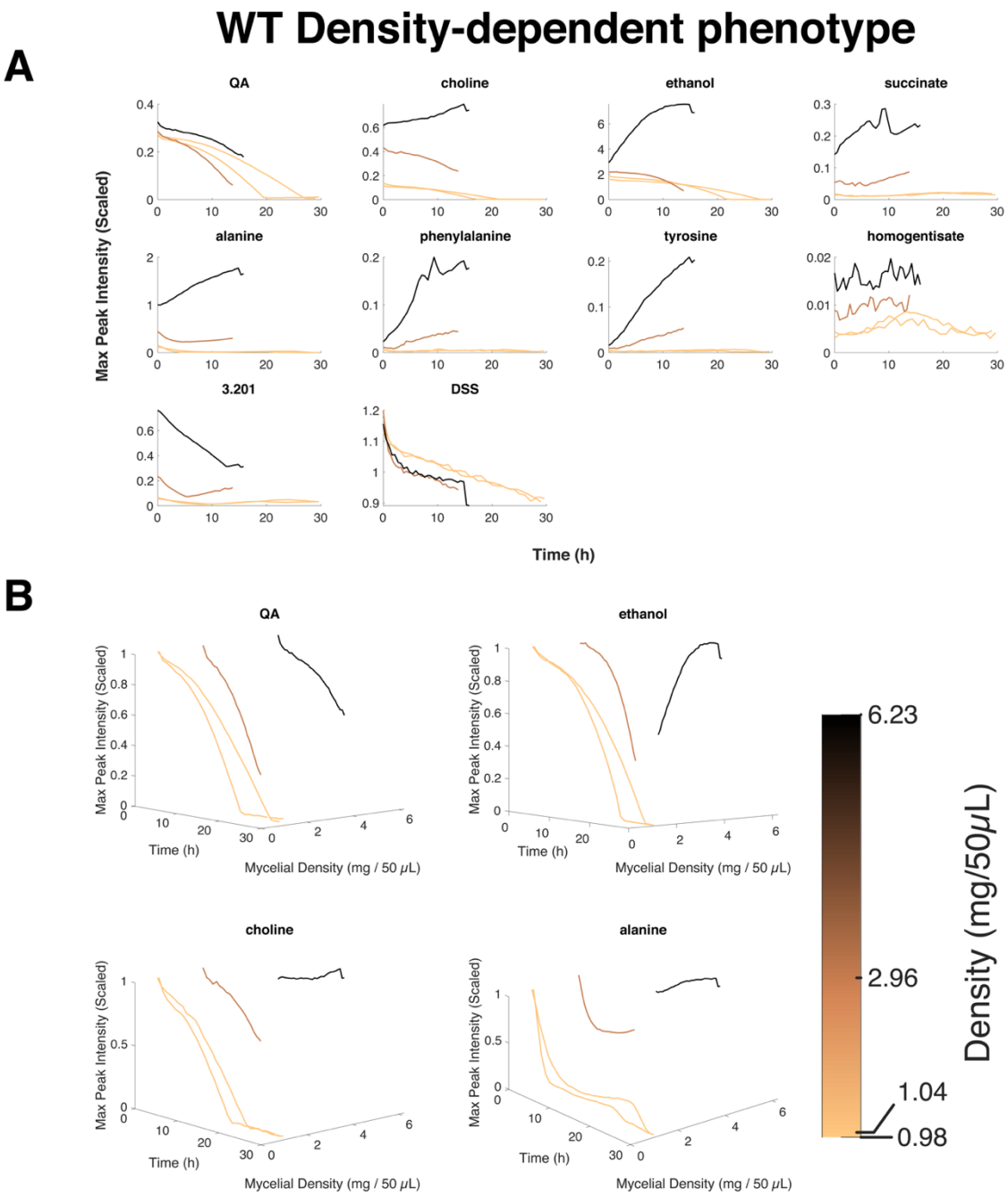

Figure 3.8. Unscaled WT metabolite profiles show density-dependent accumulation of important metabolites. Scaled 3D metabolite profiles better illustrate the optimal density for metabolism, which is between 3 and 6 mg/50 µL. Note that homogentisate quantification reflects noise as this metabolite was not detected in the WT. The drop in DSS and metabolite levels at ~15h in the 6.23 mg condition derives from culture instability at that time.

proportionally to HGA without strong dependence cell density, potentially indicating that HGA is its sole destination in the mutant. ^{13}C-labeled QA fed to a 6 mg Δ*qa-x* culture resulted in accumulation of ^{13}C-QA (and a small amount of ^{13}C-ethanol), confirming this hypothesis (Figure 3.11A-B) while ^{12}C-ethanol followed the characteristic high-density pattern (Figure 3.11C).

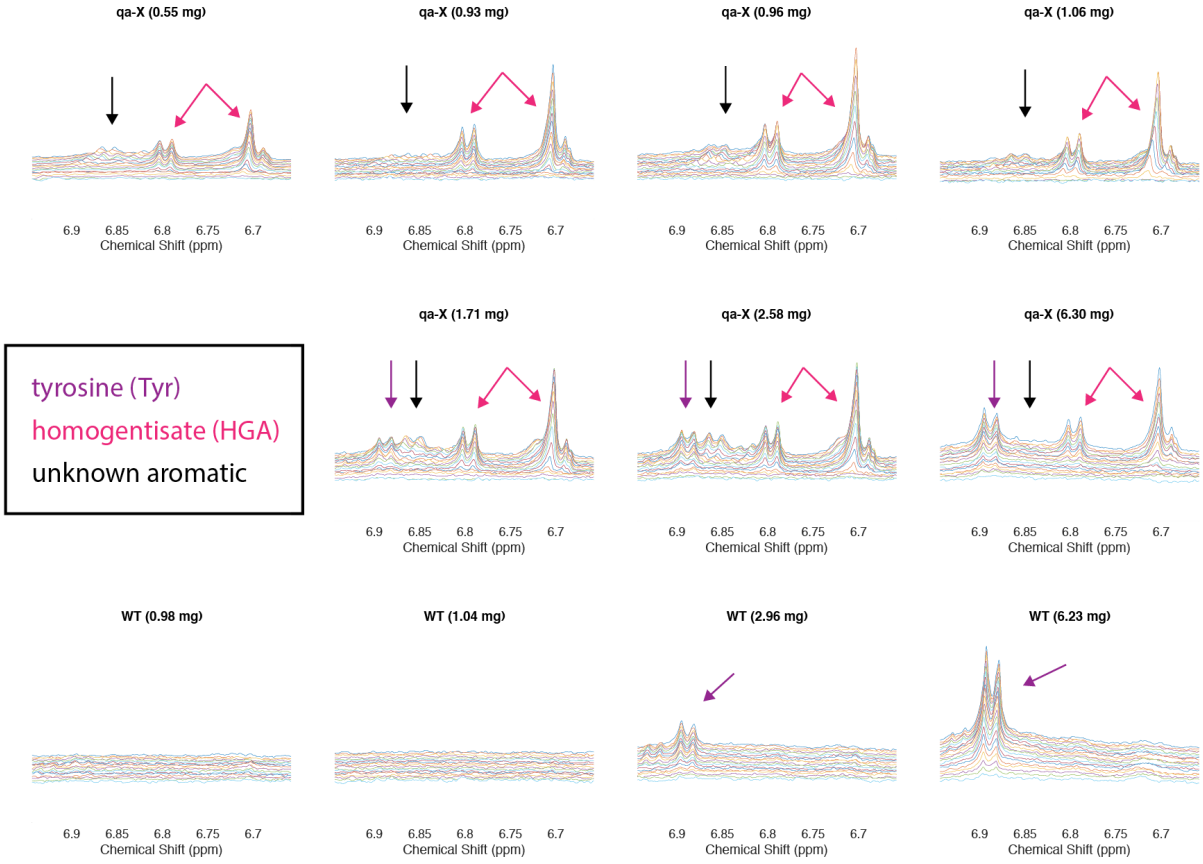

Figure 3.9. Differential accumulation of Tyrosine in the WT and HGA in the mutant. Homogentisate (pink arrows) accumulates strongly in the mutant, but is not detectable in the WT. Tyrosine, an upstream metabolite of HGA in, accumulates more strongly in the WT. HGA accumulation is not density-dependent.

Differential accumulation of aromatics in the WT and Δ*qa-x* mutant

Compared to the mutant, the WT cultures accumulated significantly higher levels of phenylalanine (7.3-7.45 ppm) and tyrosine (6.88 ppm; Figure 3.7-8). Neither were detected in the

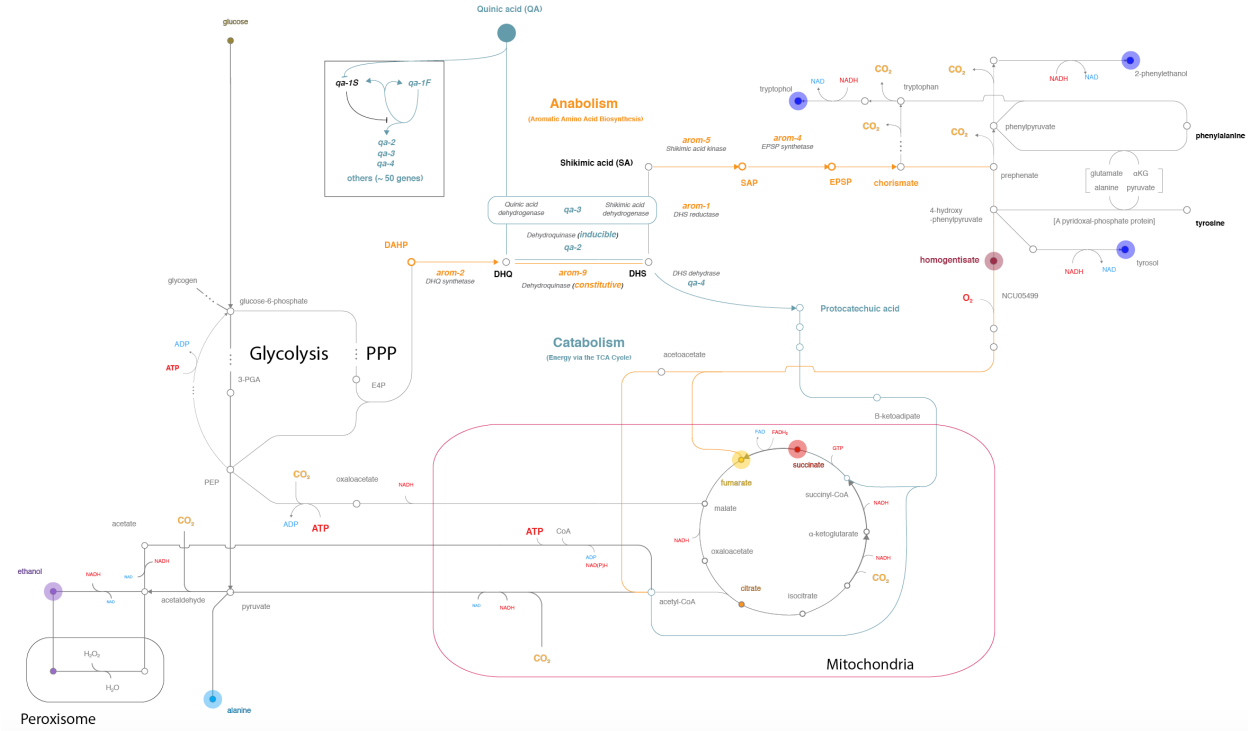

Figure 3.10. The QA pathway has several connections to central carbon metabolism. The QA pathway derives flux from central carbon metabolism and a QA carbon source. It then branches into the QA-induced catabolic (blue) branch, and the constitutive anabolic (orange) branch. The former contributes carbon flux to succinyl-CoA and acetyl-CoA in the TCA cycle via protocatechuic acid (PCA) and the B-ketoadipate pathway, while the latter branches into aromatic amino acids, their aromatic alcohol derivatives (blue circles). The anabolic branch can also contribute carbon to the TCA cycle via homogentisate (maroon), which is oxidized to yield acetoacetate and fumarate, effectively bypassing the electron transport chain which drives succinate conversion to fumarate. Reactions were derived from cyc.pnnnl.gov.

1 mg cultures, but both were density-correlated in both strains above their density thresholds. A convenient effect of performing these reactions at different densities is that it is possible to reason that a metabolite has density dependent accumulation, whereas its absence in a lower-density culture alone may be interpreted differently. This was the case with tyrosine, which did not appear to be present in any of the low-density cultures, but was clearly density-dependent in higher-density cultures (Figs 3.7-9). As its profile approached the limit of detection for both WT and *qa-x*, but was present below the higher density threshold in the WT, it is reasonable to conclude that it is simply below the limit of detection in these cultures. This is important because it suggests that preferential accumulation of phenylalanine and tyrosine is not the cause of the density-dependent shift, but may instead reflect a general underlying pattern that influences the shift. Curiously, we could not reliably annotate tryptophan in our spectra, and potentially associated resonances had very low intensities.

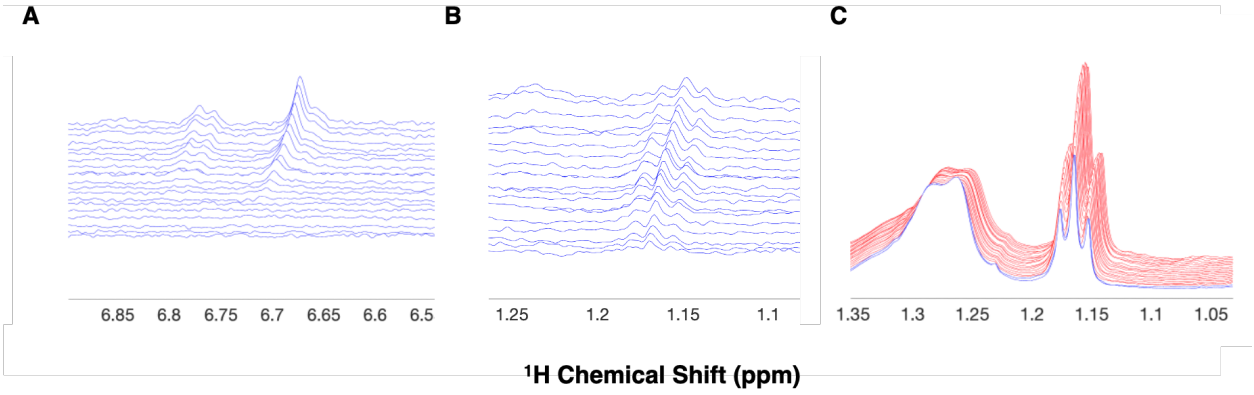

Figure 3.11. Flux from QA accumulates in HGA in Δ*qa-x*. A. Universally labeled ^{13}C-QA was fed to 6 mg Δ*qa-x*, resulting primarily in accumulation of characteristic HGA peaks (measured by hsqcetgpr1d). **B.** ^{13}C also accumulated in small amounts of ethanol consistent with natural abundance. **C.** ^{12}C Ethanol (noesypr1d) in the same culture accumulated in the characteristic high-density pattern, implying ethanol pools are fed by fluxes with sources other than QA.

Aromatic amino acids phenylalanine and tryptophan generally do not provide carbon for the TCA cycle, and carbon is lost as CO_2 during their biosynthesis. Rather, these serve as nitrogen sources in most eukaryotes (cyc.pnnl.gov). As such, carbon flux through chorismite and prephenate is effectively trapped if it is diverted to these pathways without phenylalanine hydroxylase, which is not present in some fungi, including *Neurospora*. Instead, the Ehrlich pathway is used to produce aromatic alcohols phenylethanol and tryptophol, which were not observed. On the other hand, tyrosine biosynthesis through 4-hydroxyphenylpyruvate is reversible. Thus, in the WT cultures, tyrosine may be utilized as a reserve for flux through the constitutive pathway.

The fact that loss of *qa-x* function results in homogentisate accumulation suggests that functional *qa-x* activates homogentisate 1,2-dioxygenase (NCU05499; cyc.pnnl.gov) in the WT. Fumarate (6.50 ppm), a downstream product of this degradation pathway, was observed at very low levels in the highest density cultures for both strains, as well as a dense *qa-4* culture. Acetoacetate, the other product, was not observed in any cultures. This could imply rapid utilization and/or low levels of synthesis.

Evidence that a quorum sensing mechanism drives the density-dependent shift

We next tested high-density conditioned Δ*qa-x* media against low-density Δ*qa-x* mycelia. We found that the mycelia metabolize as if they were a high-density culture, producing ethanol and maintaining choline and succinate levels for the first 5-6 h (Figure 3.12). At that point, the mycelia began metabolizing as if they were a low-density culture. This result indicates that there is likely a chemical signal in the conditioned media which can induce the high-density phenotype. Additionally, the return to low-density phenotype suggests that the molecule is either degraded or actively consumed by the mycelia. If the former is true, isolation of the molecule

may prove difficult. More work is needed to confirm this observation and isolate the molecule to identify it.

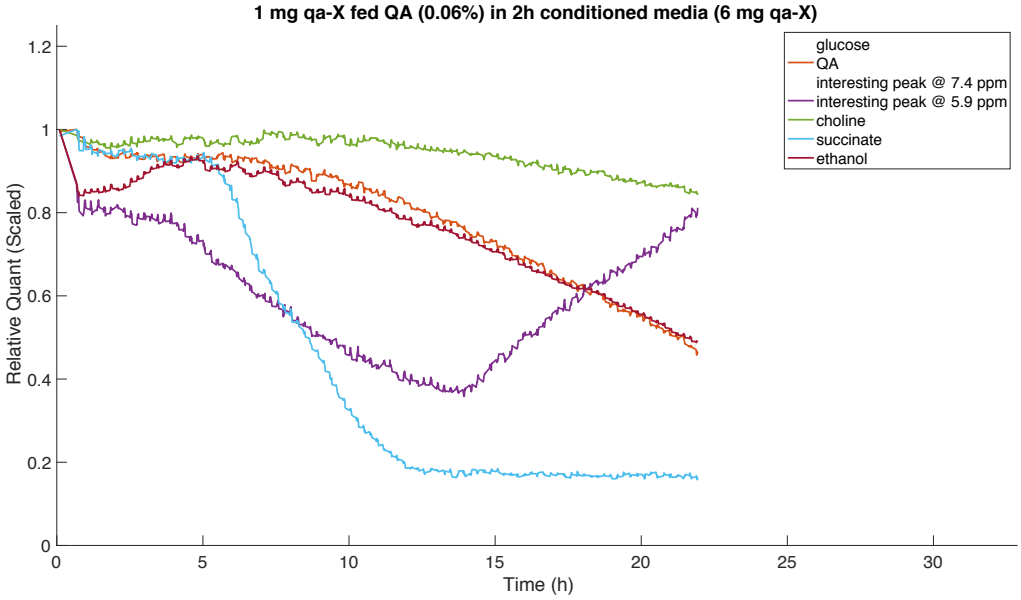

Figure 3.12. Media conditioned by dense cultures may trigger the high-density phenotype in low-density cultures. Media conditioned by two Δ*qa-x* runs initiated limited ethanol production from 1 mg of Δ*qa-x* mycelia. Choline, QA, succinate, and ethanol levels were sustained or increased slightly as would be expected in a high-density culture limited to low-density kinetics. There is a coordinated and marked change at 5 h to consumption of these metabolites, consistent with a reversion to low-density phenotype upon depletion of a compound in the conditioned media. Cells were removed by filtration from two separate 6-mg Δ*qa-x* CIVM runs after 2h. This timepoint was chosen because most metabolic trends are stable and aligned well with previous high-density Δ*qa-x* runs, but the media is still complete. Filtrates were combined and used as starting media for the low-density experimental run. Conditioning and experimental runs were carried out the same day. The observed effect may be more pronounced using freshly conditioned media due to QSS instability.

Quorum sensing is known to lead to metabolic/developmental shifts in both bacteria (homoserine lactones) (Studer et al. 2020) and fungi (farnesol and aromatic alcohols) (Nickerson et al. 2006; Weiland-Bräuer 2020; Hogan 2006). The aromatic alcohols tyrosol, phenylethanol, and tryptophol are of particular interest because they are derived from aromatic amino acids tyrosine, phenylalanine, and tryptophan, respectively. These amino acids are derived from QA via the constitutive anabolic (*arom*) shunt, while protocatechuic acid (PCA) is produced by the QA-induced catabolic pathway. Under QA feeding, catabolism is driven, but anabolism may still occur because of the need for aromatic amino acids. However, ethanol is a viable carbon source for N. crassa as well, as we have seen and as reported by Xie et al. (2004).

Cell density is monitored by an aromatic alcohol-based quorum sensing mechanism in yeast, unraveled by Chen and Fink (2006). The output of this system drives the decision to enter morphogenesis or stationary phase. High cell density triggers transcription factor Aro80p activation. Genes ARO9 and ARO10 are inhibited by in high nitrogen conditions. Nitrogen inhibition of aromatic amino acid degradation genes follows from these compounds being used as nitrogen sources. Under nitrogen starvation, these biosynthetic genes produce tryptophol and phenylethanol, which are derived from tryptophan and phenylalanine, respectively. At low cell densities (1E5 cells/mL), alcohols are produced, but quorum sensing is not activated. At higher cell densities (5E7 cells/mL), tryptophol accumulates and activates ARO9 and ARO10 through an Aro80p-dependent mechanism, forming a positive feedback loop. Tryptophol and phenylethanol both accumulate and stimulate morphogenesis to pseudohyphal growth through a PKA cascade involving Tpk2p and FLO11. Interestingly, tyrosol was previously identified as a quorum-sensing molecule in *Candida albicans* (Alem et al 2006), but did not stimulate this effect in yeast. Although we did not detect these aromatic alcohols, their presence is quite

possible. The physiological concentrations of phenylethanol and tyrosol (5-8 μM) and tryptophol (1-2 μM) measured in the yeast study (Chen and Fink 2006) fall below our limit of detection by untargeted CIVM-NMR. Homologs of the alcohol dehydrogenases in all three aromatic alcohol pathways are present in Neurospora. Accumulation of HGA in the mutant may be a sign of increased flux pressure in these upstream pathways that could explain the lower density threshold in the mutant. This effect must be localized in the pathway, however, as the WT accumulated significantly higher levels of tyrosine and phenylalanine than the mutant and a dense *qa-4* culture (Figure 3.13) did not accumulate homogentisate as might be expected by flux diversion to the anabolic pathway (Figure 3.10).

From a dynamical perspective, the *arom* genes comprising the anabolic pathway in *Neurospora* are constitutive; i.e., the anabolic pathway might be expected to produce amounts of aromatic amino acids proportional to the number of cells present. This would be a convenient source of flux for a QSS in the WT, and a bottleneck downstream in Δ*qa-x* could lead to overflow into the aromatic alcohols. Interestingly, the density-dependent shift in metabolism has only been observed with QA and residual ethanol as a carbon source. Since phenylalanine and tyrosine accumulate in all the experiments, it is reasonable to conclude that the constitutive branch is receiving flux. In the mutant, the flux excess accumulates in HGA.

Our first and only attempt to induce a high density phenotype in a low-density Δ*qa-x* culture using addition of QA + 3x physiological concentrations of phenylethanol, tyrosol, and tryptophol was not successful (data not shown). These concentrations may not be relevant in *Neurospora,* or the molecules could have counteractivity, or they may not be the correct molecules. It may be that Δ*qa-x* sensitivity to density arises from a block to the anabolic

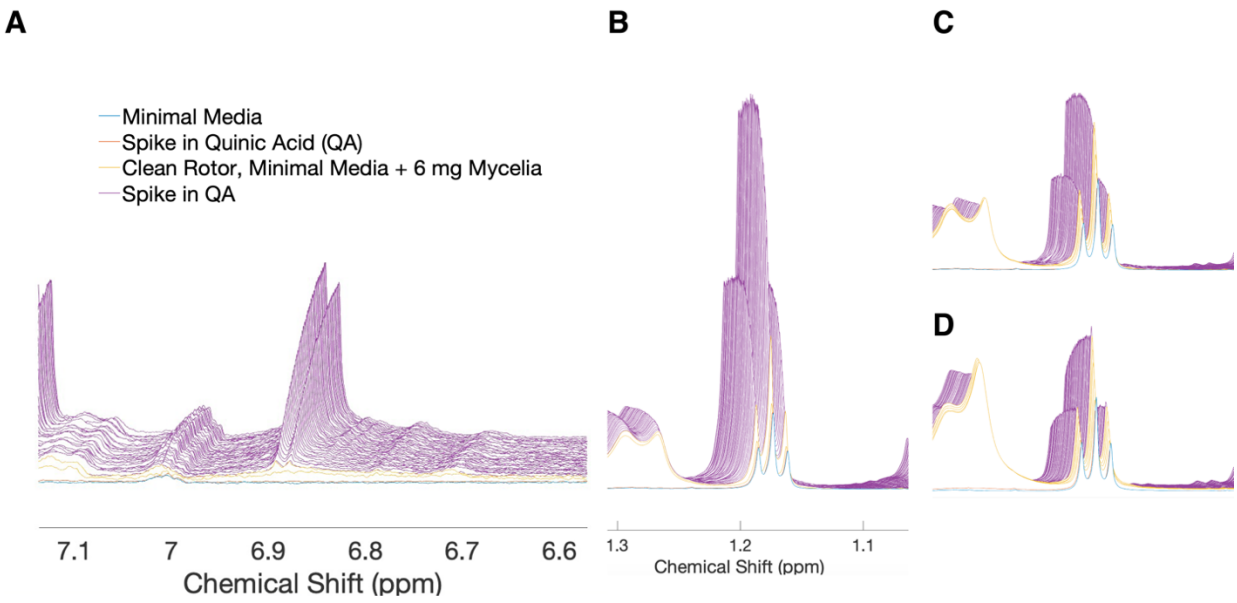

Figure 3.13. A dense *qa-4* mutant culture does not accumulate homogentisic acid, but produces high amounts of ethanol. (A) No HGA was detected in a 6 mg *qa-4* mutant culture fed 0.5% QA (w/v), although tyrosine (6.9 ppm) accumulated greatly. (B) Even without appreciable QA consumption, the same *qa-4* mutant culture produced enormous quantities of ethanol (shown, 1.17 ppm) and other compounds including succinate, free amino acids, formate, tyrosine, choline, the associated singlet at 3.2 ppm (not shown). Ethanol, succinate, choline, and the singlet slowed or ceased accumulating upon G-1-P and putative ribose depletion (not shown). (C) Ethanol production in a 6 mg *qa-x* mutant culture fed 3% QA (w/v). (D) Ethanol consumption in a WT culture fed 3% QA (w/v). Note that (B), (C), and (D) are scaled identically as evidenced by the starting level of ethanol. Legend in (A) is common to all panels.

degradation pathway, channeling flux to PCA and β-ketoadipate pathway, which is known to produce allorecognition molecules in bacteria (Harwood and Parales 1996). Given that the *qa-4* mutant blocks flux to the β-ketoadipate cycle but still exhibits a high-density phenotype (Figure 3.13), however, it seems unlikely that a QS could be produced downstream of DHS. Likewise,

given that Δ*qa-x* accumulates HGA and is more sensitive to density, it seems unlikely that a QS could accumulate downstream of 4-hydroxyphenylpyruvate. Therefore, the most likely source of a QS would seem to be the internal inducers, DHS, DHQ, or QA itself. However, higher concentrations of QA are not sufficient to increase sensitivity to cell density in the WT, as the low-density phenotype presents in the WT culture with a higher amount of QA.

Discussion

We have provided here a distinct dynamic metabolic phenotype for the Δ*qa-x* mutant under starvation, QA feeding, and glucose-QA-starvation shifts. In each of these the mutant is distinguishable from the WT. Differences are consistent with a role of *qa-x* in CCR, and indicate that flux in the anabolic QA pathway is blocked at HGA in the mutant, which explains the classic media coloration phenotype for this strain. We then find that Δ*qa-x* is more sensitive to cell density, with a lowered threshold for a novel quorum sensing behavior in *Neurospora crassa* involving reversal of net ethanol and choline fluxes. These results have not determined the function of the *qa-x* gene, but indicate that it may be involved in choline metabolism and the anabolic leg of the QA pathway.

It seems unlikely that *Neurospora* would grow to densities as high as those used in this study. However, the density shift observed here does occur near the top of the physiological range. An ability to sense a quorum is useful for several reasons, including self- and allo-competition. On the other hand, the utility of a metabolic shift in a quorum environment, particularly when ethanol is produced under those conditions, may be to inhibit the growth of competing microbes (Gause 1932; Goudriaan and De Wit 1973). However, this would imply an ability to detect those microbes, and not *Neurospora* per se. An interesting dynamic may arise if this communication occurs in tandem with the well-described mating type and vegetative hyphal

fusion communication systems in *Neurospora* (Herzog et al. 2015; Jonkers et al. 2016). Future experiments will focus on ^{13}C labeled feeding experiments to track specific fluxes of QA and ethanol, as well as additional attempts at inducing the high-density phenotype with known bacterial and fungal signaling molecules. Identification and characterization of this quorum sensing process will be important for *Neurospora* research given the popularity of liquid cultures. Additionally, both quorum sensing and ethanol production, particularly the overproduction phenotype of the *qa-4* mutant (Figure 3.13), may be of interest to the biotechnology community, and will be explored further in future work.

Materials and Methods

Conidial suspensions

Stock strain conidia were kept at -80C and were either obtained from Mary Case (OR74A Wild-type; WT), David Asch (*qa-x* mutant; Δ*qa-x*), or the FGSC. For each strain, an agar slant (1.5% Sucrose Vogels, Arom complete) was inoculated with conidia without thawing and placed at 30°C in a dark incubator for 3-5 days to allow for full growth of hyphae and conidiophores. The slants were then placed under light for 24h to encourage maturation of conidia. The slants were washed with 12 mL of sterile H2O, which was filtered through cotton. Each suspension was adjusted to 10E6 cells/mL, then stored for up to 3 weeks at 4°C (we have noticed that metabolism is altered after ~ 4 weeks at °C in some strains, but have found conidial suspensions up to 3 weeks reliable).

Neurospora crassa cultures for color change optimization

Vogels containing QA (3 %, w/v) was prepared, pH adjusted using concentrated NaOH to pH 4.5, and 4-fold serially diluted into Vogels media (no carbon) to yield 156, 39, 10, 2.4, 0.6, 0.15, 0.04, and 0.01 mM QA (Sigma Aldrich, St. Louis, MO, USA) solutions. These were

aliquoted into 1 mL volumes in a 2-mL deep-well culture plate. To each well, 20 µL of conidial suspension (Δ*qa-x* or WT) were added, and the plate was covered with rayon filter tape. The plate was incubated at 30°C for 7 days until a visible mycelium had grown and covered the air-liquid interfaces of the wells with conidia. The plate was removed to the bench for 5 weeks, during which color in the *qa-x* wells deepened to a dark brown.

Growth of Neurospora crassa for CIVM-NMR

Vogel's media (50 mL, 1.5% sucrose w/v) in a 250-mL Erlenmeyer flask was inoculated under aseptic conditions with conidial suspension to a total concentration of 1E5 cells/mL (200 µL conidial suspension), and covered with aluminum foil. Liquid cultures were grown with orbital shaking (~237 rpm) at room temperature (~25°C) under constant cool white light (7 µmol L−1 s−1 m−2) for 32 h. At that point mycelia consistently formed a single, cohesive mass. The entire culture was transferred to a 50 mL conical tube (Sarstedt; Newton, NC, USA) for transport to the NMR facility (15–30 min).

Preparation of Neurospora mycelia for CIVM-NMR

Neurospora mycelia were prepared for CIVM as described in Judge et al. (2019), with the following modifications: 1.5% Sucrose Arom Complete Media was used. Mycelia were grown for 24-37h at room temperature, or 30°C for 20-24h. Light was not controlled.

CIVM-NMR Experiments

A basic CIVM protocol template for *N. crassa* will be made available at protocols.io., and example can be found in Appendix A1. All CIVM experiments were carried out as outlined in Judge et al. (2019) with the following modifications: Vogels Minimal Media for NMR (VMM-NMR) was made up as 100 mL of 10x concentrate, leaving out sodium citrate. All solutions (wash solution, addition solutions) containing VMM-NMR in this manuscript were

made using dilutions of this concentrate. For QA solutions, a 15% w/v QA addition solution (pH-adjusted to 4.5) was prepared diluted in VMM-NMR to 10x the target in-rotor concentration (either 3% or 0.3% w/v). Gradient experiments used 0.3% QA in the rotor (1:5 dilution of the 15% solution), which was added as a 5µL (1:10) partial media replacement (remove 5 µL of 50 µL current rotor media, then replace with addition solution so that the concentrations of media components other than the carbon source are unaffected). All experiments presented in this study were measured at 3500 Hz spinning speed in order to impart less stress on the organism. Interleaved noesypr1d (as described in Judge et al., 2019 with the modification of no dummy scans and only 8 scans to achieve 34 s experiments) and jres spectra were collected. Jres experiments (not reported) each lasted 7 minutes and 40 seconds. Every 10 noesypr1d were interleaved with 1 jres, and this sequence was repeated for 12-30 h depending on the run. For starve conditions, mycelia were run in VMM-NMR for 1h. For QA addition/spiking conditions, 5 µL of culture media was removed from the rotor, 5 µL of addition solution was added, and the data collection was restarted within 8 minutes. Note: for *qa-4* mutant experiment: QA addition solution was diluted to 0.3% instead of running at 3% QA. For glucose + QA runs, 0.3% QA and 9.25 mM glucose were used. For ^{13}C-QA spiking, 0.3% U-^{13}C-QA (Isolife, Wageningen UR, The Netherlands) was used, and data were collected according to ^{13}C-glucose experiments in Judge et al. (2019) with the exception of using 0 dummy scans + 8 scans for noesypr1d experiments, and 16 scans for hsqcetgpr1d experiments. After runs, liquid was pipetted off from mycelia and filtered. Of 50 µL of culture, ~30 µL of liquid was typically recovered. Mycelia were washed with 4 quick sequential rinses in an eppi tube with 500 mL of ddH2O, removing 450 µL each time so that mycelia were left in 200 µL H2O, which was then flash-frozen in liquid nitrogen and lyophilized.

Data Processing and Management

All Bruker data files for each sample (containing multiple experiments) were zipped into a single file, uploaded to a secure Dropbox account, and unzipped for processing on a common location on a Mac PC. Data were phased and pre-processed using the publicly available CIVM NMR pipe wrapper toolbox (https://github.com/artedison/Edison_Lab_Shared_Metabolomics_UGA)

Quantification and Annotation of NMR features

Custom MATLAB (R2021a; The MathWorks, Inc., Natick, Massachusetts, USA) scripts were used. Maximum spectral intensity in a region defined for each metabolite presented in this study was taken for each timepoint (spectrum). For scaled plots, data were. Custom MATLAB scripts were written for plotting. Dependencies from the Edison Lab Metabolomics Toolbox (https://github.com/artedison/Edison_Lab_Shared_Metabolomics_UGA) were used in the scripts. Chenomix (Chenomix, Inc., Edmonton, Canada) in trial mode was used for annotation of HGA. Other metabolites were annotated based on previous *Neurospora* CIVM-NMR extract sample annotations (Judge et al. 2019).

References

Alem, M. A. S., Oteef, M. D. Y., Flowers, T. H. & Douglas, L. J. Production of tyrosol by Candida albicans biofilms and its role in quorum sensing and biofilm development. *Eukaryot Cell* **5**, 1770-1779, doi:10.1128/EC.00219-06 (2006).

Arnett, D. R., Lorimer, H. E. & Asch, D. K. Catabolite repression directly affects transcription of the *qa-y* gene of Neurospora crassa. *Fungal genetics and biology : FG & B* **46**, 377-380, doi:10.1016/j.fgb.2009.02.003 (2009).

Battogtokh, D., Asch, D. K., Case, M. E., Arnold, J. & Schüttler, H.-B. An ensemble method for identifying regulatory circuits with special reference to the qa gene cluster of *Neurospora crassa*. *Proceedings of the National Academy of Sciences* **99**, 16904-16909 (2002).

Beadle, G. & Tatum, E. Neurospora. II. Methods of producing and detecting mutations concerned with nutritional requirements. *American Journal of Botany* **32**, 678-686 (1945).

Beadle, G. W. & Tatum, E. L. Genetic Control of Biochemical Reactions in Neurospora. *Proceedings of the National Academy of Sciences* **27**, 499, doi:10.1073/pnas.27.11.499 (1941).

Case, M. E., Geever, R. F. & Asch, D. K. Use of gene replacement transformation to elucidate gene function in the qa gene cluster of Neurospora crassa. *Genetics* **130**, 729-736 (1992).

Chaleff, R. S. The Inducible Quinate-Shikimate Catabolic Pathway in Neurospora crassa: Genetic Organization. *Microbiology* **81**, 337-355, doi:https://doi.org/10.1099/00221287-81-2-337 (1974).

Chen, H. & Fink, G. R. Feedback control of morphogenesis in fungi by aromatic alcohols. *Genes Dev* **20**, 1150-1161, doi:10.1101/gad.1411806 (2006).

Davis, R. H. & de Serres, F. J. in *Methods in Enzymology* Vol. 17 79-143 (Academic Press, 1970).

de Assis Leandro, J. *et al.* Carbon Catabolite Repression in Filamentous Fungi Is Regulated by Phosphorylation of the Transcription Factor CreA. *mBio* **12**, e03146-03120, doi:10.1128/mBio.03146-20.

Fillinger, S., Panozzo, C., Mathieu, M. & Felenbok, B. The basal level of transcription of the alc genes in the ethanol regulon in Aspergillus nidulans is controlled both by the specific transactivator AlcR and the general carbon catabolite repressor CreA. *FEBS letters* **368**, 547-550 (1995).

Gaertner, F. H. & Cole, K. W. A cluster-gene: Evidence for one gene, one polypeptide, five enzymes. *Biochemical and Biophysical Research Communications* **75**, 259-264, doi:https://doi.org/10.1016/0006-291X(77)91037-3 (1977).

Gause, G. F. Experimental Studies on the Struggle for Existence : I. Mixed Population of Two Species of Yeast. *Journal of Experimental Biology* **9**, 389-402, doi:10.1242/jeb.9.4.389 (1932).

Giles, N. *et al.* Gene organization and regulation in the qa (quinic acid) gene cluster of Neurospora crassa. *Microbiological reviews* **49**, 338-358 (1985).

Giles, N., Geever, R., Asch, D., Avalos, J. & Case, M. Organization and regulation of the qa (quinic acid) genes in Neurospora crassa and other fungi. *Journal of Heredity* **82**, 1-7 (1991).

Giles, N. H., Case, M. E., Partridge, C. W. & Ahmed, S. I. A gene cluster in Nuerospora crassa coding for an aggregate of five aromatic synthetic enzymes. *Proceedings of the National Academy of Sciences* **58**, 1453, doi:10.1073/pnas.58.4.1453 (1967).

Goudriaan, J. & De Wit, C. T. A Re-Interpretation of Gause's Population Experiments by Means of Simulation. *Journal of Animal Ecology* **42**, 521-530, doi:10.2307/3121 (1973).

Gross, S. R. & Fein, A. LINKAGE AND FUNCTION IN NEUROSPORA. *Genetics* **45**, 885 (1960).

Harwood, C. S. & Parales, R. E. The beta-ketoadipate pathway and the biology of self-identity. *Annual review of microbiology* **50**, 553-590, doi:10.1146/annurev.micro.50.1.553 (1996).

Herzog, S., Schumann, M. R. & Fleißner, A. Cell fusion in Neurospora crassa. *Current opinion in microbiology* **28**, 53-59, doi:10.1016/j.mib.2015.08.002 (2015).

Hogan, D. A. Quorum Sensing: Alcohols in a Social Situation. *Current Biology* **16**, R457-R458, doi:https://doi.org/10.1016/j.cub.2006.05.035 (2006).

Howe, K. L. *et al.* Ensembl Genomes 2020—enabling non-vertebrate genomic research. *Nucleic Acids Research* **48**, D689-D695, doi:10.1093/nar/gkz890 (2020).

Huiet, L. & Giles, N. H. The qa repressor gene of Neurospora crassa: wild-type and mutant nucleotide sequences. *Proceedings of the National Academy of Sciences* **83**, 3381, doi:10.1073/pnas.83.10.3381 (1986).

Hynes, M. J., Murray, S. L., Duncan, A., Khew, G. S. & Davis, M. A. Regulatory genes controlling fatty acid catabolism and peroxisomal functions in the filamentous fungus Aspergillus nidulans. *Eukaryot Cell* **5**, 794-805 (2006).

Jonkers, W., Fischer, M. S., Do, H. P., Starr, T. L. & Glass, N. L. Chemotropism and Cell Fusion in Neurospora crassa Relies on the Formation of Distinct Protein Complexes by HAM-5 and a Novel Protein HAM-14. *Genetics* **203**, 319-334, doi:10.1534/genetics.115.185348 (2016).

Judge, M. T. *et al.* Continuous in vivo Metabolism by NMR. *Frontiers in Molecular Biosciences* **6**, doi:10.3389/fmolb.2019.00026 (2019).

Kochut, K. *et al.* IntelliGEN: A distributed workflow system for discovering protein-protein interactions. *Distributed and Parallel Databases* **13**, 43-72 (2003).

Logan, D. A. *et al.* Genome-wide expression analysis of genetic networks in Neurospora crassa. *Bioinformation* **1**, 390 (2007).

Lumsden, J. & Coggins, J. R. The subunit structure of the arom multienzyme complex of Neurospora crassa. A possible pentafunctional polypeptide chain. *The Biochemical journal* **161**, 599-607, doi:10.1042/bj1610599 (1977).

Nickerson, K. W., Atkin, A. L. & Hornby, J. M. Quorum Sensing in Dimorphic Fungi: Farnesol and Beyond. *Applied and Environmental Microbiology* **72**, 3805-3813, doi:doi:10.1128/AEM.02765-05 (2006).

Patel, V. B., Schweizer, M., Dykstra, C. C., Kushner, S. R. & Giles, N. H. Genetic organization and transcriptional regulation in the qa gene cluster of Neurospora crassa. *Proceedings of the National Academy of Sciences* **78**, 5783-5787 (1981).

Pfister, N., Bauer, S. & Peters, J. Learning stable and predictive structures in kinetic systems. *Proceedings of the National Academy of Sciences* **116**, 25405-25411 (2019).

Rines, H. W., Case, M. E. & Giles, N. H. Mutants in the arom gene cluster of Neurospora crassa specific for biosynthetic dehydroquinase. *Genetics* **61**, 789-800, doi:10.1093/genetics/61.4.789 (1969).

Schweizer, M., Case, M. E., Dykstra, C. C., Giles, N. H. & Kushner, S. R. Identification and characterization of recombinant plasmids carrying the complete qa gene cluster from Neurospora crassa including the qa-1+ regulatory gene. *Proceedings of the National Academy of Sciences* **78**, 5086-5090 (1981).

Studer, S., Mandel, M. J. & Ruby, E. G. AinS Quorum Sensing Regulates the Vibrio fischeri Acetate Switch. *Journal of Bacteriology* **190**, 5915 - 5923 (2008).

Sun, J. & Glass, N. L. Identification of the CRE-1 cellulolytic regulon in Neurospora crassa. *PLoS One* **6**, e25654, doi:10.1371/journal.pone.0025654 (2011).

Tang, X. *et al.* Systems Biology of the qa Gene Cluster in Neurospora crassa. *PLOS ONE* **6**, e20671, doi:10.1371/journal.pone.0020671 (2011).

Tatum, E. L., Gross, S. R., Ehrensvärd, G. & Garnjobst, L. SYNTHESIS OF AROMATIC COMPOUNDS BY NEUROSPORA. *Proceedings of the National Academy of Sciences* **40**, 271, doi:10.1073/pnas.40.5.271 (1954).

Weiland-Bräuer, N. Friends or Foes—Microbial Interactions in Nature. *Biology* **10**, 496 (2021).

Xie, X. *et al.* Transcriptional response to glucose starvation and functional analysis of a glucose transporter of Neurospora crassa. *Fungal genetics and biology* **41**, 1104-1119 (2004).

CHAPTER 4

DISCUSSION AND FUTURE DIRECTIONS

CIVM-NMR is important for unraveling quorum sensing in *Neurospora*

CIVM-NMR provides many new avenues for research in microbial metabolism and systems biology. Direct real-time measurements of major metabolite pools yields information about pathway fluxes (Judge et al. 2019). In Chapter 3, I build on many of the ideas outlined in Chapter 2. In the initial paper, we note that samples can be used in downstream *in vivo* or chemical analyses following CIVM. In Chapter 3, I demonstrate this by re-running the organism, *i.e*. I show it is robust to our experimental conditions. This experiment also introduces the partial media replacement approach and provides both a perturbation (e.g. addition of carbon source or multiple carbon sources, specific inhibitors (Drsata et al. 1996; Ralser et al. 2008), quorum sensing molecules (Nickerson et al. 2006; Weiland-Bräuer 2020; Hogan 2006), pheremones, or other modulators of cell behaviors such redox metabolites or toxins) as well as a controlled way to take stock of intracellular and extracellular metabolites. Furthermore, I report drastically increased resolution is possible (from 4 min to ~35 s), which allows more flexible signal averaging across timepoints and opens the method to observation of minute-scale dynamics. Further development will come in the analysis of tracked ridges in CIVM data. Wu et al. 2021 (in review) propose a workflow that facilitates characterization of these dynamic and multivariate datasets using functional PCA (fPCA). In this workflow, we fit functional forms to tracked ridges, then apply PCA to derive eigenfunctions for a given sample and plot ridges as single points in this principal component space. Preliminary application of this method to my

density gradient data revealed clear differences in both clustering of ridges in PCA space, as well as in the eigenfunctions for low and high density samples.

Future directions for quorum sensing and the *qa* cluster in *Neurospora*

As discussed in Chapter 1, full utilization of the time series data from CIVM-NMR will require a modeling-based method. In these chapters, I primarily make inferences about metabolites based on the coincidence of shifts in their profiles. For instance, the depletion of glucose occurs at the same time ethanol accumulation halts (Chapter 2; Judge et al. 2019), implying these fluxes are related. Likewise, the depletion of QA in glucose+QA feeding experiments in Chapter 3 is associated with an uptick in ethanol consumption. This direction is also extended in Wu et al. in the form of data-driven kinetic networks which associate ridges (time-series metabolite pool dynamics) based on these inherent time-dependences using CausalKinetix (Pfister et al. 2019). The result is an empirical network of hypothetical fluxes between metabolite features, regardless of whether or not they are annotated/identified. Efforts are ongoing to integrate/map these networks with known biochemical networks, such as those in MetaCyc (metacyc.org).

The clear next biological direction for this work is to probe other mutants in the *qa* cluster for subtle phenotypes using these approaches. The study of this classic biochemical pathway built upon auxotrophic relationships has produced a better understanding (Giles et al. 1985) of its regulatory relationships than those, perhaps, of any other pathway in *Neurospora*. This makes the pathway all the more enticing for the application of a simple untargeted metabolomics approach (Edison et al. 2021) such as the one we have demonstrated here. Additionally, a solid foundation has been laid by transcriptomics studies (Battogtokh et al. 2002, Tang et al. 2011) for a fuller elucidation of the metabolic reaches of *qa* cluster metabolism and

carbon catabolite repression in this fungus. Furthermore, in a mutant with only a subtle phenotype, we were quickly able to establish stark differences in metabolite dynamics, such as the accumulation of HGA in Δ*qa-x*, that went unnoticed for decades despite being one of the inspirations for Beadle and Tatum's seminal experiments in genetic biochemistry. This ties the gene's function strongly back to QA metabolism, as well as other modules such as aromatic amino acid catabolism and ethanol, G-1-P, and choline utilization. Furthermore, it appears that *qa-x* has an effect on a previously unobserved switch in metabolism induced by high cell density, the characterization of which presents another promising avenue for research. Coincidentally, the discovery of a quorum sensing mechanism in *Neurospora* may have important implications for circadian clock synchronization, another rapidly evolving interest in the Arnold lab.

REFERENCES

Arnett, D. R., Lorimer, H. E. & Asch, D. K. Catabolite repression directly affects transcription of the *qa-y* gene of Neurospora crassa. *Fungal genetics and biology : FG & B* **46**, 377-380, doi:10.1016/j.fgb.2009.02.003 (2009).

Battogtokh, D., Asch, D. K., Case, M. E., Arnold, J. & Schüttler, H.-B. An ensemble method for identifying regulatory circuits with special reference to the qa gene cluster of Neurospora crassa. *Proceedings of the National Academy of Sciences* **99**, 16904-16909 (2002).

Edison, A. S. *et al.* NMR: Unique Strengths That Enhance Modern Metabolomics Research. *Analytical Chemistry* **93**, 478-499, doi:10.1021/acs.analchem.0c04414 (2021).

Giles, N. *et al.* Gene organization and regulation in the qa (quinic acid) gene cluster of Neurospora crassa. *Microbiological reviews* **49**, 338-358 (1985).

Hogan, D. A. Quorum Sensing: Alcohols in a Social Situation. *Current Biology* **16**, R457-R458, doi:https://doi.org/10.1016/j.cub.2006.05.035 (2006).

Judge, M. T. *et al.* Continuous in vivo Metabolism by NMR. *Frontiers in Molecular Biosciences* **6**, doi:10.3389/fmolb.2019.00026 (2019).

Nickerson, K. W., Atkin, A. L. & Hornby, J. M. Quorum sensing in dimorphic fungi: farnesol and beyond. *Applied and environmental microbiology* **72**, 3805-3813 (2006).

Pfister, N., Bauer, S. & Peters, J. Learning stable and predictive structures in kinetic systems. *Proceedings of the National Academy of Sciences* **116**, 25405-25411 (2019).

Tang, X. *et al.* Systems Biology of the qa Gene Cluster in Neurospora crassa. *PLOS ONE* **6**, e20671, doi:10.1371/journal.pone.0020671 (2011).

SUPPLEMENTAL MATERIAL CHAPTER 2

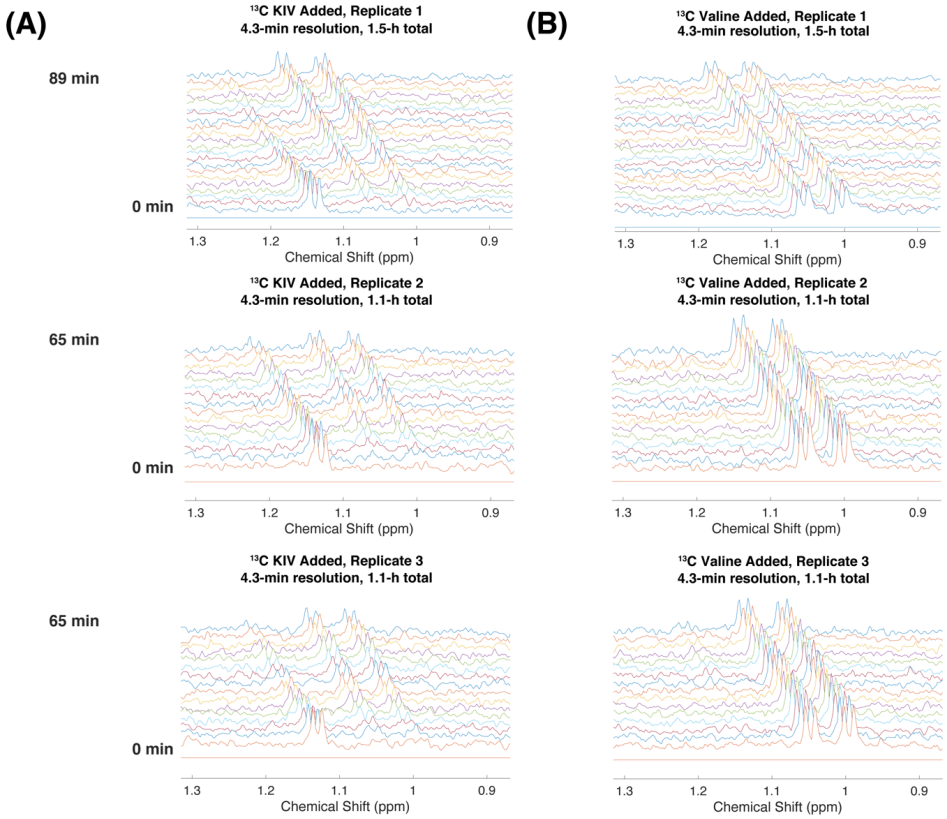

Supplementary Figure 1. Targeted isotopic CIVM-NMR measurements of metabolic flux in human myeloid leukemia cells are reproducible. (A) 1D ^{13}C-edited hsqc experiments were used to observe protons covalently attached to ^{13}C derived from uniformly labeled KIV in three independent replicates. ^{13}C valine accumulates as KIV is consumed. (B) The same experiments were used to observe protons covalently attached to ^{13}C derived from uniformly labeled valine in three independent replicates. ^{13}C derived from uniformly labeled valine does not accumulate to appreciable levels in KIV.

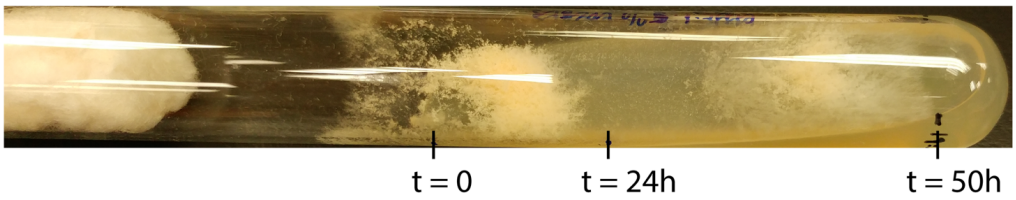

Supplementary Figure 2. Growth of *N. crassa* after a CIVM-NMR experiment. A piece of mycelium was used to inoculate a growth slant at t = 0. The culture was kept on the bench and the advancement of the growth front was marked at t = 0 h, 24 h and 50 h. Roughly circadian conidiation was observed between 0 h and 24 h, and again before the 50-h mark.

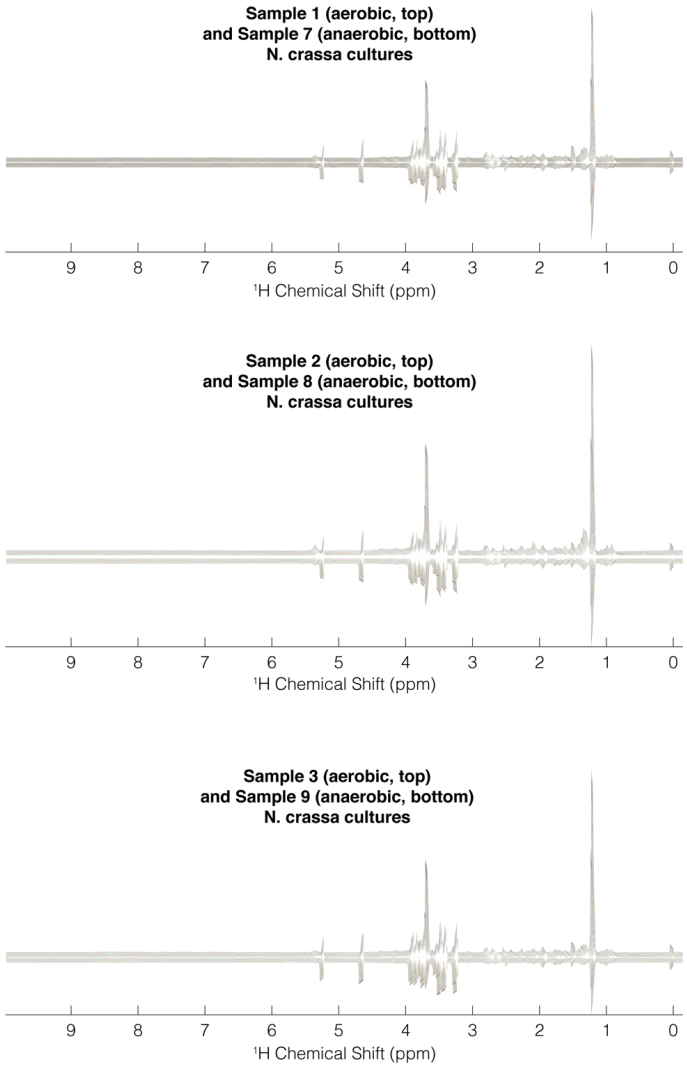

Supplementary Figure 3. Comparison of aerobic and anaerobic samples for three independent replicates. Replicates 1,2,3 (aerobic) are plotted against mirror images of replicates 7,8,9 (anaerobic).

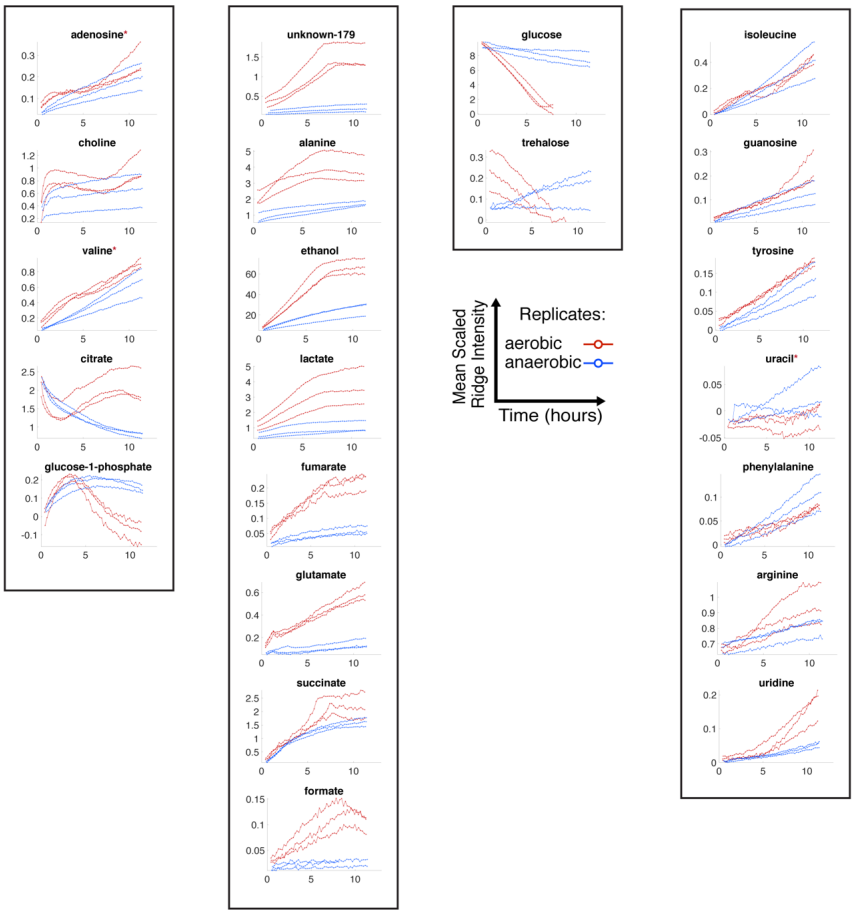

Supplementary Figure 4. Aerobic and anaerobic trajectories for each metabolite that was both annotated and quantified in this study. One example of an un-annotated ridge is also shown. Metabolites are grouped with those having similar profiles in one or both conditions. Red asterisks indicate compounds whose absolute peak intensities were affected by changes in baseline; these were therefore excluded from biological interpretation.

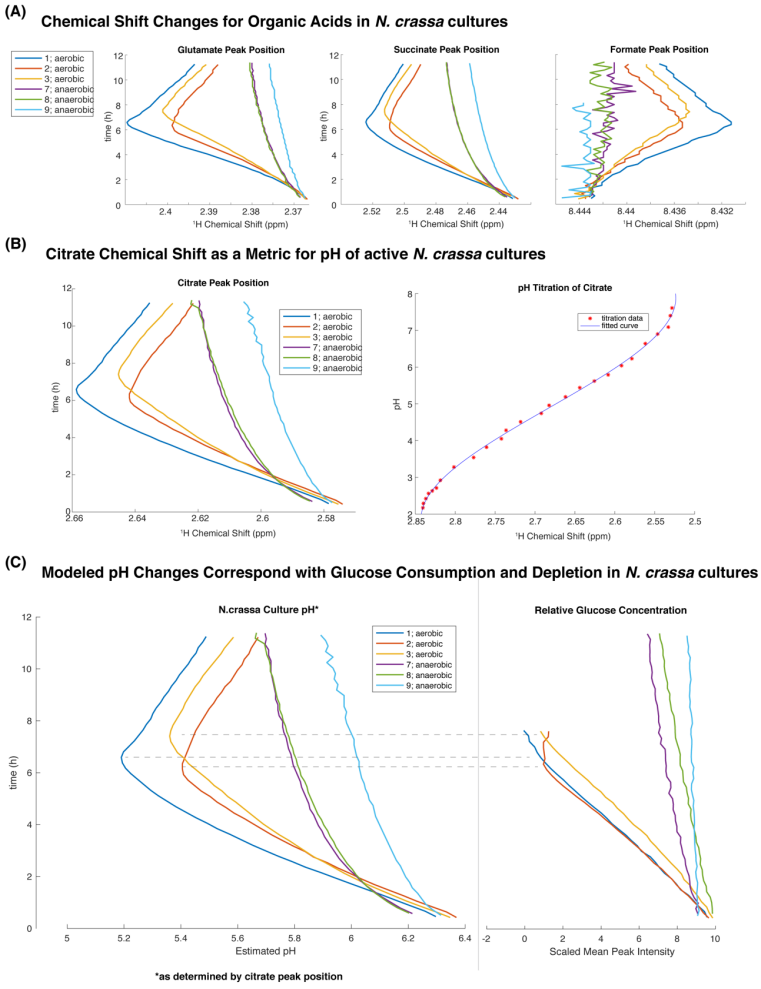

Supplementary Figure 5. Organic acid peak positions reflect glucose-dependent changes in pH over time. (A) Representative in-vivo peak position changes for glutamate, succinate, and formate for all samples. The formate peak position in the anaerobic samples is noisy because the peak was very low intensity. (B) Position of a representative citrate peak over time and in-house pH titration data for citrate. A 3rd-order polynomial was fit to the titration data in order to interpolate pH values at each timepoint for each sample (C). Dashed horizontal lines are used to show that glucose depletion coincided with reversal of acidification around 6-7 h in the aerobic samples.

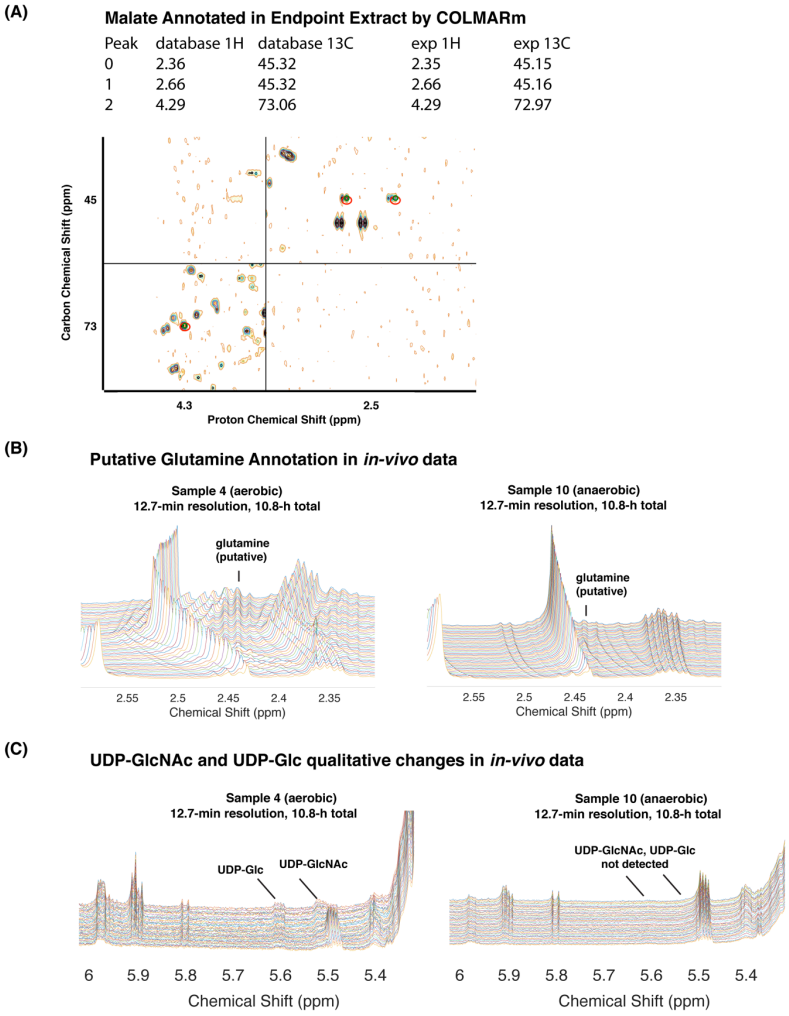

Supplementary Figure 6. Qualitative assessment for unquantifiable metabolites in this study. (A) Malate was annotated in the 2D data for endpoint extracts by peak matching to databases using COLMARm[1]. Positions of matched peaks are indicated with a red ellipse and in the peak table. (B) Peaks consistent with glutamine increased in the aerobic and may be present in the anaerobic condition. (C) UDP-GlcNAc (UDP-N-Acetyl Glucosamine; UDP-NAG) and UDP-Glc (UDPGlucose) were annotated in the aerobic condition but could not be traced reliably.

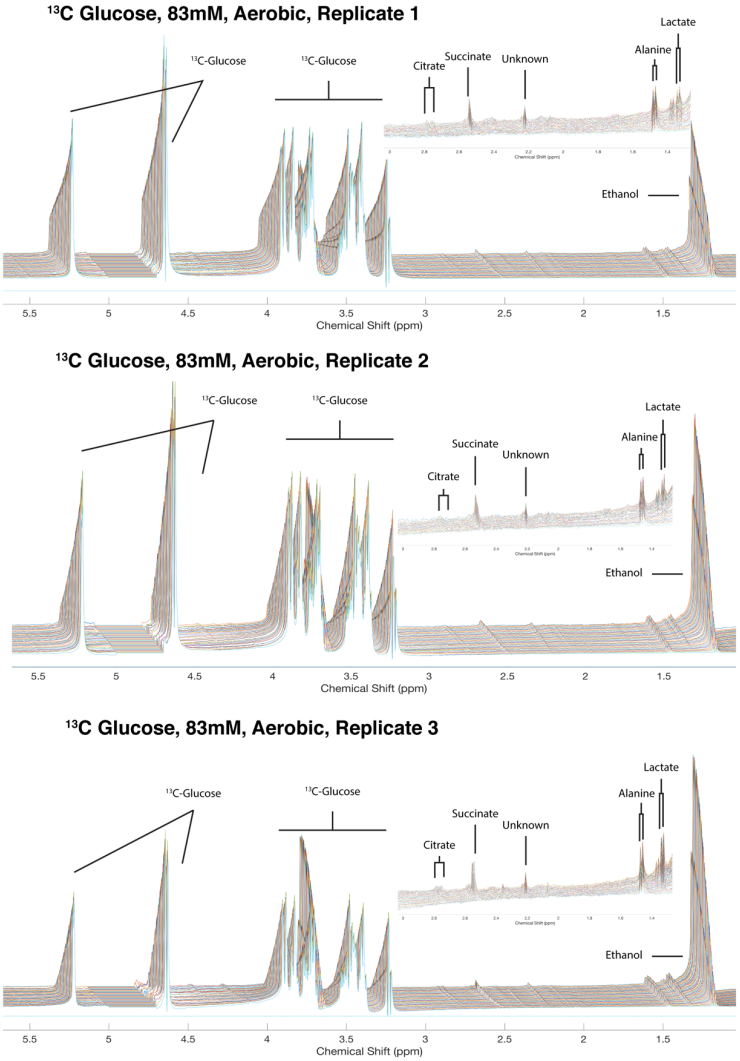

Supplementary Figure 7. Accumulation of ^{13}C-labeled metabolites in three independent replicate aerobic N. crassa cultures. hmqc1d NMR experiments were used to monitor the accumulation of ^{13}Clabeled metabolites after addition of uniformly labeled ^{13}C glucose. Glucose was converted to ethanol, alanine, succinate, and lactate, citrate, and some peaks that have yet to be identified.

(A)

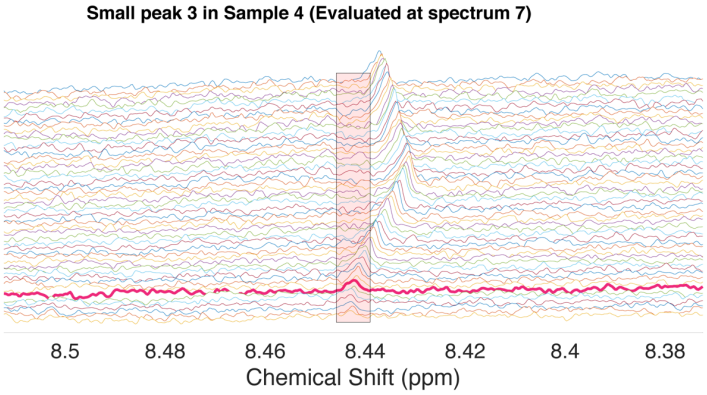

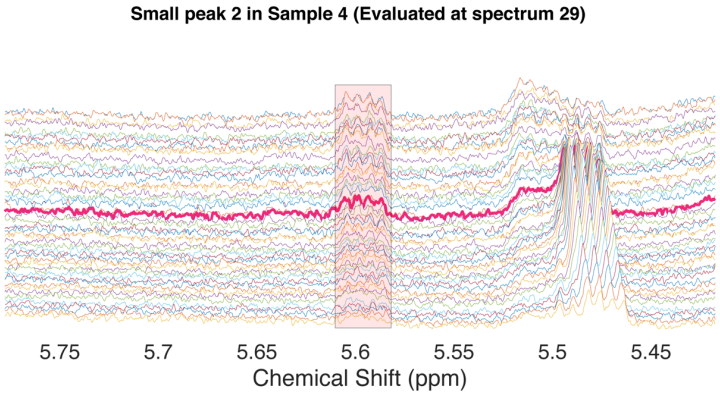

(B)

(C)

	Small Peak	Annotation	Integral (Peak)	Integral (DSS)	[1H] (mM)*
Individual Spectra	1	unknown	00.212	0047.526	0.036
	2	UDP-NAG (whole multiplet)	01.474	0048.040	0.246
	2	UDP-NAG (quarter multiplet)	-	-	0.062
	3	formate	00.145	0048.350	0.024
Summed Spectra	1	unknown	20.910	2466.623	0.068
	2	UDP-NAG	69.245	2466.623	0.225

* [1H] (mM) = (Peak Integral) / (DSS Peak Integral) * (0.89 mM * 9 DSS protons)

Supplementary Figure 8. Estimation of sensitivity for CIVM-NMR using our HR-MAS probe in an aerobic sample. (A) Formate peak in spectrum 7 (bolded in magenta, t = 84.6 min), where it became discernable from noise. (B) Similar result for a UDP-N-acetyl glucosamine peak in spectrum 29 (t = 363.8 min). (C) Table of measured intensities and calculated concentrations of ^{1}H based on the known concentration of DSS in the sample. Integrals were assessed using the boundaries shown by the pink box. Notably, formate and an unknown peak) of similar intensity (not shown) yielded similar concentrations of ^{1}H, and these values are within a factor of ~2 from the calculated potential sensitivity from one quarter of the UDP-N-acetylglucosamine peak.

ID[a]	Name[b]	Matching Ratio[c]	13C RMSD[d]	1H RMSD[e]	Uniqueness[f]	Manual Score[g]	Confidence Score[h]	Identified in 1D?[i]
1	D_Mannitol_1	1	0.05	0.007	2/4	Good	4	y
2	N_Acetyl_L_Glutamine_1	0.6	0.14	0.014	1/3	Poor	-	n
3	gamma_Aminobutyric_acid_1	0.67	0.18	0.009	1/2	Unknown	-	n
4	Phosphoethanolamine_1	1	0.05	0.003	1/2	Unknown	-	n
5	6_Aminohexanoic_acid_1	0.6	0.18	0.01	3/3	Poor	-	n
6	L_Arabitol_1	0.6	0.11	0.008	0/3	Unknown	-	n
7	D_Aspartate_1	1	0.03	0.004	3/3	Fair	4	n
8	Acetyl_phosphate_1	1	0.07	0.027	0/1	Unknown	-	n
9	Agmatine_1	0.75	0.08	0.006	2/3	Fair	4	y
10	Allantoin_1	1	0.07	0.008	1/1	Unknown	3	y
11	alpha_Ketoglutaric_acid_1	1	0.18	0.013	1/2	Poor	-	n
12	Adenosine_1	0.75	0.03	0.009	5/6	Poor	-	n
13	L_Arginine_1	1	0.03	0.002	1/5	Good	4	n
14	L_Asparagine_1	1	0.05	0.007	3/3	Fair	4	n
15	Benzyl_alcohol_1	0.75	0.22	0.005	2/3	Poor	-	n
16	Cadaverine_1	0.67	0.13	0.003	0/2	Fair	-	n
17	Choline_1	1	0.02	0.006	3/3	Good	4	n
18	Cytidine_1	0.88	0.1	0.012	3/7	Poor	-	n
19	alpha,epsilon_Diaminopimelic_acid_1	0.67	0.2	0.009	0/2	Poor	-	n
20	Ethanolamine_1	1	0.01	0.003	1/2	Good	4	y
21	Fumaric_acid_1	1	0.04	0.001	1/1	Poor	3	y
22	D_Fructose_6_phosphate_1	0.6	0.03	0.017	2/3	Unknown	-	n
23	D_Glucosaminic_acid_1	0.67	0.17	0.012	0/4	Poor	-	n
24	D_Glucuronate_1	0.6	0.2	0.014	1/3	Poor	-	n
25	D_Glucuronate_2	0.6	0.15	0.007	0/3	Poor	-	n
26	L_Glutamine_1	1	0.12	0.002	1/3	Good	4	y
27	L_Glutathione_reduced_1	0.67	0.16	0.01	0/4	Poor	-	n
28	D_Glucose_6_phosphate_1	0.67	0.1	0.003	1/4	Fair	4	y
29	D_Glucose_6_phosphate_2	0.71	0.1	0.01	1/5	Fair	4	y
30	Glycerol_1	1	0.05	0.005	1/3	Fair	4	y
31	Glycine_1	1	0.03	0.004	1/1	Unknown	3	y
32	4_Guanidinobutyric_acid_1	0.67	0.26	0.006	2/2	Poor	-	n
33	N_Acetyl_D_glucosamine_1	1	0.11	0.008	2/7	Poor	3	n
34	N_Acetyl_D_glucosamine_2	0.75	0.08	0.006	2/6	Poor	3	n
35	D_Glucose_1	0.71	0.08	0.008	1/5	Poor	3	y
36	D_Glucose_2	1	0.13	0.008	0/7	Poor	3	y
37	L_Glutamic_acid_1	1	0.05	0.004	2/3	Good	4	y
38	DL_alpha_Glycerol_phosphate_1	0.75	0.2	0.01	0/3	Poor	-	n
39	L_Homocitrulline_1	0.6	0.17	0.021	1/3	Poor	-	n
40	Homoarginine_1	1	0.09	0.008	2/5	Fair	-	n
41	L_Isoleucine_1	1	0.02	0.005	5/6	Good	4	y
42	Lactic_acid_1	1	0.02	0.003	2/2	Good	4	y
43	Leucine_1	1	0.12	0.007	4/5	Good	4	y
44	Lysine_1	1	0.07	0.003	1/5	Good	4	y
45	Malic_acid_1	1	0.14	0.001	3/3	Fair	4	y
46	Methanol_1	1	0.06	0.002	1/1	Poor	3	y
47	5_Methyluridine_1	0.63	0.1	0.013	0/5	Poor	-	n
48	Alanine_1	1	0.02	0.002	2/2	Good	4	y
49	L_Methionine_1	0.75	0.08	0.005	2/3	Poor	3	y
50	L_Ornithine_1	1	0.13	0.01	2/4	Poor	4	y
51	6_Phosphogluconic_acid_1	0.6	0.19	0.025	2/3	Poor	-	n
52	L_Phenylalanine_1	1	0.03	0.006	6/6	Good	4	y
53	Putrescine_1	1	0.05	0.002	1/2	Unknown	-	n
54	Phenethylamine_1	0.6	0.17	0.006	2/3	Poor	-	n
55	L_Proline_1	1	0.03	0.003	6/6	Good	4	y
56	L_Serine_1	1	0.03	0.009	2/2	Good	4	y
57	D_Sorbitol_1	0.63	0.15	0.01	0/5	Poor	-	n
58	L_Tyrosine_1	1	0.16	0.012	4/5	Fair	4	y
59	L_Tartaric_acid_1	1	0.08	0.026	0/1	Unknown	-	n
60	L_Tryptophan_1	0.75	0.06	0.009	6/6	Poor	3	y
61	L_Threonine_1	1	0.05	0.006	3/3	Good	4	y
62	D_Trehalose_1	1	0.08	0.011	3/7	Poor	3	y
63	UDP_1	0.71	0.16	0.018	1/5	Poor	-	n
64	Uridine_1	1	0.05	0.007	3/8	Fair	4	y
65	UTP_1	0.71	0.14	0.014	0/5	Unknown	-	n
66	Uracil_1	1	0.11	0.003	2/2	Good	4	y
67	UDP_GlcNAc_1	1	0.06	0.008	3/16	Fair	4	y
68	UDP_glucuronate_1	0.85	0.13	0.011	0/11	Poor	-	n
69	L_Valine_1	1	0.03	0.001	4/4	Good	4	y
70	Xylitol_1	0.75	0.12	0.015	1/3	Poor	-	n
71	Maltose_1	0.64	0.15	0.009	0/9	Poor	-	n
72	Maltose_2	0.71	0.18	0.007	0/10	Poor	-	n
73	D_Ribose_2	0.83	0.04	0.016	4/5	Fair	4	y
74	Guanosine_1	1	0.13	0.003	0/5	Poor	3	y
75	Glycerophosphocholine_1	1	0.15	0.004	4/8	Poor	3	y
76	Allocystathionine_1	0.6	0.24	0.012	2/3	Poor	3	n
77	Glycyl_L_Leucine_1	0.6	0.09	0.01	3/3	Poor	-	n
78	Propionylglycine_1	0.67	0.13	0.029	1/2	Poor	-	n
79	Dimethylmalonic_acid_1	1	0.1	0.001	0/1	Unknown	-	n
80	Erythrose_1	0.6	0.13	0.01	1/3	Poor	-	n
81	Gulonic_acid_1	0.6	0.18	0.02	1/3	Poor	-	n
82	Dimethyl_sulfone_1	1	0.23	0.006	0/1	Unknown	3	y
83	L_Iditol_1	0.75	0.14	0.006	1/3	Poor	-	n
84	UDP_galactose_1	0.62	0.08	0.007	1/8	Poor	-	n
85	gamma_Glutamylcysteine_1	0.6	0.15	0.011	1/3	Poor	-	n
86	Saccharopine_1	0.88	0.09	0.008	4/7	Fair	4	n
87	UDP_glucose_1	0.93	0.16	0.007	1/13	Good	4	y
88	CDP_choline_1	0.73	0.18	0.005	2/8	Poor	-	n
89	1_Methylguanosine_1	0.75	0.17	0.016	2/6	Poor	-	n
90	Hydroxyphenyllactic_acid_1	0.6	0.13	0.01	1/3	Poor	-	n
91	D-Glucuronic_acid_1	0.6	0.16	0.008	0/3	Poor	-	n
92	Glycogen_1	0.71	0.2	0.007	0/20	Poor	-	n
93	Maltotetraose_1	0.75	0.17	0.01	0/18	Unknown	-	n
94	Maltotetraose_2	0.67	0.16	0.008	0/16	Unknown	-	n
*	citrate	-	-	-	-	-	2	y
*	glucose-1-phosphate	-	-	-	-	-	2	y
*	nicontinate (niacine)	-	-	-	-	-	2	y
*	NAD+	-	-	-	-	-	2	y

a	Matched compound index provided by COLMARm[1]
b	Compound name as provided by COLMARm. The format is specified as CompoundName_isomerNumber_spinSystemNumber.
c	Matching ratio is an output parameter of COLMARm defined as "the ratio of the matched peaks to the total number of peaks of the metabolite"
d	Average RMSD (root-mean-square deviation) in the 13C dimension between input and database peaks. A smaller magnitude RMSD indicates a better match.
e	Average RMSD (root-mean-square deviation) in the 1H dimension between input and database peaks. A smaller magnitude RMSD indicates a better match.
f	Uniqueness score is an output parameter of COLMARm indicating the uniqueness of the match in the COLMAR database using "the number of cross-peaks in the HSQC spectrum of the mixture that are uniquely assigned" to a metabolite
g	User-indicated score in COLMARm. For this study, "Unknown" indicates no confidence in an assignment, "Poor" indicates having only one peak matching (even for compounds with only one peak), "Fair" indicates a low observed/expected peak ratio, and "Good" indicates a credible annotation.
h	Confidence score as described in Walejko et al.[2]: (1) putatively characterized compound classes or annotated compounds, (2) matched to literature and/or 1D reference data such as HMDB[3] and BMRB[4] (3) matched to HSQC, (4) matched to HSQC and validated by HSQC–TOCSY (COLMARm), and (5) validated by spiking the authentic compound into sample.
i	"y" indicates that characteristic peaks were observed in the 1D spectra of extracts. Citrate, G1P, nicontinate, and NAD+ were observed only in 1D spectra.
*	not ID'd using COLMARm

Supplementary Table 1A. Annotations of 2D, 1D on Extract. All annotations from COLMARm.

ID[a]	Name[b]	Confidence Score[c]	Extract -> *in-vivo* mapping notes	Quantification Score[d]
48	Alanine_1	4	Good for quant.	3
35	D_Glucose_1	3	annot/quant.	3
36	D_Glucose_2	3	annot/quant.	3
28	D_Glucose_6_phospha	4	annot/quant.	3
29	D_Glucose_6_phospha	4	annot/quant.	3
62	D_Trehalose_1	3	OK for quant.	3
21	Fumaric_acid_1	3	Good for quant.	3
74	Guanosine_1	3	Good for quant.	3
49	L_Methionine_1	3	Good for quant.	3
52	L_Phenylalanine_1	4	Quant. possible. Use ~7.4ppm	3
58	L_Tyrosine_1	4	Good for quant. 6.9ppm	3
69	L_Valine_1	4	Good for quant.	3
87	UDP_glucose_1	4	Good for quant. upfield ~5.8ppm	3
66	Uracil_1	4	Good for quant.	3
64	Uridine_1	4	Good for quant.	3
*	citrate	2	Good for quant.	3
*	glucose-1-phosphate	2	Good for quant.	3
13	L_Arginine_1	4	Good for quant, multiplet ~1.7 ppm. Other multiplets overlapped with Lysine. ~3.24, badly overlapped with glucose.	3
*	Succinate	2	Good for quant.	3
17	Choline_1	4	Good for quant.	3
12	Adenosine_1	-	Good for quant. 8.3ppm	3
20	Ethanolamine_1	4	Good for quant., but small and noisy	2
37	L_Glutamic_acid_1	4	Overlapped with glutamine. Could quantify ~2.35ppm.	2
41	L_Isoleucine_1	4	Good for quant. Some overlap.	2
42	Lactic_acid_1	4	chemical shift changes allow discernment from Threonine	2
1	D_Mannitol_1	4	Overlapped with glutamate. Do not quantify, but qualitative OK	2
26	L_Glutamine_1	4	Overlapped with glutamate. Do not quantify, but qualitative OK	2
67	UDP_GlcNAc_1	4	Good for qualitative information about trend, but bad peak shape, cannot trace	2
73	D_Ribose_2	4	removed with water/overlapped. possible quant at 5.4ppm	1
50	L_Ornithine_1	4	Small peaks; difficult to trace	1
61	L_Threonine_1	4	Does not shift ppm, so possible to discern from lactate	1
45	Malic_acid_1	4	too low to trace	1
*	NAD+	2	not confident, but possible annotation	1
60	L_Tryptophan_1	3	Annotate only, overlapped with Uracil	1
43	Leucine_1	4	Overlapped. Do not quantify.	1
44	Lysine_1	4	All overlapped, esp. with Arginine	1
46	Methanol_1	3	cannot annotate	0
9	Agmatine_1	4	cannot annotate	0
10	Allantoin_1	3	cannot annotate	0
82	Dimethyl_sulfone_1	3	overlapping, cannot annotate	0
30	Glycerol_1	4	cannot annotate	0
75	Glycerophosphocholin	3	cannot annotate	0
31	Glycine_1	3	cannot annotate	0
55	L_Proline_1	4	cannot annotate	0
56	L_Serine_1	4	cannot annotate	0
*	nicontinate (niacine)	2	cannot annotate	0

a	ID index from initial matching (Supplementary Table 1a)
b	Compound name from initial matching (Supplementary Table 1a)
c	Confidence score for initial matching (Supplementary Table 1a)
d	Quantification Score for compounds in the real-time data: 0 (unannotated), 1 (annotated only), 2 (qualitatively assessed), or 3 (relatively quantifiable)
*	not ID'd using COLMARm[1]

Supplementary Table 1B. Mapping to *in vivo* data. Compounds were fit according to Judge et al. (2019) using COLMARm and annotations were manually assessed and assigned confidence scores. Peak annotations were mapped to 1D *in vivo* data by visual comparison.

Annotated in 1D *in-vivo* data	Quantified in *in-vivo* data
alanine	adenosine
glucose	alanine
glucose-6-phosphate	arginine
trehalose	choline
fumarate	citrate
guanosine	ethanol
methionine	formate
phenylalanine	fumarate
tyrosine	glucose
valine	glucose-1-phosphate
UDP-glucose	glutamate
uracil	guanosine
uridine	isoleucine
citrate	lactate
glucose-1-phosphate	phenylalanine
arginine	succinate
succinate	trehalose
choline	tyrosine
adenosine	unknown-179
ribose	uracil
ethanolamine	uridine
glutamic acid	valine
isoleucine	
mannitol	
glutamine	
ornithine	
threonine	
lactate	
malate	
UDP-GlcNAc	
serine	
tryptophan	
leucine	
lysine	

Supplementary Table 1C. Annotations for *in vivo* data. Manually curated annotations and quantifications for *in vivo* data.

References

1) Bingol, K., Li, D. W., Zhang, B. & Bruschweiler, R. Comprehensive Metabolite Identification Strategy Using Multiple Two-Dimensional NMR Spectra of a Complex Mixture Implemented in the COLMARm Web Server. Anal Chem 88, 12411-12418, doi:10.1021/acs.analchem.6b03724 (2016).

2) Walejko, J. M., Chelliah, A., Keller-Wood, M., Gregg, A. & Edison, A. S. Global Metabolomics of the Placenta Reveals Distinct Metabolic Profiles between Maternal and Fetal Placental Tissues Following Delivery in Non-Labored Women. Metabolites 8, 10 (2018).

3) Wishart, D. S. et al. HMDB: the human metabolome database. Nucleic Acids Res 35, D521-D526 (2007).

4) Ulrich, E. L. et al. BioMagResBank. Nucleic Acids Res 36, D402-D408, doi:10.1093/nar/gkm957 (2008).

Supplementary Table 1D. References.

Compound	Timepoint (one aerobic sample)						Peaks Used (ppm)	Notes
	1		89		157			
	Lower Bound	Upper Bound	Lower Bound	Upper Bound	Lower Bound	Upper Bound		
Citrate	5.5	6	5	5.5	5	5.5	2.8-2.5	5.6 does not make sense; ignoring
Glutamate	7.5	8	4.5	5	5	5	2.4-2.3	little movement >6
Succinate - d2O	5.6	7	--*	5.6	--	5.6	2.4-2.5	use d2O or surine?
Succinate - surine	5.5	6	4	4.5	4.5	5	2.4-2.5	use d2O or surine?
Fumarate	8	--	4.5	5	5	5.5	6.45-6.6	
Alanine	8	--	4	--	4	--	1.35-1.4	little movement 4-8ppm
*	--	not bounded						
**	nd	not detected						

Supplementary Table 2. Selected pH fits for organic acids in three timepoints representing the extremes of pH changes. pH Fits derived using AssureNMR (Bruker, Billerica, MA, USA) on spectra from timepoint 1, 89, and 157 generally agreed with interpolated pH derived from in-house citrate titration data.

EXAMPLE CIVM-NMR PROTOCOL

Example Protocol for CIVM-NMR using addition solutions

Running 6 mg WT in QA 0.3%.

Prepping Materials

Clean ~2'x4' area of bench, using EtOH. Set out a 1.5 mL tube rack, 3-4 layered Kimwipes ("Drying Pad"). Leave some other Kipwipes to put rotor components on.

Set out **P1000, P200, P20**, and **tips** for each. Best if not autoclaved.

Wash Rotor, plug, cap, plug removal screw, needle-nose forceps:
- lay out components on Kimwipe
- lay out a clean Kimwipe for drying
- bleach solution (optional) X 1, then H2O (tap) X 4
- EtOH 70% X 2
- ddH2O X 4
- dry with Kimwipe
- store in clean eppi tube

Apply new Rayon **filter tape** punch to hole in cap. Press down around edges to stick. Ensure it is centered. Two layers

Set out **Eppi Tubes** and rack:
Pre-weigh, Rinses 1-4, Weigh/Measure (rotor volume), Solid Rotor Contents, Liquid Rotor Contents
2 Collection tubes & High-Pure Spin filters for separation at endpoint:
-> solids (rinse with H2O 4x 200 µL) -> remove to eppi tube -> freeze
-> liquid (pipette to eppi tube and freeze)

Set out **15-mL tube** for Wash Solution.

Set out **~10 mL ddH20** (a clean beaker is fine).

Tube for post_org liquid

Solutions:

Make **10X Vogels Media** (minimal; no citrate)

Still using 2018 stocks (contains ethanol). Not even on the second bottle yet.

Make **Wash Solution** (4.5 mL)

In a 15 mL Falcon Tube:

4050 µL ddH2O
450 µL 10X Vogels Media

Vortex to mix. Make 4 x 1 mL aliquots (R1-4). Use within a few hours.
Rinse media visibly contaminated after a few days in warm room, along with 10X. Will filter-Sterilize the 10x. using frozen aliquots of 10X today.

Make **Addition Solution**(s)

VMM NMR Media for 23NOV2021:
In a 1.5 mL eppi tube:

ddH2O	888 µL
NaOH (11.9 M in H2O)	12 µL
QA Stock (60% in ddH2O)	375 µL => 15 % or
DSS (20 mM in D_2O)	75 µL
10X Vogels Media	150 µL
	1500 µL

pH 4.34 using NaOH

Vortex and spin down.
Filter-sterilize with 0.20 µm syringe/spin filter, if desired.
Store @ -20C to prevent contaminant growth and evaporation (usually handled in open air)
Vortex and spin down before opening after thawing.

Also made a 1:5 dilution of this in NMR Media (gives 3%, for a 5/50 µL spike-in, -> 0.06% final [QA]). Made a **1:5 dilution** again **13JUN2021 <- Using this**

Make **NMR Media** (minimal) – Remade 9 mL 29/31MAY2021 in 6 x 1.5 mL aliquots. **– Using this**

In a 1.5 mL eppi tube:

1275 µL	ddH2O	->	1.5 mL is plenty
150 µL	10X Vogels Media	->	1X
75 µL	DSS (20 µM in D_2O)	->	5 % D_2O, 1 mM DSS
1.5 mL			

Vortex and spin down.
Filter-sterilize with 0.20 µm syringe/spin filter, if desired.
Store @ -20C to prevent contaminant growth and evaporation.
Vortex and spin down before opening after thawing.
pH: 4.48

Prep media sample:

Tare the rotor assembly in an eppi tube.
Add 50 µL NMR media to rotor from bottom. No bubbles.
Add spacer, anaerobic cap with o-ring. Be sure to twist it on. Mark tube corner with sharpie.

Running NMR

Running from a previous CIVM-NMR experiment:

Copy old experiment(s) to new name with the extension "Org":

(ex. expName = HRMAS_ncrassa_glucose_Org)

edc

Expt # 1

current parameters (can use getprosol if haven't done a run in a while)

my nomenclature:

qax_40_media_opt

qax_40_ media

qax_40_ media_gluc_opt

qax_40_ media_gluc

qax_40_media_qa_opt

qax_40_media_qa

qax_40_media_qa_gluc_opt

qax_40_media_qa_gluc

qax_40_ media_org_opt

qax_40_media_org

qax_40_media_org_qa_gluc

edasp

default

save and close

this checks the routing and fixes it if someone messed with it

check bf1 = spectrometer frequency (sometimes this gets reset)
also check in procpars that SF = spectrometer frequency. If not, ppm axis will be wrong.

Drop rotor cap side up into magnet bore. It will fall, this is normal.
open MAS display (double click the 0 Hz at bottom of topspin window)
set spin speed: 3500 Hz
set temp (corr) to 298 K (25 C)
insert
go
let settle to +/- 10 Hz (best if stable on set speed, green)

wobb

1H (no ^{13}C in there)

adjust match, tune so that V is bottom and center

stop

lock H2O_D2O+salt

this may take a while, as locking to 5% D_2O is not always easy/straightforward, especially when the spect frequency drifts a lot. Can use a D_2O sample to lock on first to help it.

If lock is insufficient, too noisy continue. If not, try:

double click the lock graphic for better view

bsmsdisp

turn lock off to check phase:

red and green somewhat symmetrical?

adjust phase if not (- makes red smaller)

turn lock back on

if low lock, lower gain. Increase power until overshooting. Then, bump down till looks like no more over/undershooting (characteristic of saturation). Then lower 2-3 more clicks, and use gain to bring intensity back up to ~60-70%.

If lock is not found, maybe use D_2O sample to help the spec find it. Or change field. Sometimes deuterium tuning + matching is off, so check that.

pulsecal (on noesypr1d)

4.4 dB µs

-7.63 dB µs

If ^{13}C or Jres is part of the run, load the expt, etc. and execute:

getprosol 1H -7.63 11.95

rga

* also do this for each expt. type

ds 0

ns 8

zg

check water suppression, shims.

for shims:

try ‘topshim hrmas’ as a starting place. zg to check.

try loading other shims using ‘rsh’

write shims with ‘wsh’

if shims are still bad, you can try JG’s suggestions:

check sample has no bubbles, etc.

gs

…

bsmsdisp

Shims

use Y shims, most sensitive

small steps, let it scan a few times with each adjustment. Has to “settle”

X, XZ if necessary, but needs large amounts
if hsqc, check lock balance if weird phasing-like distortion issues at base of peaks
tweak upper order shims, topshim hrmas to redo lower ones.

to optimize water suppression:

collect quick zg (ds 0, ns 4). Ns can be 1 if in a hurry, but noisier.
zoom into region +/- 0.5 ppm of the water peak around 4.7 ppm
right click -> Save Display Region To -> Parameters F1/2 … [dpl]

popt

check the following:

- Perform automatic baseline correction (ABSF)
- Calculate optimum after POPT has finished, but do not store in dataset
  This last one is in case you don't like the opt that the program finds.

Parameter: o1
Optimum: magmin
Startval: 2816
Endval: 2824
Inc: 1
Once done, open 999 under the current exp (noesypr1d).
optimal o1 result (we want smallest water signal): 2821 Hz

Go back to '1'

o1 2821

Can also try: gs to adjust PLDB9 slightly to get better baseline/shims by better water suppression. Lower numbers = higher power. Do not go lower than 42. Higher power is not always better, especially when lineshapes (shims) aren't great. **DO NOT DO THIS FOR CRYOPROBE (800MHz). Check with facilities manager before attempting to mess with power levels.**

Finally, be aware that a filter is often applied in processing (TopSpin or NMRpipe) that will do a pretty good job squashing the remaining water peak, so it doesn't need to be perfect. We also cut it out. Most important is that baseline around it isn't too distorted. To see what the filter looks like in TopSpin:
Processing -> BCMOD qfil BCFW = ~0.1-0.5 (based on whatever looks good), or
bcfw 0.1 (from command line)

* Reducing lock gain can help with ADC Overflow error?

zg again to make sure it looks good.

Make a copy of the experiment (edc -> '2' is fine). Keep this in '_opt'

Set

ns 8 (minimum # for noesypr1d)
ds 0 (no need for these)

check Acquisition Params tab

Automation AUNM (this should be au_zgonly) so the program only does the minimum for collection, not a bunch of other stuff like rga, shim, etc. That would just waste our time because we aren't changing the sample, and would also disrupt continuity unpredictably across timepoints).

iconnmr

log in

check configurations […] Load mtj config file.

automation

(assuming the experiment you want to run is already up in TopSpin)

select first row in Icon (sample 1)

Tools -> Import

Sample # = 1

Change experiment name to "…qax_40_media"

Experiment # = 1 (unless continuing from other run)

Import, close import window

Right click experiment you just imported -> Iterate

keep right clicking and iterating first row till you have enough experiments

for ns = 8, ds = 0, each expt is 30 s + 5 s overhead (= 103 expts/h)

Expts: 10

Select sample 1 row

Right click -> Submit (this queues the experiments, and takes several minutes for #'s > 1000.

Once queued, click Start

Check first sample in magnet, etc.

No processing

If prompted about temperature handling, say no. It will waste minutes of time and is unnecessary.

Alternatively, if # expts < 500, you can edc to "…qax_40_media", then type multizg # to queue and run an iteration of the current expt. Interleaved experiments won't work with this approach, however.

Once the above expt is finished:

Icon

Stop. yes, really stop the run.

Delete the sample 1 in icon automation window.

TopSpin

MAS Display

Stop

Eject

Media + Addition Solution (spike into media)

Open up the rotor. Remove 5 µL of liquid to waste. 5 µL **Addition solution ->** rotor.

Drop sample into bore.

TopSpin
MAS display
Insert
edc to "…qax_40_media_gluc_opt"
wobb – will likely need adjustment
lock (as above)
pulsecal (on noesypr1d) 90 degree pulse (this should do getprosol as well)
4.4 dB µs
-7.6 dB µs

getprosol 1H -7.63
rga
zg

Shims, water suppression should be fine.
Load up icon automation as above, 10 experiments to "…qax_40_media_gluc"
Stop icon run as above.
Eject rotor
Rinse rotor assembly well with EtOH, H2O, ddH2O. Dry all components, keep on kimwipe.

Prepping Mycelia

Grow ***N. crassa*** **in liquid culture** (Vogels Media 1.5-3% Glucose, w/v) for 24-52h, shaking under constant light @ ~230 rpm. I find that earlier-stage cultures are easier to spin, but this varies with [glucose].

Genotype: WT

Media: Arom Vogels Sucrose 1.5% (18JUN2021, filter-sterilized, full recipe)

Start Time & Date:

End Time & Date:

Mark start and end time (I write these on the tube as well), then pour into **50-mL Falcon Tube**. It is helpful to use the ones that stand up on their own. No need to be aseptic.

Transport to the NMR Facility.

If aerobic run, use cap with o-ring and drilled hole. Use a scored and sharpened Pasteur pipette to punch out two layers of filter from rayon breathable sticky membrane tape, sticky side on finger and coming from the other side. Use wire down center to push onto inside of rotor cap, one layer at a time.

Tare scale with **Weigh/Measure (M/W) Tube**.

Using forceps, tear off a piece of mycelium, or collect loose bits in earlier cultures. Some liquid will come along. The volume in an eppi tube should be ~**100**-150 µL. This typically yields ~20 mg of mycelia once pat-dried. I've been using less, though, around 50 µL -> 1-2 mg

* use the forceps for all subsequent mycelia handling steps. Clean with EtOH and dH2O before sensitive steps.

Mass of mycelium in tube (with liquid): mg
(to gauge mycelium density in culture)

Dab the mycelium onto Drying Pad to remove most liquid. Doesn't need to be perfect. Add to **Rinse Tube 1** (**R1**). Vortex briefly (~5-10 s) to resuspend/wash.
* The mycelia will be starved from this point onward. Sometimes this is desired.
Note the time:
Repeat on a fresh spot on Drying Pad, add mycelia to **R2**.
Repeat, add to **R3**.
Repeat, add to **R4**.

Dab mycelia on a clean area of the Drying Pad, then fold over another clean part of the Drying Pad to lightly pat-dry the mycelia. Repeat ~4-5 times as needed until no wet spots appear on the Drying Pad.

Working quickly to minimize time spent dry:
Add pat-dried mycelia to pre-tared **Weigh/Measure (M/W) Tube**. Weigh them:
Initial Mass: mg
Using forceps, tear off enough of the mycelia to get ~1-6 mg of mycelia.
Mass: mg
Mass: mg
Final Mass: mg

Add 50 µL **NMR Media**.

Tare rotor (rotor only, no spacer/cap)

Add all contents of **Measure Tube** to the clean, dry rotor. Be careful not to introduce bubbles. I use one prong of the forceps to move the mycelia to the bottom of the tube, then pipette the liquid in (from the bottom). Centrifuge briefly within an eppi tube to pop bubbles. Not too much, or the rotor might deform the tube/fail catastrophically. 4-5k rpm is okay.

Mass of rotor contents: mg

50 mg – result = mg = same number in µL
Add this number of µL to the rotor to make 50 µL = 50 mg.
Spin down again.
Reweigh rotor with contents : mg

Insert the plug slowly to rotor-level, then push ~1 mm lower.

If a drop of liquid appears in the plug, **re-add it to the rotor** or dab with kimwipe. Insert the cap (usually aerobic, with hole and o-ring) completely by twisting (this helps with the O-ring and smooth insertion), then remove it. **For 50 µL volume, shouldn't be an issue.**

Repeat the liquid check and remove by dabbing, if necessary. This shouldn't be an issue @ 50 µL, and I don't do it routinely.

Carefully re-cap the rotor by twisting the cap on.

Running NMR on Organism

Record total mass of rotor ready to run: mg

Drop sample into bore.

TopSpin
- MAS display
  - Insert
- edc to "…qax_40_media_org_opt"
- wobb – will likely need adjustment
- lock (as above) – this will get noisier because the organism takes up volume.
- pulsecal (on noesypr1d) 90 degree pulse (this should do getprosol as well)
  - 4.4 dB µs
  - -7.6 dB µs

- getprosol 1H -7.63
- rga
- zg

Shims, water suppression should be fine.
Once satisfied with the spectra, collect a baseline spectrum for the organism in its media. It may be a good idea to go ahead and collect an hour or so of spectra as a baseline (e.g. in (-) carbon source conditions).
Load up icon automation as above, 10 experiments to "…qax_40_media_org"
Start the run.

Set out in the facility:
Addition Solution
Kimwipe(s)
P10 and tips
Spacer screw
Post – org tube (if collecting)

Stop icon run as above.
Eject rotor

Remove the rotor from the magnet.
Weigh the rotor (everything included): mg

Spiking

*** NOTE: if the full rotor mass has not been measured, do so now.
mg

Load a spectrum one from the _org run above (or edc to "…media_org_gluc_qa_opt". The proper way to do this would be to do a mock-up for this medium/organism ahead of time to test what the correct PW, etc. would be. That's a lot of time, it's not totally accurate (unless you get two identical mycelia), and the following usually works fine for me:

Modify Pulse width
Two factors are changed from plain media to the spiking procedure:
1) Addition of organism
2) Addition of addition solution
Which of these had a greater effect from the plain media?
If $PW_{media} < PW_{media+addition\ solution} < PW_{media+org}$

no change necessary if going off of "…media_org" spectrum; PW already set

If $PW_{media} < PW_{media+org} < PW_{media+addition\ solution}$

getprosol 1H $PW_{media+addition\ solution}$ -7.63

Then go to icon, import this experiment to "…media_org_qa", and queue up ~12 h of experiements (~1300). I usually queue more just in case I can't get back in time (we're paying for the time, so might as well collect data!). Make sure these are queued (i.e. submitted), not started. You can iterate more and queue them after the run starts, but it may pause the run briefly.

If using multizg (good for single pulse sequence, < 500 spectra), get it ready to submit.

Remove the cap + spacer. No liquid? If liquid, you can add it back to the rotor or discard it.
If discarding, note the volume: µL

Remove 5 µL of media from the rotor and discard or save for analysis -> "qax_40 Post Starve"
Bring up the MAS Display to have insert + go ready ASAP.
Double-check the mark on the rotor.
Get 5 µL mixed Addition Solution ready in pipette tip.

When ready, start a stopwatch.
Working quickly, add in the 5 µL of Addition Solution, taking care to not introduce bubbles.

Quickly, carefully cap and return to magnet. Import and Go immediately.

As soon as spin speed is rising:
wobb, make adjustments as necessary
within ~30Hz:
re-lock, or adjust, if necessary
Start, sample in magnet, no processing, no to temperature handling.
Once first scan starts, record stopwatch time (should be 2.5-5 min):

Record Start time and date:

Once it's done, stop the icon run, delete the sample in automation window. Close iconnmr to reset counter (max's out at ~4K experiments, even after deleted)
Navigate to the data: root/opt/nmrdata/judgemt
Find the dirs for this expt. Right click -> compress to -> Name by expt. (e.g. civm_qax_40
Upload to appropriate location on Dropbox or access via Synology.

Record done time and date:

(1) Weight rotor (directly from run): mg

(2) Mass of rotor ready to run (pg. 10, pre-org run) = mg

Mass lost = (1) – (2) = mg

Rotor contents collection, processing, and storage:

Set out ice.
Keep all tubes and reagents (H2O) on ice. H2O can be stored in the 4C fridge until use.
Set out LN2 in vessel or dry ice/EtOH bath in vessel.

Solids:

Weigh Solids (rotor contents) tube: mg (1)
Transfer rotor contents to tube. **Weigh**: mg (2)
contents recovered = (2) – (1) = mg (3)

amount lost during run = total rotor mass (start – end) = mg (4)
net contents = starting content mass - amount lost during run
(mg) - (3) = mg (5)
(5) - (3) = recovery loss
(mg) - (mg) = mg

Pipette off as much liquid as possible without disturbing mycelia. Some loose mycelia will get sucked up; that's fine. Add this media to a HPF filter bed in a collection tube and spin down.

Repeat 4x:
Add 500 uL ddH2O, mix with pipette tip/vortex
Pipette off 450 µL , discard

Flash-freeze and put in -80C
later: -> lyophilize 24h or till dry -> weigh: mg (6)
solids recovered = (6) – (1) = mg (7)

Liquids:

Tare "qax_40 Post Run Liquid" tube
Transfer liquids by pipetting to "qax_40 Post Run Liquid"
Weigh: mg (8)
Freeze @-80 next to solids.

Contents retained during separation = (8) + (6) / (3)
= = %
Contents retained from experiment start = (8) + (6) / (initial contents)
= = %
* conversion factor (damp -> dry) =
% Growth change in organism mass =
= (7) / initial mycelia mass (damp) * conversion factor
= = %